

Light as a Universal Tool:
Microcapsule Sizing by Elastic
Light Scattering
and
Mineral Investigation by *in situ*
Raman Spectroscopy

Dissertation
zur Erlangung des
naturwissenschaftlichen Doktorgrades
der Bayerischen Julius-Maximilians-Universität Würzburg



vorgelegt von

Nicolae Tarcea

aus Orlat, Rumänien

Würzburg 2004

Eingereicht am:

bei der Fakultät für Chemie und Pharmazie

1. Gutachter:

2. Gutachter:

der Dissertation

1. Prüfer:

2. Prüfer:

3. Prüfer:

des Öffentlichen Promotionskolloquiums

Tag der mündlichen Prüfung:

Doktorurkunde ausgehändigt am:

to Beatrice

Table of Contents

General Introduction	1
I Microcapsule Sizing by Elastic Light Scattering	5
1 Introduction	7
2 Particle Sizing Methods	9
2.1 Ensemble Methods	10
2.2 Counting Methods	12
2.3 Fractionation Methods	14
3 Elastic Light Scattering: Theoretical Considerations	19
3.1 Numeric Methods	20
3.2 Mie Theory	22
3.2.1 General Formalism	22
3.2.2 Mie Expansion Coefficients for a Homogeneous Sphere . .	23
3.3 Extensions of Mie Theory to Coated Spheres	25

3.3.1	Mie Expansion Coefficients for a Monolayered Sphere . . .	26
3.4	Far Field Intensity: Phase Function	28
4	Experimental Realization	33
4.1	Experimental Setup	34
4.1.1	Laser	34
4.1.2	Optical Setup and the Flow Cell	40
4.1.3	Detection System	45
4.2	Measurement Procedure	45
4.2.1	Data Acquisition	46
4.2.2	Database of Scattering Patterns	49
4.2.3	Data Evaluation	49
4.2.4	System Calibration	51
4.3	Measurements	52
4.3.1	Homogeneous Spheres	54
4.3.2	Microcapsules	55
II	MIRAS	
	Mineral Investigation by <i>in situ</i> Raman Spectroscopy	59
5	Introduction	61
6	Supporting Laboratory Experiments	65
6.1	Mineral Spectra Database	66
6.2	Measurements on Meteorite Samples	69
7	MIRAS - Instrument Design and Construction	79
7.1	Instrument Requirements	80
7.2	Proposed Designs	81
7.2.1	Hadamard Spectrometer Based Design	83
7.2.2	AOTF Based Design	84
7.3	Breadboard Setup	84
7.3.1	Laser	85
7.3.2	Filter Box	86
7.3.3	Raman Head: Optics	87

7.3.4	Acusto-Optical Tunable Filter	87
7.3.5	Detector	89
7.4	Conclusions	91
7.4.1	Extended MIRAS	93
8	MIRAS - Software Implementation	95
8.1	Measuring Procedure	95
8.2	Data Processing: Corrections	96
8.3	Supportive Database: Implementation	99
9	MIRAS - Bread Board Measurements	103
10	Remote Raman Spectroscopy for Planetary Prospecting	109
10.1	Micro Raman and Raman LIDAR	110
10.2	RRS Instrument Simulator	112
10.3	Input Parameters and Numerical Simulations	113
10.4	Discussion of Simulator Output	118
10.5	From Laboratory Raman to RRS	120
	Summary	127
	Zusammenfassung	131
A	Equation Repository	135
B	Microparticle Analyzer Device - Setup Images	139
C	MIRAS - Breadboard Images	141
	Bibliography	147
	List of Figures	159
	List of Symbols and Abbreviations	161
	Danksagung	163
	Lebenslauf	165

General Introduction

Electromagnetic radiation is one of the most important tools for probing the structure and dynamics of matter. The simplest way of bringing the matter and light into interaction is the simple act of 'shining' light onto matter. In light-scattering experiments, the incident light field is considered to be weak enough so that the investigated system can be assumed to respond linearly to it. The general approach is to describe the response of the system to this weak incident field, namely to characterize the changes of the light field due to its interaction with the system.

In general, when radiation of angular frequency ω_0 is incident on a material system, scattering of the radiation occurs. Considering only the scattering phenomena, if the spectral content of the scattered radiation is analyzed, not only the angular frequency ω_0 associated with the incident radiation but also, in general, pairs of new frequencies of the type $\omega_0 \pm \omega_M$, $2\omega_0 \pm \omega_M$ or $3\omega_0 \pm \omega_M$ will be observed. The processes that take place are known as Rayleigh scattering, Raman scattering, hyper-Rayleigh scattering, hyper-Raman scattering, coherent anti-Stokes Raman scattering, coherent Stokes Raman scattering, stimulated Raman, second hyper-Rayleigh scattering, second hyper-Raman scattering, coherent

anti-Stokes hyper-Raman scattering, coherent Stokes hyper-Raman scattering, stimulated hyper-Raman spectroscopy... and many others (e.g. scattering on the acoustic waves - known as Brillouin scattering).

The elastic scattering (i.e without change of frequency) is generally referred to as Rayleigh scattering, and inelastic scattering (i.e. with change of frequency) is called Raman scattering.

The inelastic scattering of photons, referred to as Raman scattering was first observed in 1928 and named after its experimental discoverer. Raman and Krishnan discovered the effect while studying the scattering of light by liquids and named the observed scattered light "a new type of secondary radiation" [66]. Later in the same year, the observation of a "negative absorption of radiation" at frequencies higher than the excitation wavelength completed the overall picture. Smekal theoretically predicted the phenomenon [84]. Landsberg and Mandelstam [44] observed the effect by scattering light on crystals at the same time as Raman and Krishnan's experiments on liquids and published their results shortly after. In the 1960's, Raman spectroscopy became widely applied largely due to the development of the laser. The use of lasers made the investigation of other types of interactions involving more than one incident photon (hyper-Rayleigh , hyper-Raman and second hyper-effects) possible. Performant spectrometers, and sensitive detectors became available together with elaborate sample techniques[40], making Raman spectroscopy a standard investigation tool.

The classical theory of elastic light scattering was formulated by Lord Rayleigh at the end of the XIX century [67]. The main problem which the elastic scattering addresses is the relation between the properties of the scatterer (size, shape, optical properties) to the light scattering pattern. For simple geometries of the scatterer, the scattering patterns were obtained starting with the solution for the scattering of an infinite plane wave on a spherical homogeneous scatterer published by Mie in 1908 [52]. Solutions for more complicated systems followed. Solutions for magnetic spheres [39], layered spheres [3, 35, 36, 37, 54, 94], inhomogeneous spheres [102, 104, 105] as well as for infinite cylinders [68, 93, 2, 9, 47, 78], layered cylinders [4, 22, 35, 38] and also spheroids [5, 46, 78] were obtained. Exact solutions and approximations for calculating the scattering patterns were developed. A review of elastic light scattering theories is made by Wriedt [103]. Solving the problem of calculating scattering patterns for different scatterers the inverse

problem arises: how can the scatterer properties be inferred knowing the scattering pattern? Many methods have been developed addressing this problem, mainly in the field of particle sizing. Therefore for getting information on particle properties such as shape, size, refractive index or internal structure (layers, cavities) elastic light scattering is well established as a method of investigation.

In the present work, these two forms of light scattering are used for two different applications. One application addresses the elastic light scattering on microparticles, having the goal to design and construct of a device capable of determining the shell thickness and the core size for monolayer spherical particles in a flow.

The second application uses the inelastic light scattering for assessing the mineralogical composition of remote planets by *in situ* measurements. This second application consists of a small Raman spectrometer designed for robotic planetary missions.

The two different devices are described in the following chapters with the first part of the thesis discussing the microcapsule sizing by elastic light scattering and the second part analyzing the use of a Raman spectrometer as a tool for mineral investigations in space applications.

Part I

Microcapsule Sizing by Elastic
Light Scattering

*If you can kick it, it's hardware; if you
can only curse it, it's software.*

Anonymous

Chapter 1

Introduction

In recent years, an increasing number of microcapsule systems have been developed and have found applications in various fields of research and technology like food sciences, life science, pharmacy, cosmetics, cleaning, printing, to name just a few. The microcapsules are normally used for improving handling, stability and material performance, especially for controlled release of medicaments, flavors, fragrances, dyes, adhesives, fertilizers or hormones. Also, artificial microcapsules can serve as simple model for more complex systems like biological cells are. The industrial development of processes based on microcapsules depends on the possibility to provide clear and complete information about the properties of these microcapsules. However, the tools for an easy and efficient determination of the microcapsule properties are lacking, several methods being often required to describe adequately the microcapsule behavior. Methods for evaluating the individual size and size distribution of both the core and the shell are required together with methods for measuring the mechanical strength, stability in application media, permeability of the shell etc.

Elastic light scattering measurements provides a possibility for determining properties such as core size (a_C), shell size (a_S)(see Figure 1.1), refractive index

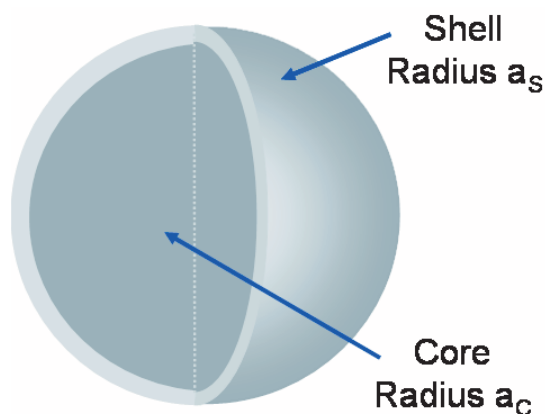


Figure 1.1: Core-shell microparticle

or eventually more complex internal structures (multilayers, cavities).

The design and construction of a device capable of measuring the above mentioned parameters for a core-shell particle is the subject of the first part of this thesis.

In chapter 2 a short overview on the methods used for sizing microparticles is given. Different sizing methods are compared, and the advantages and disadvantages for the general problem of sizing are shortly discussed.

Chapter 3 focusses on the theories used for calculating the theoretical scattering patterns with emphasize on the Mie theory generalized for layered particles.

The last chapter (4) of this first part describes the experimental approach for building an automatic microcapsule sizer. The approach started by O. Sbanski [76] with the development of a software packet for calculating and storing theoretical phase functions for core-shell particles was continued with the designing and construction of a measuring device. The hardware construction and the software with all implemented corrections imposed by the individual setup components are described in detail. Ways of improving the quality and the speed of the analyzing process are discussed. The final section presents measurements run on samples made of homogeneous spheres and also on samples containing industrial microcapsules.

Chapter 2

Particle Sizing Methods

Getting information on particles (particularly by sizing them) is of great importance in many industrial sectors. Knowledge about the size distribution is required everywhere from traditional ceramics manufacturing to semiconductor processing, biotechnology or pharmacology to name just a few. There is a great diversity of particle sizing methods, all of them having both advantages and disadvantages with regards to a specific application. There is no single best method: only the closest matching between the method and the application. In order to place our particle sizing approach in a larger context, a short overview of the most popular sizing methods is presented here. New techniques and new applications of the existing techniques are constantly being developed. This techniques can be classified in several ways (e.g. imaging vs. nonimaging, degree of separation, weighting method used, information content, size ranges etc.). We will start classifying these methods by observing that all methods are either based on single particle detection or on the assessment of the bulk particle content. Based on this observation, one can distinguish three basic classes: ensemble methods, counting methods, and separation methods. Each of these classes is covered in a separate

section below. Overviews on the particle sizing methods are given by Bailey [6] and by Provder and Dwight [64].

2.1 Ensemble Methods

The ensemble methods collect mixed data from all of the different size particles in a sample at the same time. To extract a distribution of particle sizes for the entire population, computational algorithms are employed. Common ensemble techniques are: Low Angle Laser Light Scattering(LALLS), Photon Correlation Spectroscopy (PCS), Back-scattering Spectroscopy (BSS). In general these methods are fast and easily automated but the size resolution is relatively poor.

Low Angle Laser Light Scattering (LALLS)

This method is based on reading light intensity data at different scattering angles (usually low angles) away from the axis of the laser beam which is passed through a sample of particles. Intensity data is collected at many different angles (up to 64 point detectors in most instruments). Mie theory light scattering calculations are applied to the intensity data in order to generate a distribution of particle sizes that is consistent with the observed light intensities. LALLS is applied to relatively low concentration samples, so that the effects of multiple scattering¹ are reduced. Normally multiple scattering makes it difficult to generate an accurate size distribution based on scattering angles. It is a very fast method and it also has the advantage of a very broad dynamic range (commonly from under 0.1 μm up to millimeters). One can measure both powders and fluid suspensions and the measurement is non-destructive. One disadvantage is the relatively low resolving power. E.g. narrow size distributions must be at least 15% - 20% different in size to be resolved. The entire distribution is represented by a set of 128 to 256 data points over the entire size range, so real high resolution measurement is not possible. Also the accuracy depends on the precision of the predefined optical parameters (refractive index, light absorption in the sample) available for the particles, as well as the accuracy of information about particle shape. All this parameters are used to calculate the scattering properties of the particles.

¹light scattered from one particle is in turn scattered by a second particle before reaching the detectors

Mixtures of particles with different optical properties, unusual shaped particles, particles with fine internal structure, porosity, or long thin fibers yield results that are far from being correct and can not normally be measured. Strongly absorbing particles may not produce a usable scattering signal [106].

Photon Correlation Spectroscopy (PCS)

Due to Brownian motion, light scattered from small particles (under $4 \mu m$) varies rapidly in intensity. The variation in intensity over very short times can be "auto correlated" to extract information about the velocity distribution of the particles that scattered the light. The average size of the particles and information about the size distribution is calculated. Since the method is not based on the intrinsic optical properties of the sample a minimum amount of information about the sample is needed to run an analysis. Even mixtures of different materials can be accurately measured. The fluid properties in which the sample is suspended has to be known (e.g the viscosity). Among the advantages that this method presents, the minimum measurable particle size (hundreds of nm), the simplicity and speed in measurement and the non-destructive character of the approach. A major disadvantage is the extremely low resolution. Usually particles must differ in size by 50% or more for PCS to reliably detect two separate peaks. Therefore, the method does not actually provide size distribution data, but rather the mean size and an estimate of standard deviation. Only small particles with significant Brownian motion can be measured. Larger particles ($>4 \mu m$) are beyond the instrument's range [57].

Back-Scattering Spectroscopy (BSS)

This method resembles the LALLS technique (*see* section 2.1). In contrast to LALLS, where the scattered light is recorded at low angles (close to the forward direction), for BSS the scattered light is measured at high angles (close to the backward direction). Light scattering calculations are applied to the measured intensity data to generate a particle size distribution. Back scattering is often applied to high concentration samples (e.g. industrial flux or samples that can not be diluted without changing the size distribution). Advantages of this method are the possibility of measuring samples that are too concentrated for most other sizing methods, a relatively simple operation and no sample preparation. One

disadvantage is the low resolution, even in comparison to LALLS. Multiple scattering from high concentration samples further reduces the resolution. The optical properties (refractive index, absorption characteristics) and shape of the particles must be known to generate accurate results. Strongly absorbing materials are hard to measure due to the weak back scattering signal.

2.2 Counting Methods

The counting methods characterize the sample by measuring one particle at a time by accumulating counts of particles with similar sizes. Some common counting methods are: the electrozone counter, the light counter, the time of flight counter, and the microscope (optical or electron). In each of these methods, particles are classified and placed in "size bins", one particle at a time. The counting of clusters of particles as a single larger particle causes the most errors in the reported size distribution for these type of methods. The accuracy and resolution of these methods depend on how accurately the size of each particle can be characterized during the (usually) very brief time that is counted.

Electrozone Counter

Before measurement, the particles are suspended in an electrically conductive fluid (usually saline water with emulsifier). The measurement consists in a forced flow through a small orifice where conductors are placed in the fluid on either side of the orifice and the electrical resistivity of the orifice is monitored as particles pass. Each particle produces a change in electrical resistivity as it passes the orifice. The intensity of the generated signal is proportional to the particle's volume. Each signal generated in this way is recorded and after a statistically sufficient number of passing events a size distribution is generated (one has to account for the statistically finite probability of co-incident counts²). This method is suitable for a relatively broad range of sizes (from 0.5 μm to more than 300 μm), is simple to implement and easy to calibrate with known size standards. The analysis is relatively quick and non-spherical particles can also be measured. Adjacent narrow peaks that differ by about 15%-20% can be resolved (comparable

²when more than one particle pass at the same time through the orifice generating a single count

to LALLS). Due to the possibility of blocking the measuring orifice with large particles the upper particle size limit is roughly 60% of the orifice size. The lower limit is approx. 2% of the orifice size and this limitation is imposed by the sensitivity with which the resistivity measurements are performed (particles smaller than $0.5 \mu m$ can no longer be detected). Therefore, for one measurement (using one counting gate) the dynamical range is relatively low. Analysis of broader distributions requires pre-separation of samples according to size. This makes analysis of broad distributions more difficult. Samples must be suspended in a conductive fluid which may not be convenient for many kinds of samples. Usually, the particles must be electrical insulators.

The Light Counter

The light counter is the optical equivalent of the electrozone counter (see Section 2.2). Particles are forced through a counting chamber, where a focused laser beam is partially blocked as the particle passes. The reduction in light intensity reaching a detector is related to the optical cross section of the particle, and this is converted to a size distribution. This method is suitable for a relatively broad range of sizes, from $0.5 \mu m$ to more than 2 mm (using different size sensors). It can be calibrated with known size standards. Resolution is comparable to LALLS and the size range is limited for a single run due to the size of the sensor. Non-spherical particles reduce resolution because the cross section of the particle is evaluated rather than its volume. The cross section for a given particle weight will depend on both particle shape and orientation as it passes through the detector. A second detector beam perpendicular to the first is sometimes used and allows a better measurement of volume. It is not possible to measure particles below $0.5 \mu m$, and measurements below 1 - 2 μm may be of lower accuracy.

The Time of Flight Counter

This technique is generally used for dry powders. An air stream containing particles is drawn through a fine nozzle into a partial vacuum. Particles accelerate in air according to size, with smaller particles accelerating more rapidly than larger particles. The particles then pass two focused laser beams. The first laser beam detects each particle and starts a time-of-flight clock, while their arrival at the second laser beam stops the clock. The time of flight is recorded, and the

individual times of flight are converted into a size distribution. This technique has the advantage that does work with dry powders and can easily be calibrated with known size standards. The total measurement range is from approx. 0.2 to 700 μm , where peaks that differ by 20% are resolved. Liquid suspensions of particles may be difficult or impossible to measure and non-spherical particles will be reported as smaller than correct.

Microscope Counting

With a microscope and an appropriate calibration scale, an operator can characterize a distribution of particles by visually classifying and manually accumulating counts of particles in different size ranges. Automated optical counting systems (with video camera and computer) have been implemented. Similar counting techniques can be applied to the images produced by electron microscopes. The method inspires great confidence in the results since it allows you to actually visualize the particles and evaluate their range of shapes and sizes. A quick look with a microscope often gives a great deal of information that other methods are unable to provide. On the other hand, it may be difficult to collect enough data to give a reliable result. The number of particles measured is usually small compared to other particle sizing methods, hence, representative sampling becomes critical.

2.3 Fractionation Methods

All separation methods apply an external separation force to the particles in a distribution to physically separate the particles according to size. The accuracy of these methods depends upon whether the particles react to the separation force as expected. The resolution of these methods depends on how completely the particles are separated according to size. Common separation techniques include sieves, gravitational sedimentation, the disc centrifuge, capillary hydrodynamic fractionation, sedimentation field flow fractionation, and others. In general this techniques are relatively slow compared to other sizing methods [83].

Sieves

Sieves are one of the oldest particle sizing methods, and are used in both the laboratory and in large production equipment to separate one size particle from another. The sizes of sieve openings have been standardized, so that there is reasonably good consistency between sieves from different manufacturers, at least in terms of their specifications. A series of sieves can be stacked on top of each other, with the coarsest sieve on top and the finest on the bottom, thus forming a sieve "column". A sample is introduced on top of the coarsest sieve, and progresses down through the column due to vibration, shaking, fluid flow, or some combination of these. Particles progress until they reach a sieve where the openings are too small for them to pass, whereupon they are retained. The weight of sample retained on each sieve produces a crude distribution of sizes. This is a simple and inexpensive method and it inspires great confidence in the results but is limited to relatively coarse particles. The reported distribution depends on the shape of the particles and the duration of the test, since the sieve will (in theory) pass any particle with the cross-section smaller than the nominal opening. Long thin particles will give very different results when compared to spherical particles of the same weight. The reported distribution possesses a low resolution (narrow peaks must be 35-40% different in size to be resolved). Very small particles ($<0.2 - 0.5 \mu\text{m}$) are not measurable.

The Disc Centrifuge (DC)

The disc centrifuge is a hollow, optically clear disc with a central opening on one side. The disc rotates at a known speed, from 600 RPM up to 24,000 RPM. The empty spinning disc chamber is partly filled with liquid that is held against the outside edge of the chamber by centrifugal force, forming a fluid ring inside the chamber. The liquid ring has a slight density gradient: the liquid at the outside edge of the ring has a slightly higher density than that near the inside edge. A small volume of a dilute suspension of particles is injected into the center of the spinning disc, and quickly reaches the liquid surface. Particles sediment from the surface toward the outside edge of the chamber at rates that depend on particle size, with the large particles moving much faster than the small ones. A detector beam (usually a light beam) passes through the liquid near the outside edge of the disc, and particles passing the beam reduce the intensity in proportion to their

concentration. Since all of the particles in the sample start sedimentation at the same place and time, particles of the same size all reach the detector beam at the same time. The time necessary to reach the detector beam versus beam intensity is converted to a size distribution using both Stokes' Law and Mie theory light scattering calculations. This method has an extremely high resolution (narrow particle families <2% different in size are partly resolved). The overall size range is from under 0.01 μm to more than 40 μm . Very accurate results with spherical particles are obtained. The measurement of low density particles is also possible. Absolute accuracy of the distribution depends on knowledge of optical properties and particle shape.

Capillary Hydrodynamic Fractionation (CHDF)

A very fine capillary tube with a few microns in diameter, carries a flow of emulsifier in water. At the start of an analysis, a very dilute suspension of particles is added to the flow just upstream of the capillary. As the particles move down the capillary they diffuse across the capillary tube due to the Brownian motion. The flow velocity profile within the capillary tube is approximately parabolic, with the highest velocity at the center. At any instant, a particle moves at a speed close to the speed of the fluid at that particle's center. The center of a particle of diameter D can only approach the capillary wall to a distance of $D/2$. On average, large particles have a higher velocity down the capillary than small particles, because large particles do not experience the lowest flow velocities that are near the capillary wall. Large particles reach the end of the capillary first, while very small particles reach the end last. A detector measures the concentration of particles as they exit the capillary. This method is mainly used for very small particle size (from 0.01 μm to maximum 1 - 2 μm) since larger particles have too little Brownian motion. Performance can be verified with calibration standards. This method has a very poor resolution (35% difference in size) and capillary plugging is a common problem. Non-spherical particles may not be correctly measured.

Sedimentation Field Flow Fractionation (SF3)

An SF3 instrument consists of a rotating disc that has a closed flow chamber located near the outside edge of the disc. Fluid is continuously pumped through the flow chamber while the disc is spinning at up to several thousand RPM. A

sample run begins with the disc spinning at the highest speed. The rotational rate is gradually reduced during the run. At the start of a run, a suspension of particles is added to the fluid stream. The particles are driven by a g-force toward the outside edge of the flow chamber when higher in density than the fluid, and toward the inside edge of the chamber when lower in density than the fluid. Large particles are closer towards the cell walls and small particles (with greater Brownian motion) form a cloud of particles that hover above the chamber wall. The liquid velocity profile inside the chamber is parabolic, so smaller particles spend more time in the higher velocity portions of the flow, and make faster progress (on average) along the chamber's length, exiting the chamber first just the opposite of CHDF. As the speed of rotation falls, the g-forces fall as well, allowing larger and larger particles to speed in the flow. There is a transition point where the g-forces become low enough that large particles (those too big to have significant Brownian motion) essentially roll or slide down the length of the chamber due to the lateral hydraulic force applied by the fluid flow. After this transition point is passed, larger particles move faster than smaller particles, because their centers are located at higher flow velocities than those of smaller particles (the same as CHDF). Particles are detected in the liquid flow leaving the chamber with a detector. The method has a broad dynamic range especially if both - Brownian and rolling - modes are included and very good resolution with small particles ($< 5 \mu m$). Narrow peaks as little as 5% different in size can be resolved. In Brownian mode, the particle geometry has no importance. The method employs a rather complicated algorithm for size separation and has a complicated mechanical construction.

For detailed information on the investigated sample, the methods that evaluate each particle at a time seem more appropriate, especially if the sample is a mixture of particles with different optical and/or geometrical characteristics. Most of the methods estimate the size of the particles, by reporting the equivalent spherical diameter, which leads to difficulties in accounting for particles that are not spheres and for structured particles (layers, cavities). The method that seems to inspire the greatest confidence in such cases is the direct microscope investigation and counting. This is the only method that allows for visualization of the particles and an evaluation of their range in shape and size. This method has the disadvantage that it is slow when is run by a human operator and yet

not very reliable when automated. None of the other methods can account for other geometrical parameters except the particle size. One such interesting geometrical parameter is the thickness of the layers in a multilayered particle. Using a microscope for estimating this parameter for more than a few particles is tedious. Elastic light scattering provides a possible way of characterizing this type of particles [3, 35, 36, 37, 54, 76, 94]. The common approach is to measure the elastic scattered light pattern for each particle at sufficient many different angular positions, so that the scattering pattern can be attributed without ambiguity to a certain combination in shape, size and internal structure. With each free parameter in this combination, the effort of finding the true particle shape-size-structure increases exponentially (if at all possible). The simplest scenario is a mono layered sphere. The two parameters that are to be determined are the core size and the shell thickness (*see* Fig. 1.1). This is the system considered for our application (*see* chapter 1). In the following chapters the software implementation and the hardware setup are described in detail.

Chapter 3

Elastic Light Scattering: Theoretical Considerations

The general problem of light scattering can be formulated in a rather simple way. The electromagnetic field with the electrical component \vec{E}_{inc} is incident on a scatterer of a certain volume, and creates the field inside the scatterer \vec{E}_t and a diffracted field \vec{E}_{sca} outside it (Fig. 3.1). Starting from the Maxwell equations (eq. A.1-A.4) one would find the total field \vec{E} equal to \vec{E}_t inside our volume and to $\vec{E}_{inc} + \vec{E}_{sca}$ outside, satisfying the boundary conditions on the surface of the considered volume.

Even if it seems simple, a concrete solution of the problem depends on the geometry and structure of the scatterer. Therefore, for characterizing light scattering by small particles various methods were developed whose applicability are constrained to the particular, concrete conditions for which they were created. For simple scenarios¹ analytical solutions were obtained and for more complicated scenarios approximations are employed. Both types of calculating methods involve non-trivial calculations and computational efforts.

¹addresses both geometry and optical properties

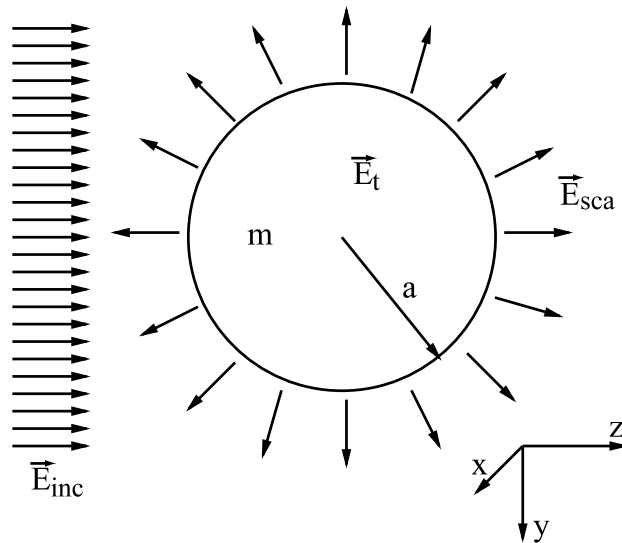


Figure 3.1: Elastic light scattering on a particle - general formulation

3.1 Numeric Methods

There is a wide range of methods used for calculating the elastic light scattering by single particles. A review of elastic light scattering theories is made by Wriedt [103]. For a quick overview on the available methods, we should proceed by differentiating between exact methods and approximate methods. Usually, for the exact methods, there is an analytical solution obtainable. Among the exact calculation methods, there are the separation of variables methods, the point matching methods, the integral equation methods, the coupled dipoles method (CDM), and the T-Matrix method (EBCM). In some cases even if the analytical solution is possible to be obtained numerical methods prove to be more efficient (e.g. for non-circular cylinders)

The separation of variables methods were the first employed for elastic light scattering calculations. They are used for particles with simple geometry, being either spheres, spheroids or cylinders. Scattering of plane waves on homogeneous spheres is covered by the initial theory developed by Mie [52] and Debye [19]. Extensions of this theory covering magnetic spheres [39], layered spheres [3, 35, 36, 37, 54, 94], inhomogeneous spheres [102, 104, 105], spheres made of optic active materials [12] and spheres illuminated with a Gaussian focused beam [26, 51] are available. For spheres made of anisotropic material there is no gen-

eral solution of Mie type available [11]. For infinite cylinders and perpendicular incidence, Rayleigh [68] arrived at a solution in 1918 and half a century later Wait [93] published the solution for oblique incidence. Other works address in detail the scattering on homogeneous cylinders [2, 9, 47, 78], layered cylinders [4, 22, 35, 38] and also on spheroids [5, 46, 78] and ellipsoids [45].

The point matching methods are overviewed by Bates *et al.* [8] and for integral equation methods there is a rich literature since these methods are the starting point for other approaches like the method of moments, the T-matrix method or the Rayleigh-Debye-Gans(RDG) theory [7, 60, 86]. From the integral equations one can calculate scattering and absorption for particles of different shape and structure (cube [34], discs [42], thin rods [91], aggregates of spheres [16] etc.).

A very powerful exact method is the coupled dipoles method (CDM) known also as Purcell-Pennypacker method, one of the most popular method in the theory of light scattering due to its large applicability [43, 65]. Another very efficient method is the T-Matrix known as Extended Boundary Condition Method (EBCM). A review on this subject, with comprehensive references was made by Mishchenko *et al.* [55].

The approximate methods are related to certain regions of values for the diffraction parameters like the size parameter x (see A.5) and the relative refractive index m . For example, if $x \ll 1$ and $x \cdot |m| \ll 1$ then one has the Rayleigh approximation² [67]. Variations from this approximation are Rayleigh-Gans-Stevenson (RGS)³, Rayleigh-Debye-Gans (RDG)⁴ known also as Rayleigh-Gans-Born, Rayleigh-Gans-Rokard or Born approximation. There are also generalizations of RDG approximation [13].

Other approximate methods are: the anomalous diffraction approximation (AD)⁵ with its generalizations WKB⁶ and eikonal approximations. For relatively large particles the geometrical optics (GO) approximation can be employed. A partially discarded method is the perturbation method [109].

All these methods can be used in different combinations raising hybrid approximations which are used for specific scattering problems or for obtaining similarly results with less computational effort [45, 46].

²the particle can be considered as an elementary dipole

³generalized Rayleigh approximation

⁴when $|m - 1| \ll 1$ and $\rho \ll 1$ where ρ is the phase shift $\rho = 2x(m - 1)$

⁵ for $x \gg 1$ and $m \sim 1$

⁶Wentzel-Kramers-Brillouin

3.2 Mie Theory

The scattering of light from a spherical object has been dealt with by many investigators since the classic solution for homogeneous sphere was suggested in 1899 by A.E.N. Love [50] and brought to conclusion by G. Mie in 1908 [52] and independently by P. Debye in 1909 [19]. Traditionally the theory of light scattering from a sphere is referred to as Mie theory and has become an important tool for diagnosing microparticles or aerosol particles in different environments. The formal solution by Mie assumed that the object is composed of a homogeneous, isotropic and optically linear material irradiated by an infinitely extending plane wave. Generally, the Mie theory is therefore restricted to spherical, isotropic, homogeneous and non-magnetic particles in a non-absorbing medium.

3.2.1 General Formalism

From the Maxwell equations (eq. A.1-A.4) by applying the rotor operator on eq. A.3 and eq. A.3 one arrives at:

$$\Delta \vec{E} - \epsilon_r \epsilon_0 \mu_r \mu_0 \frac{\partial^2 \vec{E}}{\partial t^2} - \mu_r \mu_0 \sigma \frac{\partial \vec{E}}{\partial t} = 0, \quad (3.1)$$

$$\Delta \vec{H} - \epsilon_r \epsilon_0 \mu_r \mu_0 \frac{\partial^2 \vec{H}}{\partial t^2} - \mu_r \mu_0 \sigma \frac{\partial \vec{H}}{\partial t} = 0, \quad (3.2)$$

where σ is the electric conductivity of the medium, ϵ_0 and μ_0 are the permittivity and the permeability of vacuum, while ϵ_r and μ_r are the relative permittivity and the relative permeability for the medium. By considering the fields as harmonic of type $\sim e^{i\omega t}$ one obtains $\Delta \psi + k^2 \psi = 0$ which is the scalar wave equation (Helmholtz).

For a solution ψ of the scalar wave equation, two linear independent solutions for the vectorial equations 3.1 and 3.2 can be constructed. These are:

$$\vec{M} = \nabla \times (\vec{c}\psi), \quad (3.3)$$

$$\vec{N} = \frac{1}{k} \nabla \times \vec{M}, \quad (3.4)$$

where \vec{c} is a constant vector.

For an optically linear media where the superposition principle holds true, an

electromagnetic field can be written as a linear combination of different fields (multipole expansion).

$$\vec{E} = E_0 \sum_n \left(a_n \vec{M}_n + b_n \vec{N}_n \right), \quad (3.5)$$

where a_n and b_n are the multipole coefficients. In the following, only the electric field will be considered (the magnetic field \vec{H} is linked with \vec{E} by the Maxwell equations A.1-A.4).

3.2.2 Mie Expansion Coefficients for a Homogeneous Sphere

Expressing the incident (\vec{E}_{inc}), transmitted (\vec{E}_t) and scattered (\vec{E}_{sca}) field (see Fig. 3.1) in the multipole expansion (eq. 3.5) and using the vectorial spherical harmonic functions (eq. A.21 and A.22) one arrives at:

$$\vec{E}_{inc} = E_0 \sum_{n=1}^{\infty} i^{n-1} \frac{2n+1}{n(n+1)} \left(\vec{N}_{en}^{(inc)} + i \vec{M}_{on}^{(inc)} \right), \quad (3.6)$$

by considering \vec{E}_{inc} as linear polarized in the x direction propagating in the z - direction (see Fig. 3.1), it follows:

$$\vec{E}_{sca} = E_0 \sum_{n=1}^{\infty} i^{n-1} \frac{2n+1}{n(n+1)} \left(a_n \vec{N}_{en}^{(sca)} + i b_n \vec{M}_{on}^{(sca)} \right) \quad (3.7)$$

and

$$\vec{E}_t = E_0 \sum_{n=1}^{\infty} i^{n-1} \frac{2n+1}{n(n+1)} \left(d_n \vec{N}_{en}^{(t)} + i c_n \vec{M}_{on}^{(t)} \right), \quad (3.8)$$

where the expansion coefficients a_n , b_n , c_n and d_n are to be determined. The way the Bessel functions are chosen for the vectorial spherical harmonic functions (\vec{M} and \vec{N} eq. A.21-A.22) is described by Bohren and others [11, 37, 81, 82]. For simplifying the final equations, the Riccati-Bessel functions are introduced (see appendix A for notations and substitutions):

$$\psi_n(\rho) = \rho j_n(\rho), \quad (3.9)$$

$$\chi_n(\rho) = \rho y_n(\rho), \quad (3.10)$$

$$\xi_n(\rho) = \rho h_n^{(2)}(\rho). \quad (3.11)$$

The expansion coefficients a_n , b_n , c_n and d_n are determined by resolving the equation system given by the boundary condition which states that the tangential component of \vec{E} and \vec{H} be continuous across the spherical surface of the particle. For our spherical geometry only the E_θ , E_ψ and H_θ , H_ψ components have tangential contributions and therefore the four boundary equations are

$$E_{\theta,inc} + E_{\theta,sca} = E_{\theta,t}, \quad (3.12)$$

$$E_{\phi,inc} + E_{\phi,sca} = E_{\phi,t}, \quad (3.13)$$

$$H_{\theta,inc} + H_{\theta,sca} = H_{\theta,t}, \quad (3.14)$$

$$H_{\phi,inc} + H_{\phi,sca} = H_{\phi,t}, \quad (3.15)$$

which, by using the Riccati-Bessel functions (eq. 3.9- 3.11) translates to:

$$\psi_n(mx)c_n + m\xi_n(x)b_n = m\psi_n(x), \quad (3.16)$$

$$\psi'_n(mx)c_n + \xi'_n(x)b_n = \psi'_n(x), \quad (3.17)$$

$$\psi_n(mx)d_n + \xi_n(x)a_n = \psi_n(x), \quad (3.18)$$

$$\psi'_n(mx)d_n + m\xi'_n(x)a_n = m\psi'_n(x). \quad (3.19)$$

The solution for this system is

$$a_n = \frac{m\psi_n(mx)\psi'_n(x) - \psi_n(x)\psi'_n(mx)}{m\psi_n(mx)\xi'_n(x) - \xi_n(x)\psi'_n(mx)}, \quad (3.20)$$

$$b_n = \frac{\psi_n(mx)\psi'_n(x) - m\psi_n(x)\psi'_n(mx)}{\psi_n(mx)\xi'_n(x) - m\xi_n(x)\psi'_n(mx)}, \quad (3.21)$$

$$c_n = \frac{-im}{\psi_n(mx)\xi'_n(x) - m\xi_n(x)\psi'_n(mx)}, \quad (3.22)$$

$$d_n = \frac{-im}{m\psi_n(mx)\xi'_n(x) - \xi_n(x)\psi'_n(mx)}. \quad (3.23)$$

The characteristic modes for a spherical particles are called morphology dependent resonances or MDR's. These resonance locations can be determined by calculating the poles of the expansion coefficients a_n and c_n given by equations

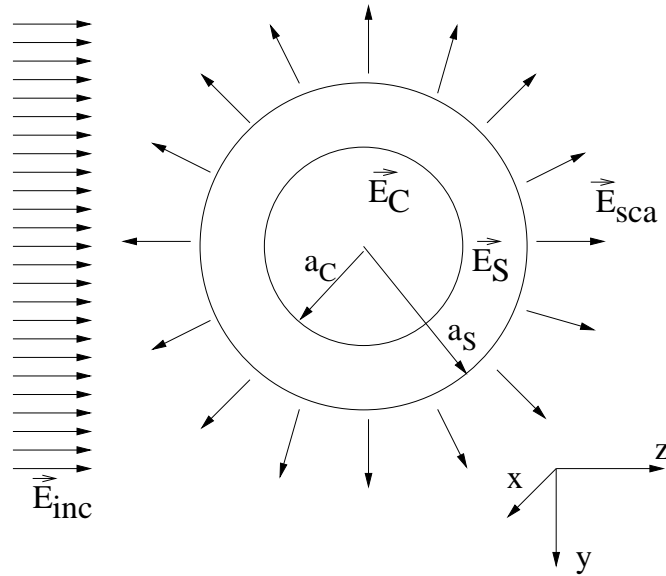


Figure 3.2: Monolayered microparticle with a core having a relative refractive index m_C and radius a_C . The shell has a relative refractive index m_S and radius a_S . The incident field \vec{E}_{inc} , scattered \vec{E}_{sca} , and the internal created fields \vec{E}_C , \vec{E}_S are schematic represented.

(3.20) and (3.22) (the denominators of b_n and d_n are the same as those of c_n and a_n).

3.3 Extensions of Mie Theory to Coated Spheres

The generalization of the Mie theory for core-mantle spheres was made in 1950's by A.L. Aden and M. Kerker [3] and K.S. Shifrin [81]. For the case of an arbitrary number of layers, solutions were presented by Mikulski and Murphy [53] and Wait [94] in 1963. Detailed results for layered spheres are presented by Kerker *et al.* [35, 36, 37]. For an inhomogeneous sphere with an arbitrary radial distribution of the refractive index, the general formal solution was obtained by Wyatt [104, 105]. A core-mantle sphere as the model of biological particles was also considered by Brunsting and Mullaney [15].

3.3.1 Mie Expansion Coefficients for a Monolayered Sphere

The scattering geometry for a coated sphere is pictured in Fig. 3.2. The core has a radius a_C and a relative refractive index⁷ m_C , the shell having a radius a_S and a relative refractive index m_S . The internal electrical fields are \vec{E}_C respectively \vec{E}_S with the incident field \vec{E}_{inc} being linear polarized in the x direction propagating alongside z . The scattered field is \vec{E}_{sca} . The boundary conditions are the same as for a homogeneous particle (eq. 3.12- 3.15) with the only difference that the equations are written for both surfaces (core - shell, shell-medium).

Therefore, one obtains:

$$E_{\theta,C} = E_{\theta,S}, \quad (3.24)$$

$$E_{\phi,C} = E_{\phi,S}, \quad (3.25)$$

$$H_{\theta,C} = H_{\theta,S}, \quad (3.26)$$

$$H_{\phi,C} = H_{\phi,S}, \quad (3.27)$$

$$E_{\theta,inc} + E_{\theta,sca} = E_{\theta,S}, \quad (3.28)$$

$$E_{\phi,inc} + E_{\phi,sca} = E_{\phi,S}, \quad (3.29)$$

$$H_{\theta,inc} + H_{\theta,sca} = H_{\theta,S}, \quad (3.30)$$

$$H_{\phi,inc} + H_{\phi,sca} = H_{\phi,S}. \quad (3.31)$$

After the multipole expansion for the incident field (eq. 3.6), for the scattered field (eq. 3.7), as well as for the internal electrical fields \vec{E}_C and \vec{E}_S :

$$\vec{E}_C = E_0 \sum_{n=1}^{\infty} i^{n-1} \frac{2n+1}{n(n+1)} \left(g_n \vec{N}_{en}^{(j)} + i h_n \vec{M}_{on}^{(j)} \right), \quad (3.32)$$

$$\vec{E}_S = E_0 \sum_{n=1}^{\infty} i^{n-1} \frac{2n+1}{n(n+1)} \left(i \epsilon_n \vec{M}_{on}^{(j)} + c_n \vec{N}_{en}^{(j)} + i f_n \vec{M}_{on}^{(h(2))} + d_n \vec{N}_{en}^{(h(2))} \right), \quad (3.33)$$

the boundary conditions will transform in:

$$m_C c_n \psi'_n(m_S x_C) + m_C d_n \xi'_n(m_S x_C) - m_S g_n \psi'_n(m_C x_C) = 0, \quad (3.34)$$

$$c_n \psi_n(m_S x_C) + d_n \xi_n(m_S x_C) - g_n \psi_n(m_C x_C) = 0, \quad (3.35)$$

$$c_n \psi'_n(m_S x_S) + d_n \xi'_n(m_S x_S) + m_S a_n \xi'_n(x_S) = m_S \psi'_n(x_S), \quad (3.36)$$

⁷relative to the medium in which the particle is placed

$$c_n \psi_n(m_S x_S) + d_n \xi_n(m_S x_S) + a_n \xi_n(x_S) = \psi_n(x_S), \quad (3.37)$$

$$m_C e_n \psi'_n(m_S x_C) + m_C f_n \xi'_n(m_S x_C) - m_S h_n \psi'_n(m_C x_C) = 0, \quad (3.38)$$

$$m_C^2 e_n \psi_n(m_S x_C) + m_C^2 f_n \xi_n(m_S x_C) - m_S^2 h_n \psi_n(m_C x_C) = 0, \quad (3.39)$$

$$e_n \psi'_n(m_S x_S) + f_n \xi'_n(m_S x_S) + m_S b_n \xi'_n(x_S) = m_S \psi'_n(x_S), \quad (3.40)$$

$$e_n \psi_n(m_S x_S) + f_n \xi_n(m_S x_S) + m_S^2 b_n \xi_n(x_S) = m_S^2 \psi_n(x_S). \quad (3.41)$$

where x_C and x_S are the Mie size parameters for the core and shell and ψ_n and ξ_n are the Ricatti-Bessel functions (*see* eq. 3.9 - 3.11).

Resolving this system of equations and by defining the following notations:

$$A_n = \frac{m_S \psi'_n(m_C x_C) \psi_n(m_S x_C) - m_C \psi_n(m_C x_C) \psi'_n(m_S x_C)}{m_S \psi'_n(m_C x_C) \xi_n(m_S x_C) - m_C \psi_n(m_C x_C) \xi'_n(m_S x_C)}, \quad (3.42)$$

$$B_n = \frac{m_S \psi'_n(m_S x_C) \psi_n(m_C x_C) - m_C \psi_n(m_S x_C) \psi'_n(m_C x_C)}{m_S \xi'_n(m_S x_C) \psi_n(m_C x_C) - m_C \xi_n(m_S x_C) \psi'_n(m_C x_C)}, \quad (3.43)$$

the expansion coefficients for the scattered field a_n and b_n are:

$$a_n = \frac{\psi_n(x_S) [\psi'_n(m_S x_S) - A_n \xi'_n(m_S x_S)] - m_S \psi'_n(x_S) [\psi_n(m_S x_S) - A_n \xi_n(m_S x_S)]}{\xi_n(x_S) [\psi'_n(m_S x_S) - A_n \xi'_n(m_S x_S)] - m_S \xi'_n(x_S) [\psi_n(m_S x_S) - A_n \xi_n(m_S x_S)]}, \quad (3.44)$$

$$b_n = \frac{m_S \psi_n(x_S) [\psi'_n(m_S x_S) - B_n \xi'_n(m_S x_S)] - \psi'_n(x_S) [\psi_n(m_S x_S) - B_n \xi_n(m_S x_S)]}{m_S \xi_n(x_S) [\psi'_n(m_S x_S) - B_n \xi'_n(m_S x_S)] - \xi'_n(x_S) [\psi_n(m_S x_S) - B_n \xi_n(m_S x_S)]}, \quad (3.45)$$

and for the internal fields:

$$c_n = \frac{m_S \psi'_n(x_S) \xi_n(x_S) - m_S \psi_n(x_S) \xi'_n(x_S)}{\xi_n(x_S) [\psi'_n(m_S x_S) - A_n \xi'_n(m_S x_S)] - m_S \xi'_n(x_S) [\psi_n(m_S x_S) - A_n \xi_n(m_S x_S)]}, \quad (3.46)$$

$$d_n = \frac{A_n [m_S \xi'_n(x_S) \psi_n(x_S) - m_S \xi_n(x_S) \psi'_n(x_S)]}{\xi_n(x_S) [\psi'_n(m_S x_S) - A_n \xi'_n(m_S x_S)] - m_S \xi'_n(x_S) [\psi_n(m_S x_S) - A_n \xi_n(m_S x_S)]}, \quad (3.47)$$

$$g_n = \frac{G_n [m_S \psi'_n(x_S) \xi_n(x_S) - m_S \psi_n(x_S) \xi'_n(x_S)]}{\xi_n(x_S) [\psi'_n(m_S x_S) - A_n \xi'_n(m_S x_S)] - m_S \xi'_n(x_S) [\psi_n(m_S x_S) - A_n \xi_n(m_S x_S)]}, \quad (3.48)$$

$$e_n = \frac{m_S [m_S \psi'_n(x_S) \xi_n(x_S) - m_S \psi_n(x_S) \xi'_n(x_S)]}{m_S \xi_n(x_S) [\psi'_n(m_S x_S) - B_n \xi'_n(m_S x_S)] - \xi'_n(x_S) [\psi_n(m_S x_S) - B_n \xi_n(m_S x_S)]},$$

$$f_n = \frac{m_S B_n [m_S \psi_n(x_S) \xi'_n(x_S) - m_S \psi'_n(x_S) \xi_n(x_S)]}{m_S \xi_n(x_S) [\psi'_n(m_S x_S) - B_n \xi'_n(m_S x_S)] - \xi'_n(x_S) [\psi_n(m_S x_S) - B_n \xi_n(m_S x_S)]}, \quad (3.49)$$

$$(3.50)$$

$$h_n = \frac{m_S H_n [m_S \psi'_n(x_S) \xi_n(x_S) - m_S \psi_n(x_S) \xi'_n(x_S)]}{m_S \xi_n(x_S) [\psi'_n(m_S x_S) - B_n \xi'_n(m_S x_S)] - \xi'_n(x_S) [\psi_n(m_S x_S) - B_n \xi_n(m_S x_S)]}, \quad (3.51)$$

where the G_n and H_n notations are:

$$G_n = \frac{m_C \psi'_n(m_S x_C) \xi_n(m_S x_C) - m_C \psi_n(m_S x_C) \xi'_n(m_S x_C)}{m_S \psi'_n(m_C x_C) \xi_n(m_S x_C) - m_C \psi_n(m_C x_C) \xi'_n(m_S x_C)}, \quad (3.52)$$

$$H_n = \frac{m_C \xi'_n(m_S x_C) \psi_n(m_S x_C) - m_C \xi_n(m_S x_C) \psi'_n(m_S x_C)}{m_S \xi'_n(m_S x_C) \psi_n(m_C x_C) - m_C \xi_n(m_S x_C) \psi'_n(m_C x_C)}. \quad (3.53)$$

The resonance locations can be determined by calculating the poles of the expansion coefficients, a_n , c_n , d_n and g_n .

3.4 Far Field Intensity: Phase Function

By expressing the scattered field from eq. 3.7 and using the solutions for the vectorial wave equation (A.21 - A.22) and the angular functions π_n and τ_n (A.23 - A.24) one arrives at:

$$E_{r,sca} = E_0 \frac{\cos \phi}{(kr)^2} \sum_{n=1}^{\infty} i^{n-1} (2n+1) a_n \xi_n(kr) \pi_n \sin \theta, \quad (3.54)$$

$$E_{\theta,sca} = E_0 \frac{\cos \phi}{kr} \sum_{n=1}^{\infty} i^{n-1} \frac{2n+1}{n(n+1)} \left(a_n \xi'_n(kr) \tau_n + i b_n \xi_n(kr) \pi_n \right), \quad (3.55)$$

$$E_{\phi,sca} = -E_0 \frac{\sin \phi}{kr} \sum_{n=1}^{\infty} i^{n-1} \frac{2n+1}{n(n+1)} \left(a_n \xi'_n(kr) \pi_n + i b_n \xi_n(kr) \tau_n \right). \quad (3.56)$$

Detecting the scattered light is normally accomplished by positioning light sensitive detectors at a certain distance from the scattering system. If detection is

performed at a distance r from the scatterer, for which [11, eq. 4.75]:

$$kr \gg \left(\frac{d}{\lambda}\right)^2, \quad (3.57)$$

where d is the size (e.g. diameter) of the scattering system and λ is the wavelength of light used for investigation, then the Ricatti-Bessel functions which describe the field can be expressed as [11]:

$$\xi_n(kr) = i^{n+1} \exp(-ikr), \quad (3.58)$$

$$\xi'_n(kr) = i^n \exp(-ikr). \quad (3.59)$$

The radial component $\vec{E}_{r,sca}$ is proportional with kr^{-2} while $\vec{E}_{\theta,sca}$ and $\vec{E}_{\phi,sca}$ with kr^{-1} , and therefore, one can consider in the far field approximation only the contribution of $\vec{E}_{\theta,sca}$ and $\vec{E}_{\phi,sca}$. The values of these two components are then:

$$E_{\theta,sca} = E_0 \frac{e^{-ikr} \cos \phi}{ikr} \sum_{n=1}^{\infty} \frac{2n+1}{n(n+1)} (a_n \tau_n + b_n \pi_n), \quad (3.60)$$

$$E_{\phi,sca} = -E_0 \frac{e^{-ikr} \sin \phi}{ikr} \sum_{n=1}^{\infty} \frac{2n+1}{n(n+1)} (a_n \pi_n + b_n \tau_n). \quad (3.61)$$

where the transport factor $(e^{-ikr})/ikr$ will be a constant if the detection is performed on a circular sector around the particle. The signal detected will be $I = \langle E \cdot E^* \rangle$ and when normalized to the incident intensity one obtains:

$$i_{\theta} = i_{\parallel} = \left| \sum_{n=1}^{\infty} \frac{2n+1}{n(n+1)} (a_n \tau_n + b_n \pi_n) \right|^2 \cos^2 \phi, \quad (3.62)$$

$$i_{\phi} = i_{\perp} = \left| \sum_{n=1}^{\infty} \frac{2n+1}{n(n+1)} (a_n \pi_n + b_n \tau_n) \right|^2 \sin^2 \phi, \quad (3.63)$$

where \parallel and \perp refer to the polarization of the scattered field relative to the scattering plane. One can observe that the polarization direction for the detected field is the same as for the incident field. For angles of detection other than $\theta = 0^\circ$ and $\theta = 90^\circ$ relative to the polarization direction of \vec{E}_{inc} , a combined contribution of i_{θ} and i_{ϕ} from the above expressions (3.62-3.63) has to be considered.

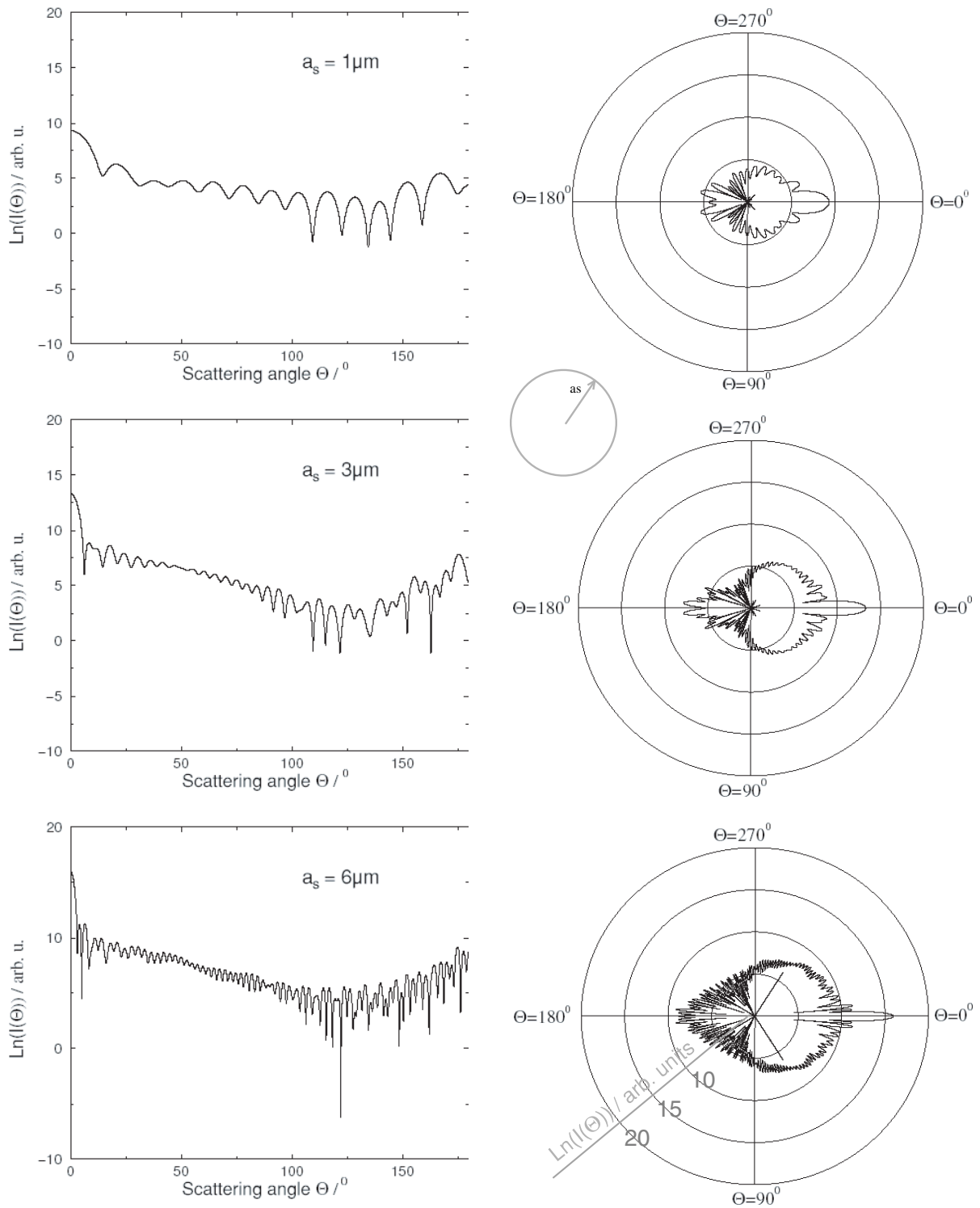


Figure 3.3: The phase functions for homogeneous microparticles of 1, 3 and 6 μm radius presented in chartesian (left column) and polar coordinates (right column). The laser propagates from $\Theta = 180^\circ$ (backscattering) to $\Theta = 0^\circ$ (forward scattering). The relative refractive index is $m = 1.5$ and the laser line $\lambda = 514 \text{ nm}$.

The representation of the intensity for the scattered field as a function of scattering angle is known as a phase function. In Fig. 3.4 the phase functions for three homogeneous particles with a size of 1, 3 and 6 μm are presented using a logarithmic scale. On the whole, making abstraction of the intensity values and fine structure, the three phase functions show high scattered intensities in the forward as well as backward direction. The smallest intensities are usually in the region of $100^\circ - 140^\circ$. The scattering pattern is very sensitive to almost all parameters that describe the system (relative refractive index, size of the core and shell, mode of the incident laser, etc.) and therefore, these phase functions can be used for identifying some of the parameters of the scattering system. One possibility of resolving the inverse problem⁸ of elastic light scattering is to have a complete set of phase functions covering all possible scattering patterns for a partially known system. In our case (*see* Chap. 1), the system consists of particles of known refractive index with an unknown size for the core radius and shell thickness. Therefore by having enough calculated phase functions for different core and shell sizes one can eventually infer these parameters for a scattering system from its scattering pattern with the condition that the system is of that specific type (i.e. monolayered sphere) and included in the database. It is well known that the Mie theory is inadequate for calculating scattering properties of nonspherical particles [55]. It is therefore anticipated that the Mie theory-based instruments may produce spurious size distributions in the presence of nonspherical particles.

⁸inferring the scattering system's properties from the scattering pattern

Chapter 4

Experimental Realization

The basic principle of measuring consists of analyzing one particle at a time by recording the elastic light scattering pattern at angles between approx. 60° and 120° . The identification of the two parameters of interest, a_C and a_S (see Fig. 1.1) is made by comparing the experimentally recorded phase functions with the previously calculated phase functions stored in a database. In the context of the sizing methods presented in chapter 2, our approach is in the class of the counting methods¹. For automating the measurement process and for being able to measure in this configuration, an extremely high purity of the investigated sample is required in the way that the scatterer geometries that are included into the database (e.g. particles with a_C from 1 to 4 μm and a_S from 3 to 5 μm made out of known material²) are the only ones that should be present in the investigated sample. Every other particle that is measured and not represented in the database, in the best case, increases the noise of the measurement, or it

¹normally all the methods based on elastic light scattering are ensemble methods

²the relative refractive index has to be known as well as absorption at the used laser wavelength

leads to counts incorrectly attributed preferentially to a specific particle size³. Furthermore the particle aggregation leads to false counts.

For a functional system, corrections and adaptations have to be made from the hardware side in order to reduce the strain on the computational efforts and from the software side in order to compensate the errors introduced by the experimental setup.

4.1 Experimental Setup

The experimental setup as shown in Figure 4.1 is based on a flow cell, through which the spherical capsules are circulated, suspended in a liquid medium of known refractive index. Carried by the flowing liquid, the particles are brought into a laser beam. The scattered light is collected by an optical system and further projected on two detector arrays. One of the detectors receives the real image of the particle in the laser beam and the other detector receives a defocused image of the same particle. The scattering plane is defined by the laser beam and the optical axis of the collecting optics system. The laser polarization is perpendicular relative to this plane and, therefore, the scattered field in the far field approximation should have the same polarization⁴(see section 3.4).

A detailed description for each major component in the experimental setup follows with emphasis on the experimental phase function recordable with these components. The required corrections for matching the experimental scattering pattern with the calculated phase function are further discussed.

4.1.1 Laser

The laser used is a solid state laser (PDL-DPGL-532-50 from Polytec) operating at 532 nm with a power of approx. 50 mW and a laser linewidth of approx. 0.35nm. The wavelength of the laser was chosen to be towards the blue end of the visible spectra having at the same time enough power to make small particles visible for the employed detectors when using exposure times under 1 *ms*. The shorter the wavelength used for scattering experiments, the richer in features (minima, maxima) is the scattering pattern for a given angular interval.

³usually theoretical phase functions for small particles fit the 'false' counts with a lower error

⁴if detection is made strictly in this plane

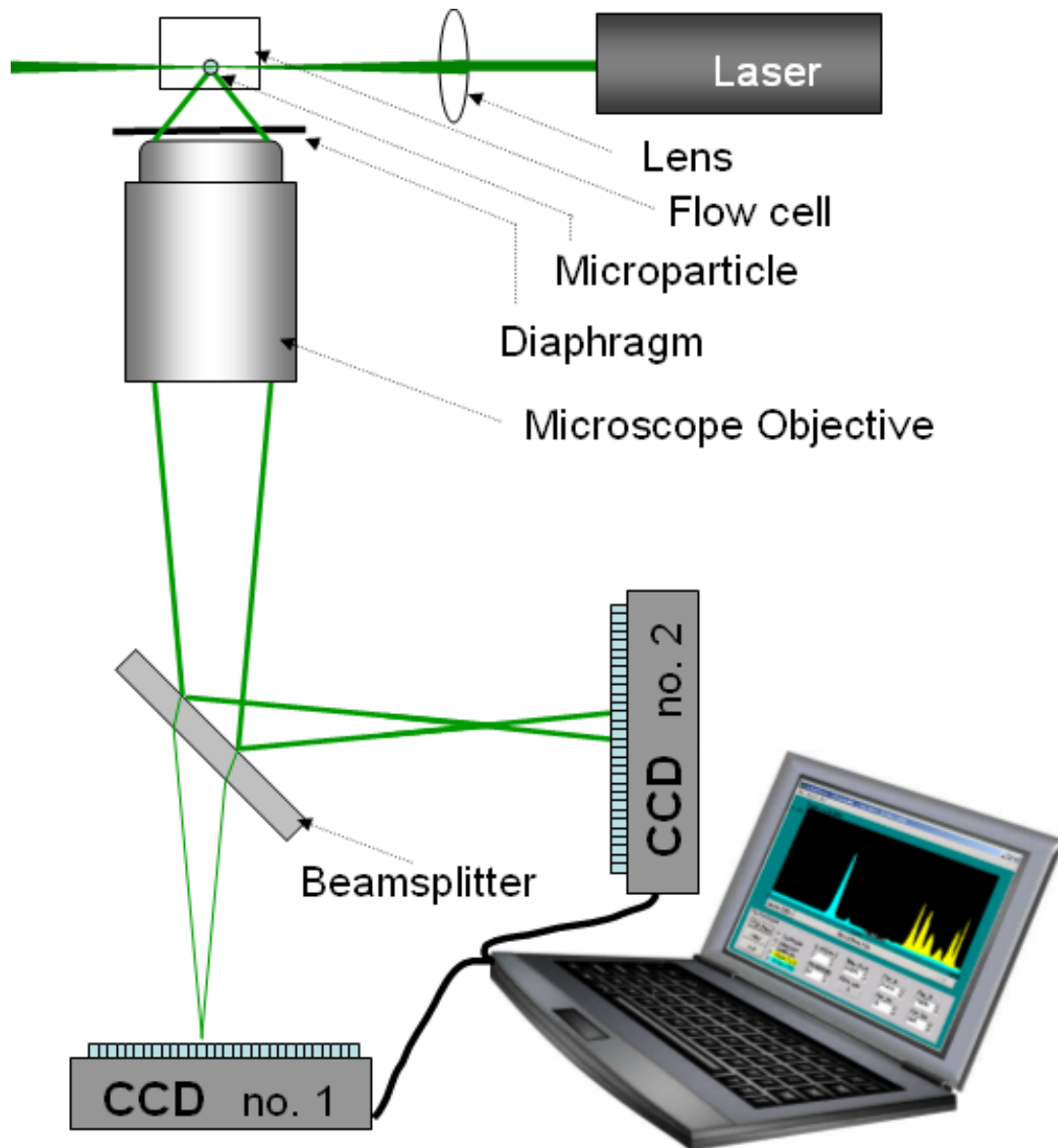


Figure 4.1: Basic experimental setup of the microcapsule analyzer device.

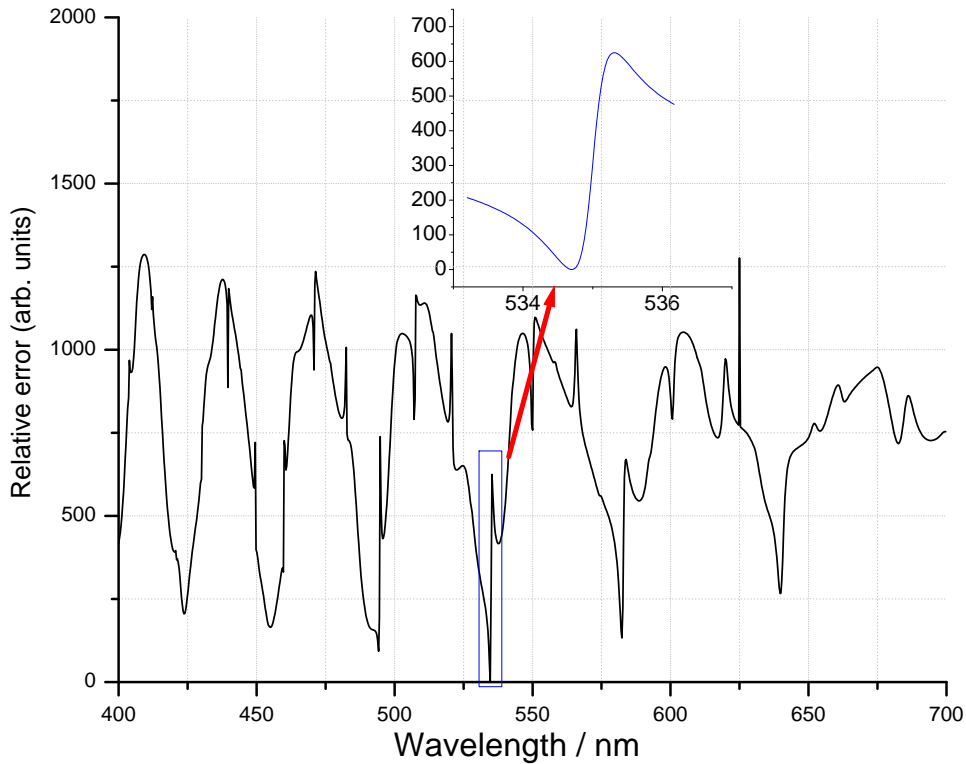


Figure 4.2: Fitting error vs laser wavelength. The considered particle is homogeneous with a radius of $2.5 \mu\text{m}$ and a refractive index of 1.33 placed in air. The detection is considered from 60° to 120° in 700 equidistant points. The error is considered between the theoretical calculated phase function at the laser central wavelength (534.7 nm) and the theoretical phase functions expected as the central laser wavelength is shifting.

Monochromaticity

The monochromaticity of the laser light is an important factor that has to be considered when comparing the theoretical phase functions with the measured scattering patterns, especially for particular particle sizes as explained in the following. For illustration the theoretical phase function for a particle of $5 \mu\text{m}$ diameter and refractive index $m = 1.33$ was calculated using a laser wavelength of 534.7 nm . This theoretical phase function was compared with the theoretical phase functions calculated at other different laser wavelengths. In Fig. 4.2 this comparison is shown as the error of fitting⁵ versus the wavelength used for generating the phase function. Of interest in this graph are the sudden jumps of the

⁵fitting the first calculated phase function (at 534.7 nm) with every other phase function

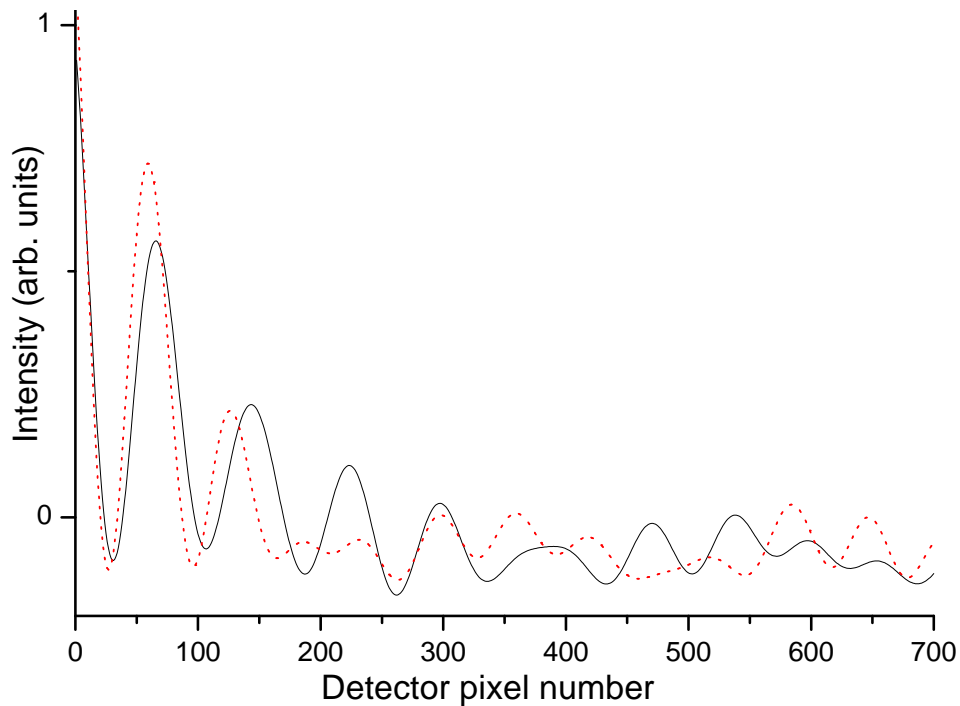


Figure 4.3: Phase functions for the same particle using two different laser linewidths. The dotted line is the scattering pattern measured with a perfectly monochrome laser (534.7 nm) and the continuous line is the phase function for the same particle when using a laser centered at 534.7 nm with a spectral linewidth of 1 nm and a lorentzian spectral profile. The considered particle is a water drop of 2.5 μm radius placed in air and measured from 60° to 120° in 700 equidistant points.

fitting error (as shown in the subgraph Fig. 4.2). The difference in fitting error from a best fit (error=0) to a local maximum of 600 on a relative scale (maximum achievable error was 1300) occurs for a difference in λ of roughly 0.5 nm. If the laser (with a non zero linewidth) is spectrally overlapping one of these 'sudden jumps' the experimentally recorded scattering pattern will hardly resemble the theoretical phase function calculated for a perfect monochromatic laser. The theoretical difference is shown in Fig. 4.3. The laser linewidth was 'overestimated' at 1 nm for illustration purposes. The scattering pattern for the 'real' laser was obtained by calculating the scattering patterns at different wavelengths inside the laser linewidth and then making a weighted sum (the laser spectral profile was considered to be lorentzian). A few calculated phase functions at different wavelengths inside the laser linewidth are shown in Fig. 4.4. The differences are due

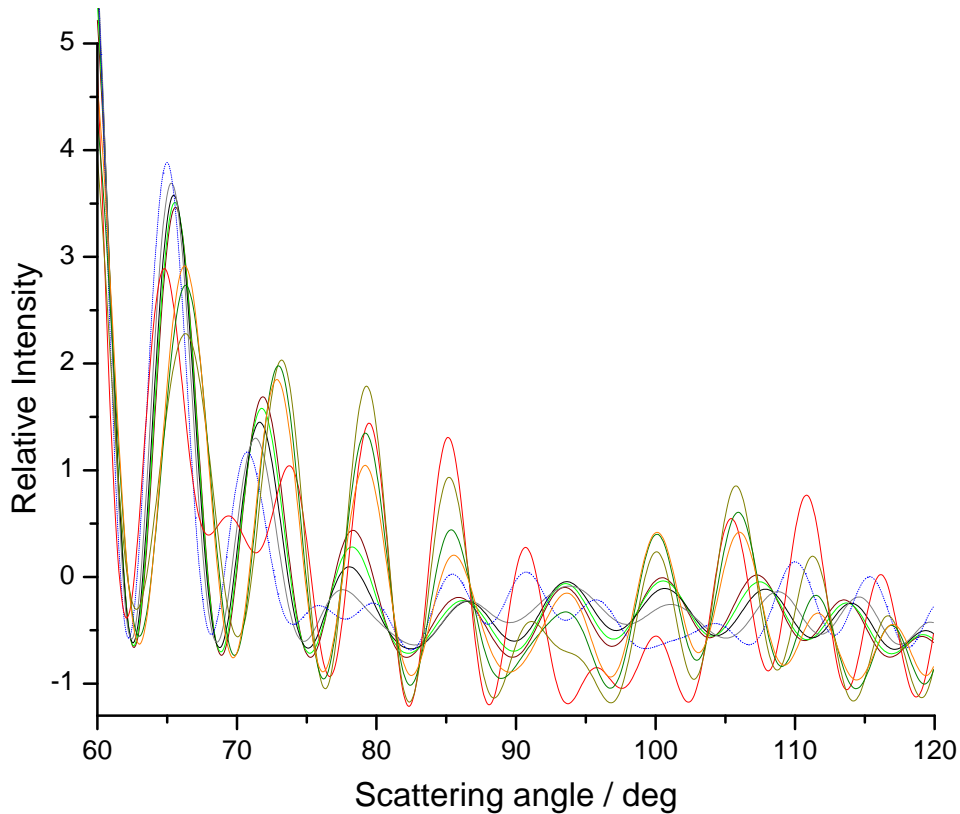


Figure 4.4: Phase functions for the same particle calculated by using nine different laser line positions into the laser spectral linewidth of 1 nm (from 534.2 nm to 535.2 nm). The considered particle is a water drop of $2.5 \mu\text{m}$ radius placed in air and measured from 60° to 120° in 700 equidistant points.

to the formation of MDR's (*see* sec. 3.2.2). This behavior is characteristic only for a reduced set of particle sizes at a specific laser wavelength and laser width. For the case described here, with a laser centered at 532.05 nm having a linewidth of 0.35 nm the specific sizes⁶ for which this behavior have to be considered are shown in Fig. 4.5. When the combination of core size and shell thickness is taken into account the previous reduced set of sizes for which the theory is no longer fitting the experiment is considerably enlarged.

A possibility for correcting this effect is to calculate the above described weighted sum for specific sizes and use the result as the attributed phase function inside the database. The drawback is a longer time necessary for building the database.

⁶here only for homogeneous spheres

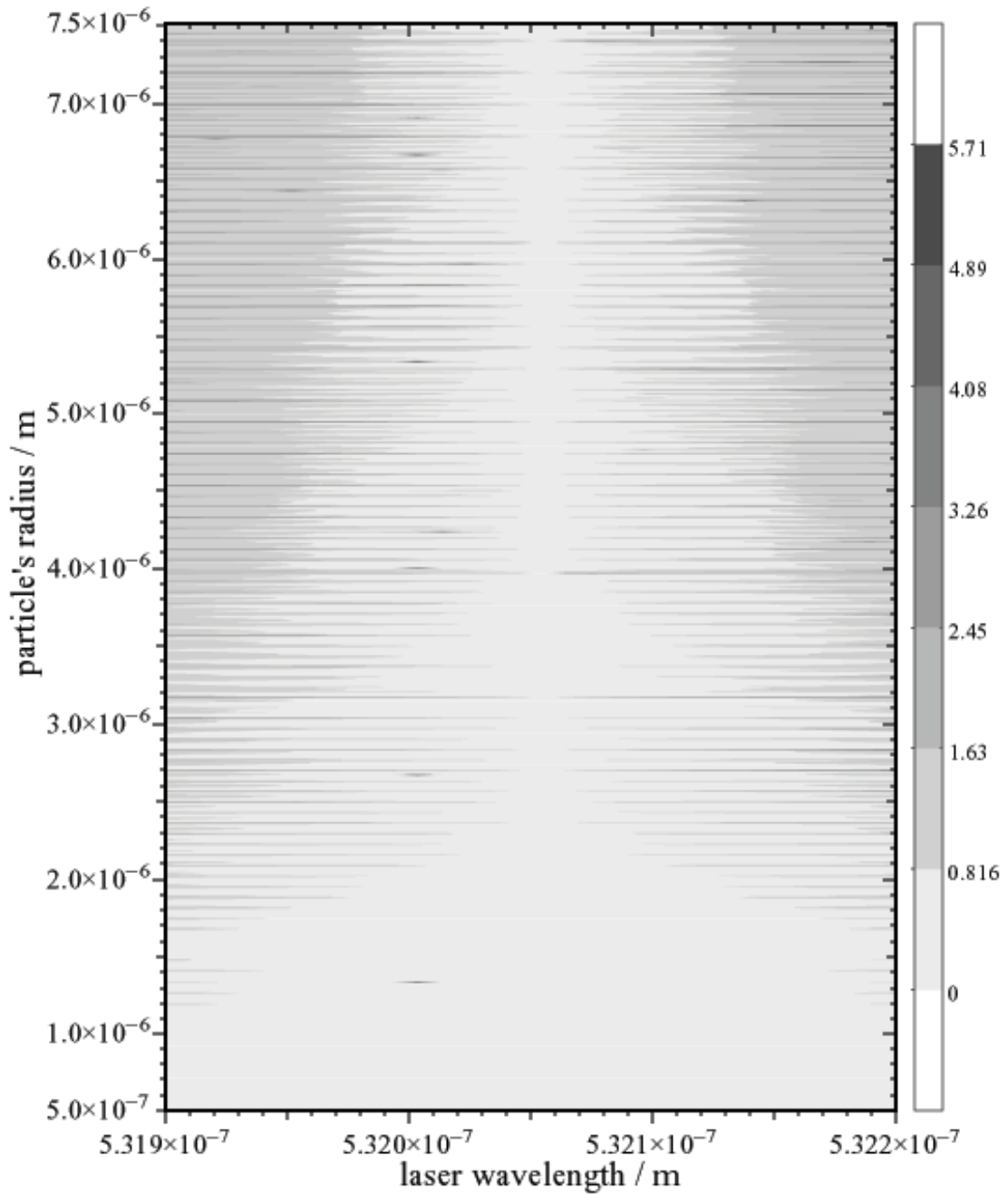


Figure 4.5: For each homogeneous particle with $m = 1.33$ and radius in the range of $0.5 \mu\text{m}$ to $7.5 \mu\text{m}$ the phase function calculated for a monochromatic laser at 532.05 nm (#1) was compared with the calculated phase functions at wavelengths inside the spectral interval $531.9 \text{ nm} - 532.2 \text{ nm}$ (#2). The differences were expressed as the error of fitting the curve #1 with every other curve #2 for each size. For specific sizes this error has large values inside the considered spectral interval. The fitting error is represented here as the $\sqrt[4]{\text{errorvalue}}$

Intensity profile and focusing

The Mie theory assumes for the incident field to be a monochromatic plane wave with a planar intensity profile. For the experiment to accommodate the theory, a perfectly collimated beam with a plane intensity profile is needed. The laser normally provides a collimated beam with a gaussian intensity profile. Due to the short illumination times of the detectors and the need for recording the scattering patterns of particles as small as $1 \mu m$ in diameter, a relative large power density in the laser beam is needed. Therefore the original beam with a diameter of $\approx 1 mm$ has to be further condensed to $\approx 50 - 70 \mu m$. Transforming the gaussian intensity profile in the collimated beam requires special optics⁷. An easier approach is to account for these deviations by implementing them in the computational routines [49].

The final experimental approach was to use a slowly converging beam with a gaussian intensity profile. The beam waist which defines the sampling volume is inside the flowing cell (*see* section 4.1.2). As a general approximation⁸ if the diameter of the laser beam⁹ is more than 10 times the particle's diameter, and the particle is placed in the center of the laser beam, the calculated phase functions are virtually the same, whether the formalism for a plane intensity profile or for a gaussian profile is used.

4.1.2 Optical Setup and the Flow Cell

For defining the sampling volume inside the flow cell the laser beam was focused with a lens having a focal length of $40 mm$. A cylindrical volume of roughly $50 \mu m$ in diameter and $\approx 80 \mu m$ in length, defined by the waist of the focused beam, was used as sampling volume.

Collecting the scattered light was accomplished with a microscope objective with a large numerical aperture. Recording the scattering pattern over a large angle interval is important for having a better chance to correctly identify the scatterer afterwards in the database. The microscope lens must also have a large working distance. Both numerical aperture and working distance values were chosen in close correlation with the type of flow cell used.

⁷e.g. interferometric masks carved on glass

⁸observation from the Light Scattering Analysis (LSA) software packet

⁹with the locale equiphase fronts in the laser beam close to plane wave fronts

The Flow Cell

Three different geometries for the flow cell were considered. The cell with a cylindrical geometry used with the cylinder axis perpendicular to the scattering plane is the simplest one, having the main advantage that in the scattering plane the symmetry of the problem is conserved and no corrections have to be implemented as long as the scattering system is on the cylinder axis. The two important disadvantages for this type of cell is the positioning of the sampling volume on the cylinder axis, and the poor quality of cylinder walls for low diameter cylinders¹⁰.

The second cell (*see* Fig. 4.6 and Fig. B.1) has a planar interface between the circulating fluid inside the cell and the outside medium (air), where the collecting optics are placed. The plane interface requires corrections to be applied to the recorded light pattern, both to the intensity and to angular distribution. Due to total reflections the geometry has a maximum limit for the angle interval that can be recorded through the plane window ($\approx 95^\circ$ if water is used inside the cell). When imaging the particles inside the fluid through the plane window, due to refraction, the virtual position of the object on the optical axis is changing as the angle of light collection changes. As Figure 4.6 shows, the larger the collection angle, the closer the virtual object position to the collecting system. This means that for optics with a short depth of field (even if the numerical aperture N.A. is high) the collecting angle is reduced by this effect. The magnification for both directions changes as well and therefore, the recorded image has to be corrected. Due to a higher magnification at high angles, the total available scattered intensity at these angles will be distributed over a larger area and therefore, the recorded intensity has to be corrected as well. At the same time, the angular range from where the light scattering pattern is effectively collected is smaller than maximum permitted by the N.A. of the collecting system (in Figure 4.6 θ_1 is smaller than θ_2). Another problem that has to be considered when recording over large angles through a planar window is the change in the transmission coefficient with the angle¹¹ of collection and the dependence of this transmission coefficient with the

¹⁰low diameter cylinders ($d \lesssim 3 \text{ mm}$) are to be used for allowing a close positioning of the optics relative to the scattering center as well as for minimizing the chance of multiple scattering

¹¹relative to the normal direction on the window

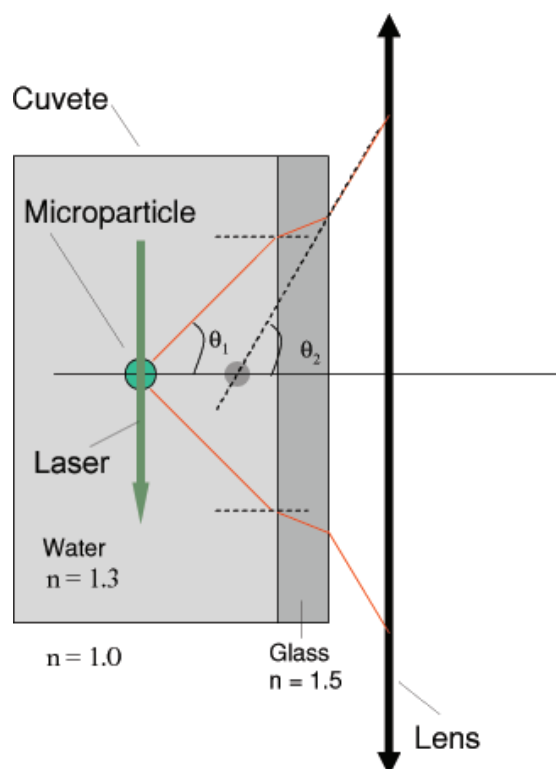


Figure 4.6: The schematic view from above for a flow cell having a planar fluid-air interface.

light polarization at the interface liquid-glass-air (Fig. 4.7). The transmission through two interfaces (fluid-glass and glass-air) have to be considered.

The third type of flow cell considered was of a more complex construction (see Fig. 4.8). The collecting optics were placed inside the flow cell. The main flow consist of distilled water. A second flow is created by injecting the sample to be investigated through a fine nozzle. The main flow drives the sample flow in the laser beam and further towards the evacuation pipe. The mechanical complexity of the cell outweighs the advantage of recording the scattered light pattern without having too many signal deformations (as is the case of the cell with the plane window).

The final setup was chosen to be based on the second type of flow cell (Fig. 4.6 and Fig. B.1) due to simplicity in construction and stability in use.

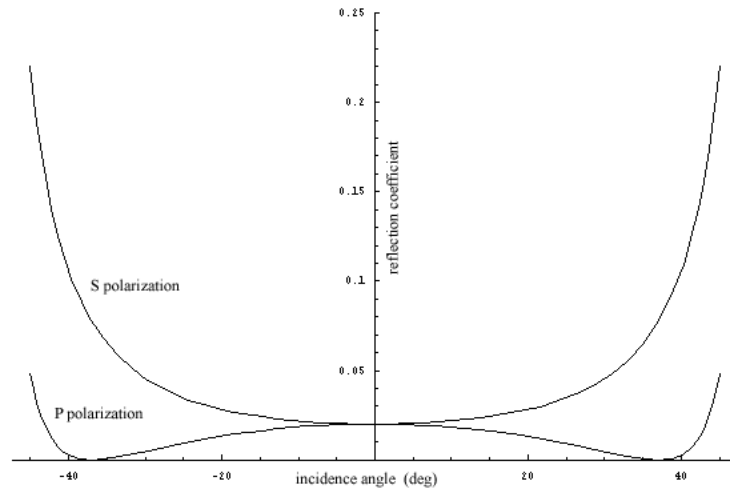


Figure 4.7: For a plane interface water-air the Fresnel reflection coefficient R is represented here. R depends on the polarization of light relative to the plane of incidence and the angle of incidence (transmission $T = \sqrt{1 - R^2}$).

Light Collecting Optics

As collecting optics a microscope objective (M.O.) of type ULWD MPlan 20 from Olympus with a numerical aperture of 0.4 was used. The maximum collecting angle for this M.O. is then $\approx 47^\circ$ when having the object plane at $\approx 8 \text{ mm}$ in front of the first lens.

Airy diffraction patterns formed by the rear aperture of the microscope objective are having no influence on the overall recorded light scattering pattern¹².

The entrance aperture of the objective was reduced by placing a diaphragm in front of the first lens as shown in Figure 4.8 and 4.1. There are two reasons for using this diaphragm. As the particles are moving (up or down) through the laser beam the images created through the M.O. are swept over the detector array. If the image is allowed to have a large size on the direction perpendicular to the scattering plane then by sweeping over the detector the fine fringe structure might get blurred by having the detector integrating over the whole height of the image. Another reason is to block the light scattered at high ϕ angles¹³ for reaching the detector in this way reducing the computational effort needed for calculating

¹²for the M.O. having the N.A. of 0.4 at $\lambda = 532 \text{ nm}$ an Airy pattern has a radius of $\approx 4 \mu\text{m}$ while the detector pixel size is $7 \mu\text{m} \times 200 \mu\text{m}$ and the main disk concentrate 84% of the total intensity.

¹³see section 3.4

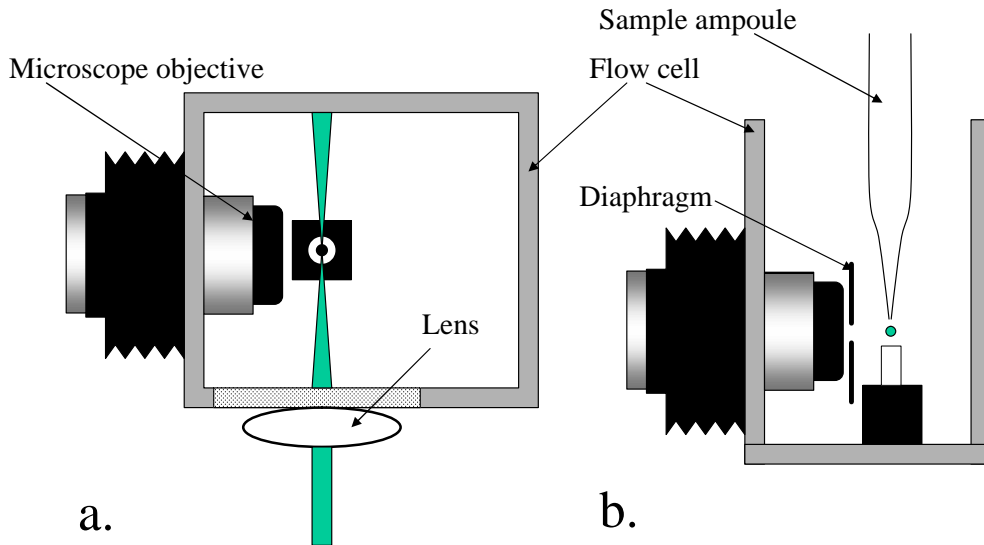


Figure 4.8: Flow cell with optics placed inside the flow chamber

the theoretical equivalent of the scattering pattern. Using a diaphragm with a 1 mm opening only the equivalent of an angle interval of $\delta\phi \approx 6^\circ$ around $\phi = 0^\circ$ is collected. For non zero angles of ϕ the calculated field has both \parallel and \perp components (sec. 3.4).

The beamsplitter placed on the optical axis of the M.O. distributes the incoming light towards two CCD arrays as Fig. 4.1 shows. The CCD no. 1 is placed in the image plane of the M.O.¹⁴ behind the beamsplitter and CCD no.2 is at a longer distance, beyond the image created after the reflection on the front side of the beamsplitter. In this way a defocused image of the particle is created on the CCD no. 2. The reflection coefficient on the front side of the beamsplitter at 45° angle of incidence and $\lambda = 532\text{ nm}$ is close to 70%, in this way most of the incoming light is sent towards CCD no. 2. The reflection on the backside of the beamsplitter has to be as small as possible¹⁵ in order to minimize the duplicate images on the detectors and avoid unwanted interference effects¹⁶.

Since the incidence angle on the front side of the beamsplitter is 45° , the Fresnel reflection coefficients for the s and p components of the incident light are different¹⁷(Fig. 4.7). Corrections have to be made when the phase functions are

¹⁴the object plane is including the laser beam

¹⁵ideally having an antireflection coating for 45° and $\lambda = 532\text{ nm}$

¹⁶the beamsplitter has a thickness of 4 mm

¹⁷for the s component at the Brewster angle $R = 0$

generated if fields of different polarizations contribute to the final curve. In our case this correction is needed only if light scattered at $\phi \neq 0$ is considered.

4.1.3 Detection System

Recording the scattered light was accomplished with two identical CCD arrays of type ILX526A from Sony, placed at different distances from the microscope objective. The linear sensor has 3000 pixels over a total length of 21 mm. The pixel size is $7 \mu m \times 200 \mu m$ and the sensitivity of $300 V/(lx \cdot s)$. The maximum clock frequency is 1 MHz¹⁸. The spectral sensitivity is maximum in the region of 450 nm and of 90% of the maximum at 532 nm. The average dark voltage is $\sim 2.5 mV$ with the saturation level at an exposure of 0.003 lx · s. The dynamic range of the detector is only 320. Recording light scattering patterns with this dynamic range, for particles with sizes from 1 μm to 5 μm using the same integration time implies having the powerful scatterer¹⁹ no brighter than approximately 50 times the brightness of the poorest scatterer²⁰. This condition holds true only if the phasefunctions are sampled for θ in the interval of 80° up to 120°. This is the reason for choosing the 90° scattering geometry.

A correction that has to be considered arises from the fact that by employing linear detectors the approximation that the transport factor from eq. 3.60-3.63 is a constant is no longer true. The use of a microscope objective also has to be considered. The difference when using an imaging system with high magnification (80x was chosen for illustration) is shown in Figure 4.9.

Both CCDs are controlled by a computer using two parallel ports in EPP mode. The electronics for controlling the CCDs are of type CCDL-30SH1-8-S from Eureka.

4.2 Measurement Procedure

A normal measurement consists in recording the light scattering patterns for a large number of particles, each particle at a time as they are passing through the sampling volume defined inside the flow cell. The system has to recognize a valid

¹⁸this is limiting the readout speed at min. $\approx 3 ms$

¹⁹usually the biggest particles

²⁰the small particles

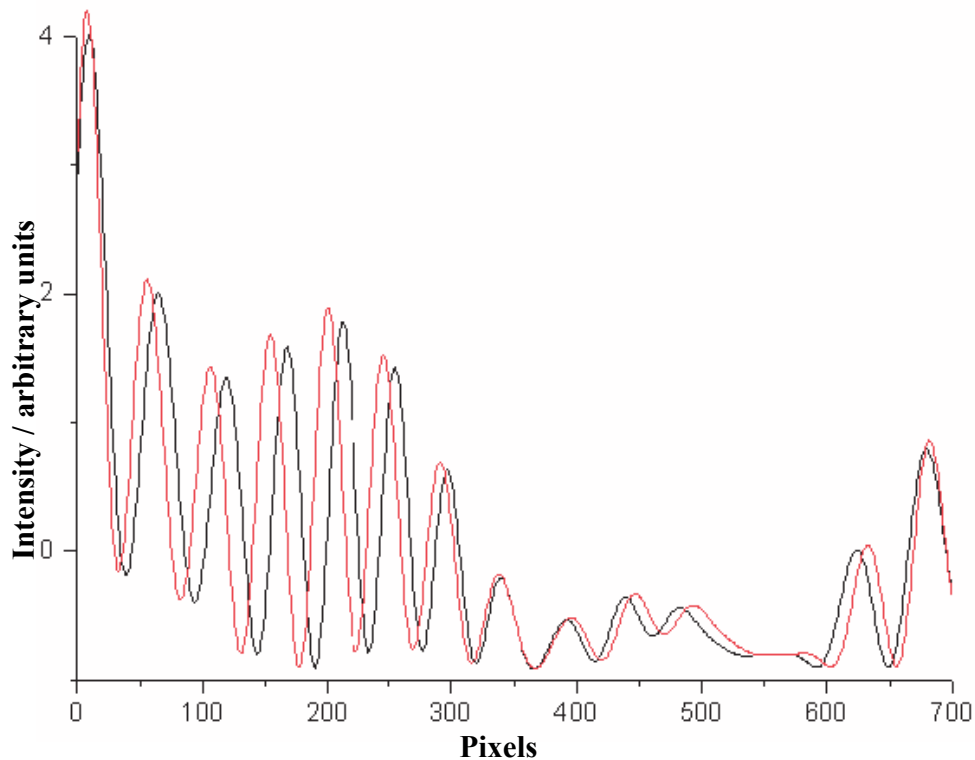


Figure 4.9: The same phase function for two different theoretical sampling procedures. The sampling with a constant step for θ (scattering angle) normally used for circular detector arrays (the red curve) and sampling with a constant step in $\tan \theta$ used when plane detectors are employed (black curve in figure). The considered imaging system was a 80x microscope objective of N.A. = 0.9. A sampling angle of 60° was used for illustration. The CCD array cells were considered having all of them the same size ($200 \times 7 \mu\text{m}$)

scattering pattern automatically and save it for further analysis. The desired speeds for the particles in the laser beam have to be in the order of 1 mm/s ²¹ and concentration of $10^6 \text{ particles/cm}^3$ so that the detection system and data acquisition procedures can function without too many discarded measurements.

4.2.1 Data Acquisition

The measurement procedure is a repetitive task which cycles until the desired number of particles are recorded. The measuring algorithm is shown in Figure

²¹an integration time of 10 ms , a M.O. with a magnification of 20x and the detector cell of $200 \mu\text{m}$ height

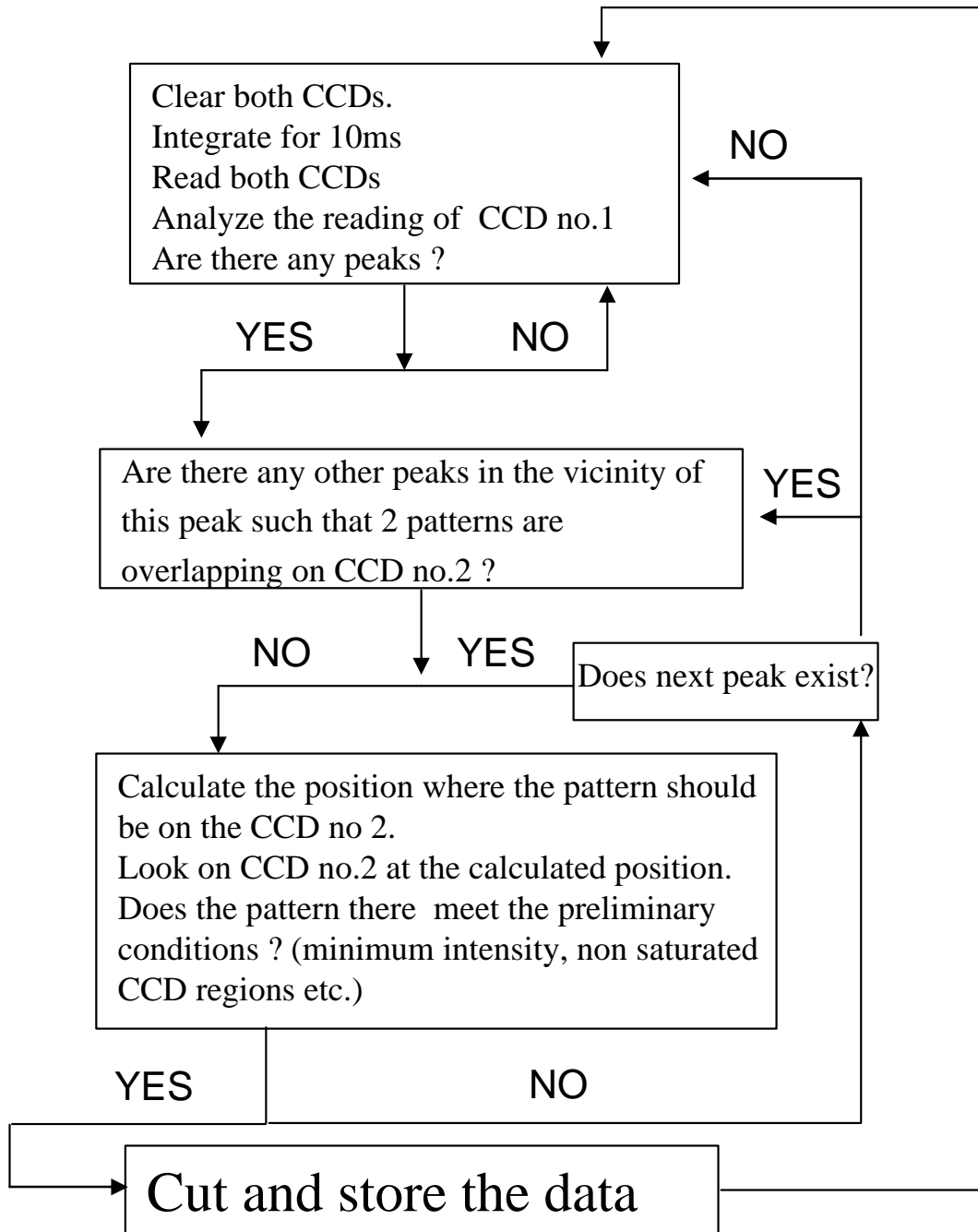


Figure 4.10: The scheme of the measurement cycle

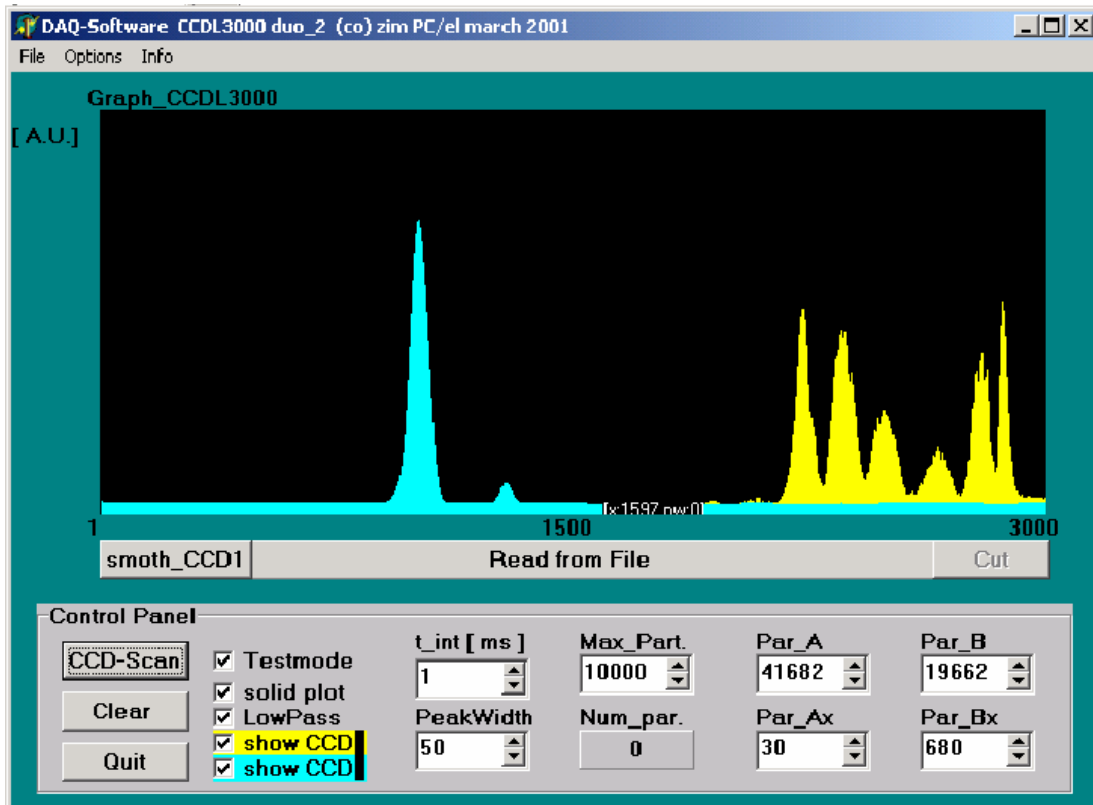


Figure 4.11: Acquisition software user interface

4.10. The procedure starts by clearing the CCD array, and then integrating for the set integration time (normally 10 *ms*). Both CCD are read after the integration time has passed and a quick analyze is made. The readout from the CCD no. 1 (see Fig. 4.1) is first roughly smoothed for eliminating of unwanted 'spikes' and then the presence of peaks is assessed. If there are particles detected, then the next step is to check whether the particles are far enough one from another such that the scattering patterns are not overlapping on the CCD camera no. 2. If the particles are spatially enough separated then the pixel positions on the CCD camera no. 2 where the scattering patterns should be located are calculated²². The readout from CCD no. 2 is checked on the calculated intervals for satisfying several criteria such as having a minimum total intensity recorded and no saturated regions. If all criteria are satisfied the patterns are cut and

²²knowing the position on CCD no. 1 and the linear transformation to a corresponding point on camera no. 2

saved. The procedure repeats till a preset number of valid²³ patterns are recorded. The whole process of acquiring the experimental scattering patterns is controlled by a PC-based instrument control software developed in Pascal (Delphi IDE). A screenshot of the software user interface showing the readings on the two detectors is illustrated in Figure 4.11.

4.2.2 Database of Scattering Patterns

At this stage the theoretical phase functions are calculated by using the stable algorithms for core-shell particles described by Kaiser and Schweiger[33] and translated and implemented in C++ by O. Sbanski[76]. The theoretical data is generated for different particle sizes with different shell thicknesses, for a fixed angle and with a fixed number of sampling points. Additionally a Fourier transformation of the theoretical spectrum is attached and a vector holding the position of the minima and maxima of the theoretical curve is also appended to the data structure. All necessary corrections for the laser line width and polarization as well as integrating over ϕ angles²⁴ are applied at this step. Generating the data for a set of particles ranging in sizes from 0.5 to 3.5 μm radius with a step of 0.01 μm and having a shell thickness of 0 up to 1 μm when measuring with a laser having a linewidth of 0.30 nm and recording over $\phi = 6^\circ$ translates into calculating approx. 9 million theoretical phase functions. The amount of theoretical phase functions stored in the database is smaller than this (only $\approx 3 \cdot 10^5$ patterns) since for each a_C and a_S pair only one pattern is saved. The effort of generating the database is made only once. The software is implemented in C++ running on linux based machines.

4.2.3 Data Evaluation

After the experimental phase functions have been recorded a set of corrections is applied to the rough data. The experimental sets are corrected for:

- relative intensity changes due to the changing transmission coefficient of the fluid-glass-air interface with scattering angle (*see* section 4.1.2)

²³satisfying the imposed criteria

²⁴as imposed by the experimental setup. ϕ values are determined by the diaphragm height, and the sampling volume positioning relative to the M.O.

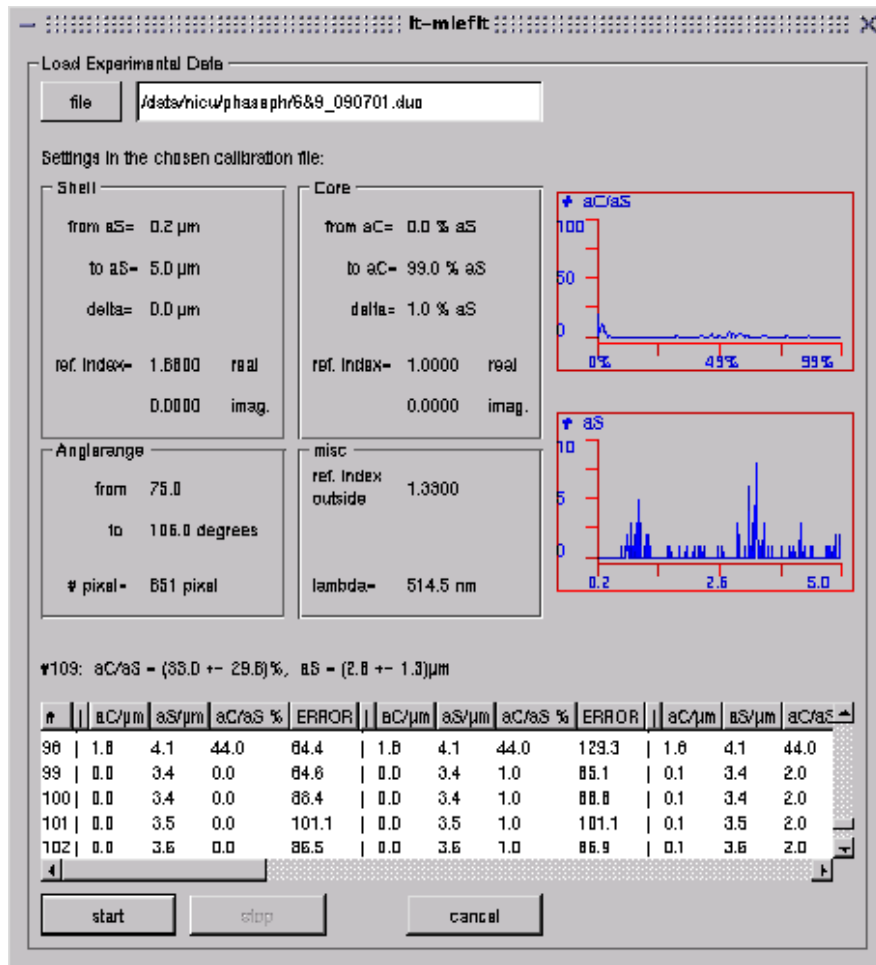


Figure 4.12: Data evaluation software user interface: Results report.

- changes in intensity due to non-uniform magnification across the angle interval (the imaged object is immersed)
- changes in angular distribution due to the non uniform magnification
- changes in angular distribution due to detector geometry (linear detectors, *see* section 4.1.3)

After the corrections were made, the dataset is analyzed by comparing each experimentally recorded scattering pattern with each theoretically generated phase function in the database. For speeding up this process, before the comparing procedure starts, for each experimental curve a quick Fourier transform is computed and attached to the experimental dataset. A vector recording the position

of the minima and maxima of the experimental curve is also created in the same manner, when generating the theoretical curves (section 4.2.2). The actual comparison of an experimental curve with a theoretically generated one is decided by first comparing the Fourier transforms and the associated vectors of the two. The comparison of the actual phase functions is made only if the distance²⁵ between these associated values is smaller than a predefined value. Since the Fourier transformation is generated only for the approx. first 20 points in the frequency domain, and having the associated vector normally with only approx. 40 independent projections, it is more convenient, in order to reduce the computational effort, to compare these at first, and only then, if necessary, the actual phase functions (which are normally generated over more than 600 points). If decided, the phase functions are compared in the same manner as the Fourier transformations were compared, namely by calculating the Euclidian distance between the two curves (experimental and theoretical considered as vectors)²⁶. After the experimental phase function has been compared with all valid candidates in the database, the closest match (given by the shortest 'distance') is considered²⁷ and the values of the inferred a_C and a_S are added to the statistic. After all experimentally recorded phase functions have been compared in this way, the final statistic is reported. Figure 4.12 shows the software user interface with the results from a measurement on standard homogeneous particles displayed. The whole process is very demanding in terms of computational effort especially if the database is large.

4.2.4 System Calibration

The parameter that has to be known before the database generation and the measurements are started is the real light collecting angle. A rough estimation for the angle interval is made from geometrical considerations. Once the system is aligned and the scattering plane defined a sample consisting of homogeneous particles with a narrow size distribution is run. The scattering patterns are recorded and fitted with theoretical phase functions generated for different sizes (inside the known narrow distribution) and different angles close to the initial

²⁵calculated as a normal Euclidian distance in a n dimensional space

²⁶each point is considered an independent projection

²⁷only if the actual error is smaller than a predefined maximum

coarse estimation. A statistic with a maximum of best fits indicating the most probable light collecting angle is obtained. Verification of the result is made by refitting the calibration set with theoretically phase functions generated only at the angle reported as most probable from the calibration procedure. The original narrow distribution should be obtained. This approach is extremely demanding in terms of computational power. A fixed setup avoids the need for such a procedure. The collecting angle and the image size on the CCD no. 2 are fixed by keeping a constant relative positioning of the sampling volume to the rest of the system. This relative positioning changes by changing the refraction index of the fluid inside the cell. Exact corrections can be made in this case.

4.3 Measurements

The current setup and the analyzing software have been tested with standard homogeneous spheres of different sizes and narrow distributions. Polymer microcapsules fabricated by Schering AG in normal production process have also been tested. The microcapsules having an empty core and a shell thickness of maximum 200 nm are normally obtained by flowing gass bubbles through an emulsion of particles with sizes in the range of few tens of nanometers. The nanosized spheres attach themselves to the bubble's wall forming the shell.

For all runs the elastic scattered light was collected between $\theta = 78^\circ$ and $\theta = 111.5^\circ$ (see Fig. 3.4 for θ notation) as it was determined by running the calibration procedure (section 4.2.4) on monodispersed spheres of diameter $2 \cdot a_C = 6.3 \mu m$. The samples were prepared with a concentration of around 10^6 particles/cm³ in water. This angle interval was recorded on 641 pixels on the CCD. no 2 (see Fig. 4.1). For having not too many scattering objects outside our generated database the water used for diluting the samples was filtered for particles larger than 1 μm .

The theoretically generated datasets hold the phase functions for all spherical particles with a core radius a_C of minimum 0.25 μm and maximum 5 μm and a shell thickness between 0 and 2 μm . The refractive index for water was considered to be 1.33.

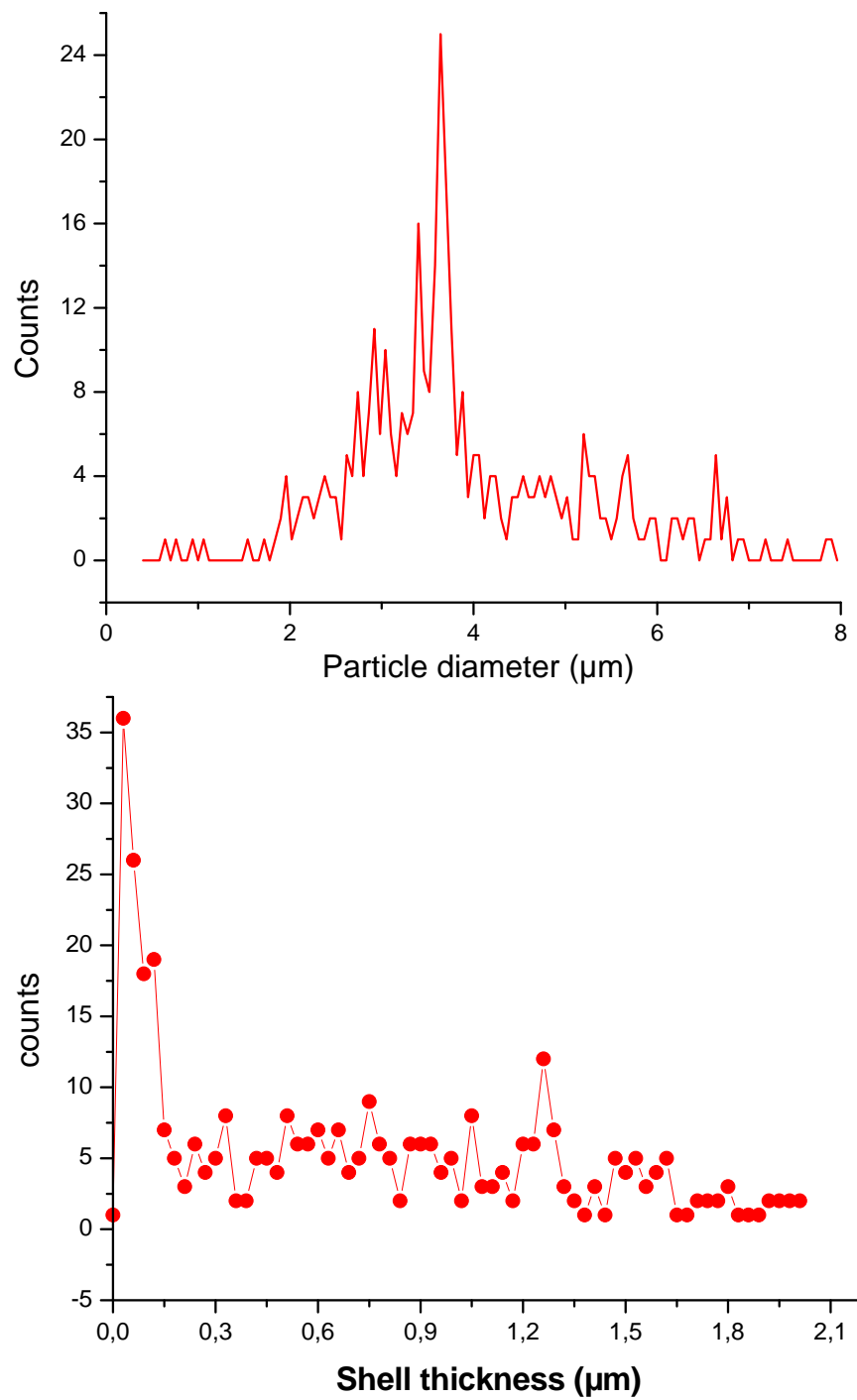


Figure 4.13: Measurement results on homogeneous standard particles of specified diameter of $4.02 \pm 0.11 \mu m$.

4.3.1 Homogeneous Spheres

The standard samples were monodispersed solutions of melamine resin particles produced by Micro-Particles GmbH under the catalog name MF-F with sizes between $1.1 \mu\text{m}$ and $6.3 \mu\text{m}$. The refractive index for these spheres is 1.68 without absorption at 532 nm (producer specifications). The scattering patterns for these particles were extremely reproducible from one particle to the next one, and also for different sample runs. Figure 4.3.1 shows the results after analyzing the scattering patterns of 1000 particles of diameter $4.02 \mu\text{m}$. Of the 1000 particles recorded by the measuring device, only approx. 370 were fitted with an error smaller than a predefined level²⁸. The 370 particles included into the final statistic show a mean diameter of around $4 \mu\text{m}$ with a clear shell thickness a_S around 0. The difference in the reported core size might be due to a slightly different refractive index for the fluid and the particles than the ones used for creating the database (1.33 for water, 1.68 for melamine resin). Two experimentally recorded curves and the closest match found in the database are shown in Figure 4.3.1

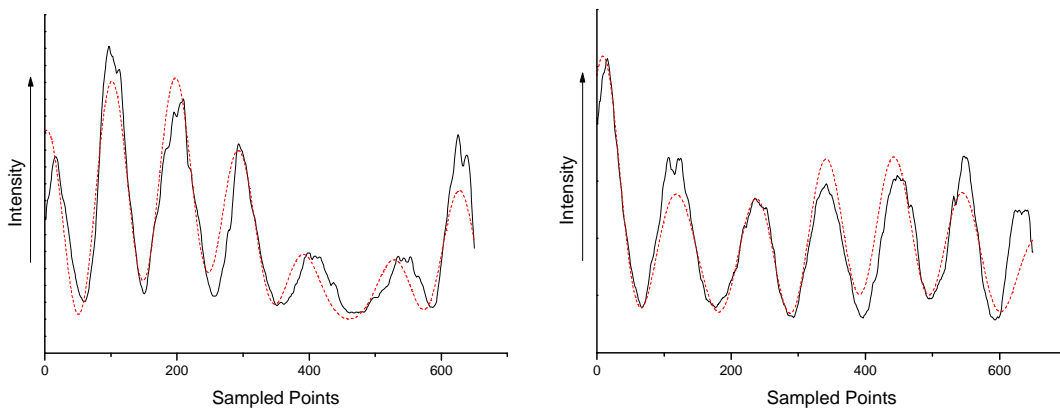


Figure 4.14: Two different experimental scattering patterns (continuous line) and the closest match found in the database for them (doted line). The scatterers are supposed to be particles having a diameter close to $4 \mu\text{m}$ and a refractive index of 1.68 placed in water

²⁸the chosen value is a relative fitting error of 350 calculated as the Euclidian distance between the two curves (considered as vectors).

4.3.2 Microcapsules

The microcapsules produced by Schering AG were also tested. The microcapsules are empty making them very fragile and having a relative refractive index to the medium (water) under unity. In this case, by interacting with the laser light two phenomena might interfere with the well running of the experiment. The photon pressure on the particle walls might damage the spherical structure and at the same time draw the particle out of the laser beam²⁹. That is why for this particular type of capsules the used laser intensities were reduced compared with the measurements on the homogeneous spheres. The damage of the structure is improbable since the manufacturer characterizes the particles as relatively stable in water columns up to 1 *m* high which translates to a uniform force on the walls of approx. 100 *nN*. However the photon pressure is not uniformly distributed over the spherical surface. Under the microscope, no damage was recognized for low laser powers as used for scattering experiments. For the force that is driving the particle out of the laser beam an estimated value of 3 *fN* at high intensities is already important since at a particle mass of roughly 10^{-13} *g*³⁰ this translates to an expelling acceleration of 30 *m/s*² out of the laser beam.

Due to capsule fragility the samples do present a lot of fragments which interfere with the measurement process. All non-spherical objects which are not represented inside the database are creating false counts. Figure 4.3.2 shows two recorded phase functions with the closest match found for them. The counts were considered valid since the fitting error was smaller than the acceptance limit. The results of a measurement on a sample containing microcapsules is shown in Figure 4.16. The false counts are either increasing the noise or are fitted by specific sizes as Figure 4.16 shows. Here the expected shell thickness was expected to be somewhere in the 150 *nm* region but the fitting procedure shows three peaks at 0, 500 *nm* and close to 1000 *nm*. These are not sustained by the physical process of particle formation. The way the software fits some of these recorded phase functions is shown in 4.3.2. Other runs having the same type of microparticles presented the same false shell thickness distribution.

In the present configuration, the system is only partially functional. The theoretical approach and the experimental implementation are not totally over-

²⁹a focussed gaussian beam

³⁰ a 5 μm particle made out of a shell 500 *nm* thick, having a density of 2 *g/cm*³

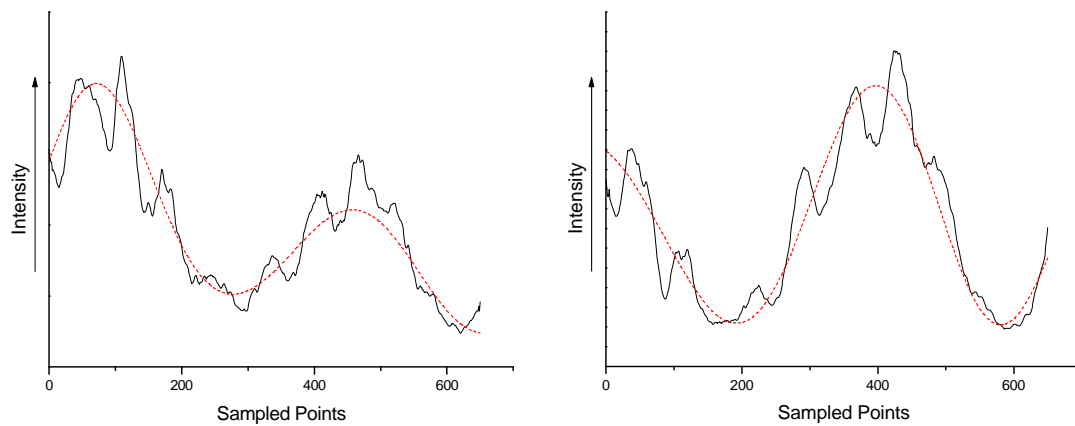


Figure 4.15: Two different experimental scattering patterns (continuous line) and the closest match found in the database for them (dotted line). The scatterers are suppose to be spherical microcapsules

lapping at this point. The database creation software have to account for the non-planarity of the incident field on the particle. In the slow focused beam used at this stage, only the absolute focus point can be considered to have a plane wave front. Furthermore, for testing purposes non-absorbing microcapsules having a core with a relative refractive index $m > 1$ are to be used.

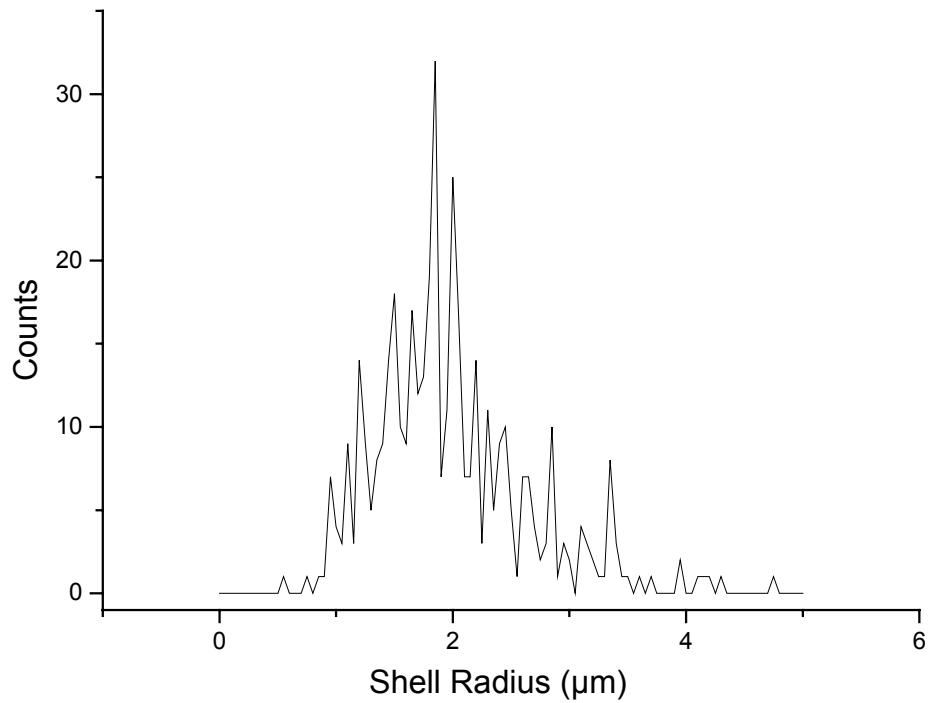
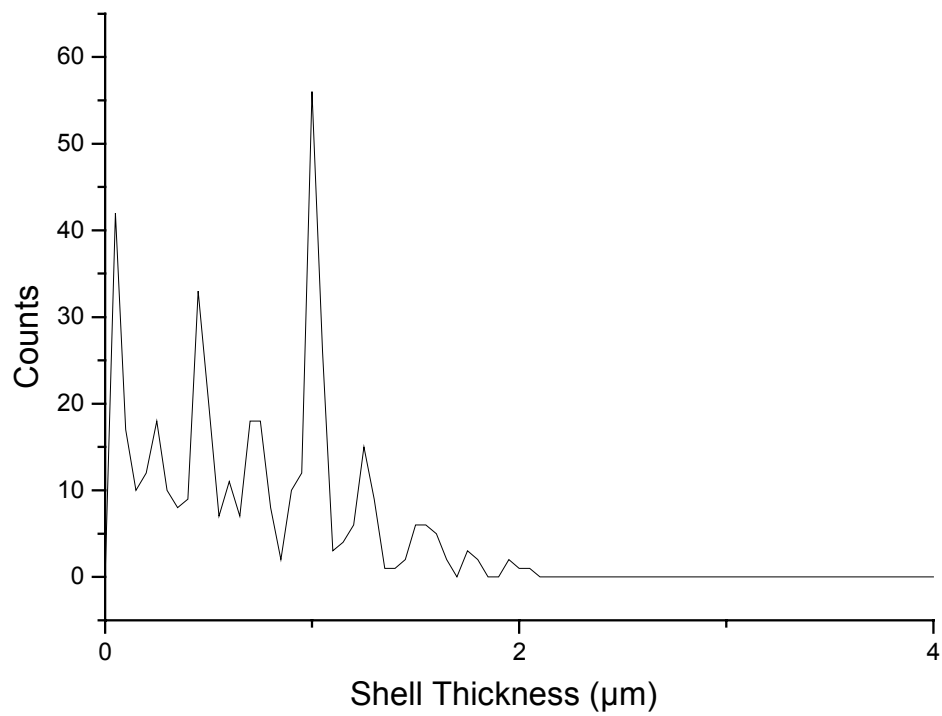


Figure 4.16: Measurements on microcapsules

Part II

MIRAS

Mineral Investigation by *in situ*

Raman Spectroscopy

Chapter 5

Introduction

Near-ground investigations of celestial bodies (planets, comets, asteroids) are expected to expand in the near future due to a steady increasing number of planned space missions. A special interest is shown towards Mars exploration. After the two Viking landings in 1976 and their successful science operation on the Martian surface, a breakthrough for the short-distance investigation of the Martian surface was the landing of the rover, Sojourner (as part of the Pathfinder mission, 1997). Recently the Mars Exploration Rover Mission with its twin rovers, Spirit and Opportunity, has already proved to be a total success. The deployment of such vehicles offers the possibility to obtain experimental data by directly sensing the surface and if needed chipping and collecting surface material for further investigations on Earth¹. The near-ground sensing can be done in various ways. However, up to now only a few techniques have been employed. Among them there are alpha proton X-ray spectroscopy (APXS)[70], X ray fluorescence spectroscopy (Viking missions 1976), thermal emission spectrometry, Mössbauer spectrometry and simple macro and microscopic imaging. Using these techniques, it was shown, for example, that the Martian surface contains large amounts of ferrous oxide and

¹upon a sample return mission to Mars is not yet decided either by NASA or ESA

sulfur (in the form of sulfate), large amounts of SiO₂ and also amounts of MgO [70]. Recently, the past presence of fluid water on Mars was confirmed by the data provided by the microscope imager together with the Mössbauer and alpha proton X-ray spectrometers².

In order to qualify for a space mission an instrument has to fulfil a set of requirements. Above all and apart from the scientific requirements, are the limitations on mass/volume and the energy needs of the instrument. A Raman spectrometer capable of *in situ* measurements for planetary missions has to be, therefore, small and robust with low needs in energy and data processing power.

Regarding the science it addresses, a micro Raman spectrometer as a stand alone device on a planetary surface (e.g. Mars) offers a wide spectrum of possibilities:

1. Chemical analysis via determination of the mineral composition.
2. Analysis of organic molecules in the soil.
3. Identification of the principal mineral phases (i.e. those making up at least 90 % of the material in soils and rocks).
4. Classification of rocks (igneous, sedimentary, and metamorphic) and definition of Martian petrogenetic processes.
5. Oxidation state of elements of Martian soil, on rock surfaces and inside rocks.
6. Content of volatiles (H₂O, SO₃, CO₂, NO₂) in minerals and glasses.
7. Determination of selected minor and trace-element contents (e.g. rare-earth elements).
8. Measurement of physical properties (e.g. size distribution).
9. Determination of reaction kinetics, i.e. oxidation processes on newly exposed surfaces, and determination of the reaction products.
10. Morphology of organic inclusions (fossils) and minerals on a μm scale.

²NASA at www.nasa.gov

11. Water and ice on Mars; identification of secondary minerals, clays, state of carbonaceous matter, hydrated crystals.

The second part of this thesis addresses the steps taken for designing and testing a small Raman spectrometer capable of *in situ* planetary measurements. The project known under the name of MIRAS was performed under the auspices of Federal Ministry of Education and Research, BMBF and German Space Center, DLR under national registration 50OW0103. MIRAS stands for "Mineral Investigation by *in situ* Raman Spectroscopy".

As supporting laboratory experiments the measurements on standard minerals and on SNC Mars meteorites are discussed on chapter 6. The SNC meteorites are thought to have come from the surface of Mars and are named after the initials of the places where the first three were found: Shergotty, India in 1865, Chassigny, France in 1815, and Nahkla, Egypt in 1911. Less than 30 SNC meteorites have been found to date. Apart from the data provided by the Viking, Pathfinder and Mars Rover Exploration missions, the SNC meteorites can also be used as a source of information on the composition of Mars materials.

A detailed description of the proposed designs for MIRAS, with the components used for building the testing version of a breadboard (BB) is covered in chapter 7. The two proposed designs, one based on an acousto-optic tunable filter (AOTF) and the other based on a dispersive hadamard transform spectrometer are compared to each other. The software developed for controlling the breadboard version of MIRAS is described in chapter 8 together with a short description of the structure of a relational database used for in house spectra management. Spectra acquired with the MIRAS breadboard version based on the AOTF are presented in chapter 9. The final chapter (no. 10) addresses a rather different possibility of using Raman spectroscopy for planetary investigations. The chapter summarizes the content of four technical notes that were established within the study contracted by the European Space Agency concerning the possibility of applying Raman spectroscopy in the field of remote imaging.

Chapter 6

Supporting Laboratory Experiments

In the last few years, a large amount of work has been done in the direction of demonstrating that Raman spectroscopy is a valuable tool for planetary research. The investigation of minerals by employing Raman spectroscopy, with application for *in situ* planetary measurements, is an ongoing project sustained by a series of scientific groups. Numerous examples are reported in the literature where this technique has been successfully applied for the characterization of minerals. Wang *et al.* [99] reported the use of Raman spectroscopy to characterize the structural and compositional characteristics of different types of pyroxene. Values of $\text{Mg}/(\text{Mg} + \text{Fe} + \text{Ca})$ and $\text{Ca}/(\text{Mg} + \text{Fe} + \text{Ca})$ of pyroxene in the (Mg, Fe, Ca) quadrilateral were reported within an accuracy of ≈ 0.1 . Pyroxenes from basalts and those from plutonic equivalent were distinguished by analyzing the distribution of their Mg' [$\text{Mg}/(\text{Mg} + \text{Fe})$] and Wo^1 values. This was done using point-counting Raman measurements on unprepared rock samples. Virtually all types of minerals have been characterized to date by using Raman spectroscopy. Raman characterization of minerals with regards to their mineral classification

¹wollastonite values $X^{\text{Ca}^{2+}}$

in classes, types, groups and species have been done and Raman features that are specific to one class, type, group or species have been identified. (Eg. Measurements on silicate garnets [41, 58], on various types of tourmaline [25], on clay minerals [59] are just a few examples). Several research groups have undertaken experiments in simulating alteration conditions in the laboratory. Raman measurements on a model silicate compound under variable pressure (from 1 bar up to 270 kbar) and variable temperature (from 108 K to 425 K) have been discussed by Liu *et al.* [48]. Measurements on olivine at different pressures and temperatures were reported by Sharma *et al.* [80]. Since minerals are exposed to significant alterations during the time scale of their formation, the experimental simulation is supposed to provide useful insights into their history of formation. To demonstrate the ability of Raman spectroscopy in determining the mineralogical character of rocks that originated on remote planets, measurements were done on meteorite samples. Solely with the use of Raman spectroscopic analysis as a stand-alone method, conclusions were drawn concerning the mineralogical formation and eventually the history of the sample. For the Zagami meteorite, by employing only Raman spectroscopy, Wang *et al.* [98], concluded that the sample was a pyroxene-phyric basalt excluding a possible formation through sedimentary and plutonic processes. An analyze of the complex shock and thermal history of the ALH84001 Mars meteorite was made by Cooney *et al.* [17] using micro-Raman and IR reflectance techniques. The application of Raman spectroscopy for an *in situ* characterization of biological samples is another very important direction of research [21, 108]. Fourier-transform, laser Raman spectroscopy in the near IR (1064 nm) has been used by Wynn-Williams *et al.* [107] to characterize a variety of key pigments and biomolecules produced by bacteria and microbes in material from extreme Antarctic cold deserts, which is analogous to martian habitats.

6.1 Mineral Spectra Database

A reference base² with Raman spectra of interest for analyzing geomaterials as well as organic materials of relevance to the subject of planetary *in situ* measurements (for now with focus on Mars) does not exist at this moment. For the existing databases the exact mineralogical, chemical and crystallographic charac-

²i.e. spectra obtained from known inorganic, organic or amorphous species.

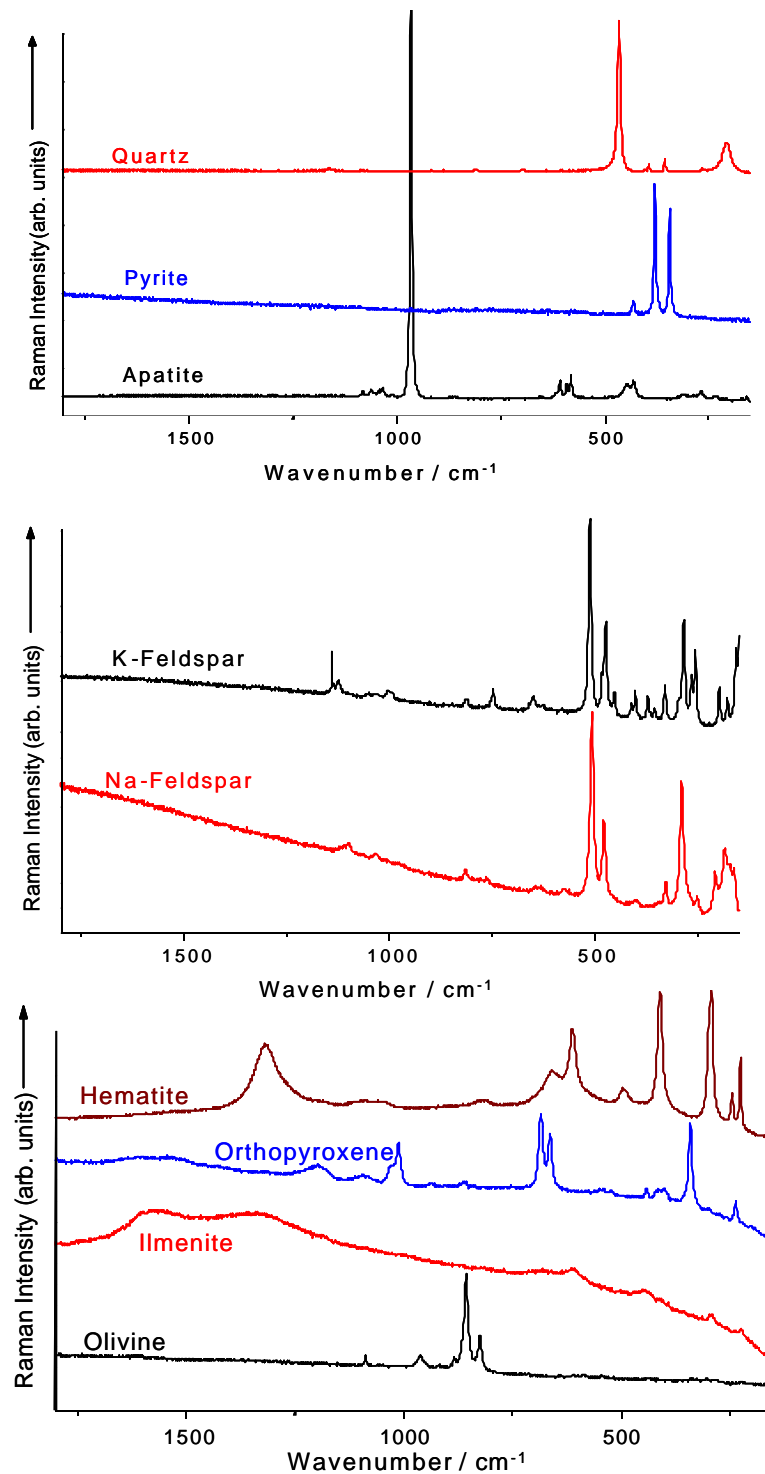


Figure 6.1: Raman spectra of different minerals. The fingerprint-like information of a vibrational spectrum allows a quick assignment. From the top to the bottom, the Raman spectra of quartz, pyrite, apatite, K and Na-feldspar, hematite, orthopyroxene, ilmenite and olivine are shown.

terization of the used reference materials is often missing, and the samples and the spectra incorporated in the database were normally selected having other objectives ahead [27, 14].

In general, Raman spectra are highly specific and they function as a fingerprint for each type of molecule. Raman spectra of a few minerals are shown in Figure 6.1. Based on this specificity, identifying the components in a sample resumes merely at comparing the measured spectra with the spectra of known components in the database. A poorly-documented database will therefore handicap any identification.

For building a database especially created for the investigation of rocks and minerals from Mars, containing spectra of all phases which are suspected to be found on Mars and in Martian rocks, and in general for building a database which is to be used by a larger user community, standards have to be adopted and agreed upon. Generating reference Raman spectra for minerals implies the existence of well defined and characterized reference materials. Up to now there are no standardized reference materials agreed upon and no mineral Raman database of large acceptance.

The building of a mineral database for use in conjunction with the experiments for the MIRAS project is therefore essential. The main goal is to have an indexed catalog with the main vibrational modes for each mineral of interest. Minerals from the Museum of Mineralogy at the University of Würzburg as well as from the Mineralogische Staatssammlung München were used for building a part of this index.

As general measuring procedures for acquiring the Raman spectra in the database neither the orientation of the light polarization plane relative to the crystal axes³ nor the setup characteristics or the spectrometer parameters were considered, measurement on different points of a sample and different similar samples were performed instead and compared with general data available in literature. For each mineral a 'synthetic' Raman spectrum was afterwards composed taking into consideration all available data. The actual implementation of the database is discussed in section 8.3. (*see* also Figure 8.5, C.6, C.7, C.8)

³In order to partially exclude the polarizations effects, incident light can be prepared to have a circular polarization. Even then, the intensity of the Raman modes can be sensitive to crystal orientation.

6.2 Measurements on Meteorite Samples

SNC meteorites are the only genuine martian material available. Up to now less than thirty SNC meteorites have been found. Thus SNC meteorites are extremely rare, very valuable and highly priced if at all available on the market. That means that destructive methods, e.g. thin cutting for optical microscopy, electron microprobe analysis, x-ray diffraction, can only be conducted on a very limited number of samples. From these samples, only a tiny part - due to their rarity and value - is available for destructive investigation methods. Most parts of these meteorites are in private and/or public collections and are not available for these types of investigation methods. Micro Raman spectroscopy offers a nondestructive⁴ possibility of investigating these valuable SNC meteorite samples.

The mineralogical knowledge of SNC meteorites differs very much from sample to sample. Some have been the subject of an immense number of investigations (for instance Zagami), whereas others, especially the newly found SNC meteorites from the African desert, are only known from short abstracts and a small number of overview investigations which are routinely done after the discovery of the respective meteorite. Whereas the main components of the SNC meteorites are mostly known, the knowledge of the accessory minerals (oxides, sulfides, carbon-bearing phases, hydrous phases) is mediocre even for the "classic" SNC meteorites. Until now most of the newly found SNC meteorites have not been investigated for these phases. Thus, for instance, information on the cooling rate, the evolution of the magmatic Martian rocks or the weathering and hydrothermal alteration of these rocks on Mars are lacking. Especially the finding of pyrrhotite as an important contributor to the magnetic signature may have major implications for the interpretation of the Martian magnetic anomalies and for the magnetic signature of the shocked pyrrhotite-containing SNC meteorites[92].

All of the measurements on the SNC meteorites were performed with the same spectrometer used for measuring the standard minerals, namely a commercial micro-Raman setup (Labram from Dilor). A He:Ne laser operating at 633 *nm* with a power of 1 *mW* at the sample and an Argon-ion laser at 514 *nm* were used. Raman spectroscopic imaging of Mars meteorite material and point measurements of these samples were used to identify the minerals. The samples,

⁴except some rare cases of oxidation changes of iron components by a strong laser beam

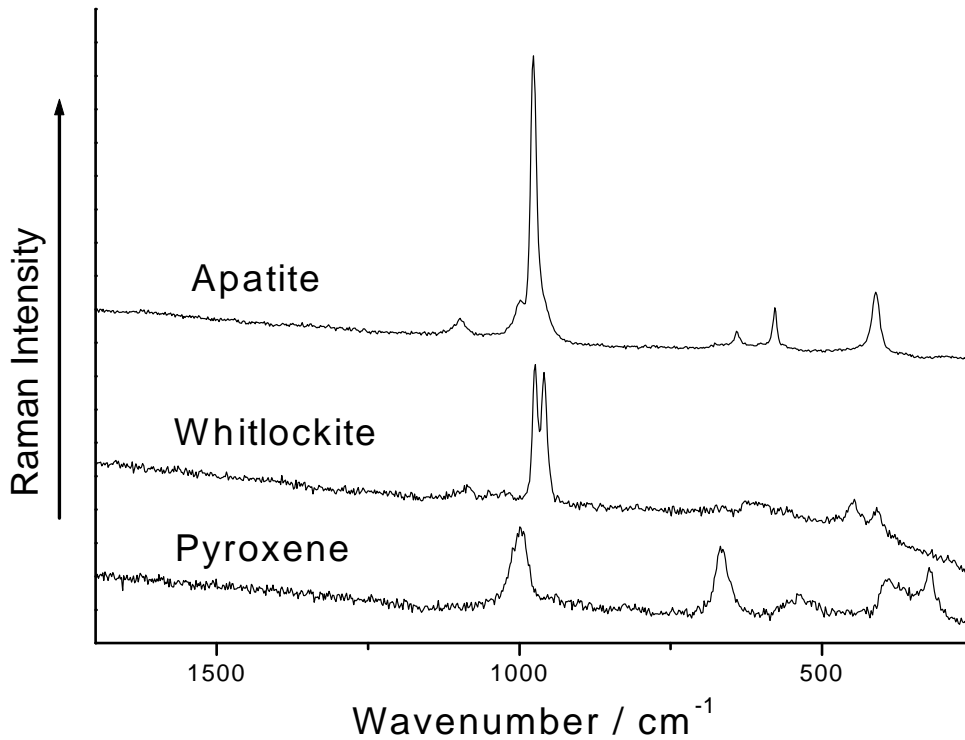


Figure 6.2: Raman spectra recorded from a Zagami slab.

Sayh al Uhaymir 060 (SaU 060, MSM⁵ 28321), Dar al Gani 735 (DAG 735, MSM 27776), Northwest Africa 856 (NWA 856, MSM 27845) and Northwest Africa 1068 (NWA 1068, MSM 28322), were provided and are under the custody of the Mineralogical State Collection in Munich. Among the interesting findings on this meteorites, pyrite as a hitherto undescribed phase in the picritic (olivine-phyric) shergottite NWA 1068 as well as reduced carbon (e.g. graphite) and anatase in the shergottite Say al Uhaymir 060 are reported for this class of meteorites [30]. Different mineral and organic components can be easily identified by analyzing the Raman spectra taken from micrometer sized spots on the sample. Exciting only a small spatial region on the sample ensures the excitation of a relatively small number of different types of molecules and therefore the spectrum does not become extremely complex by overlapping characteristic Raman features from different molecules. The Raman spectra are highly specific, the extreme differences between spectra allowing a quick assignment and identification. Even for

⁵MSM numbers are the identifiers used by the Mineralogische Staatssammlung München from where the samples were borrowed

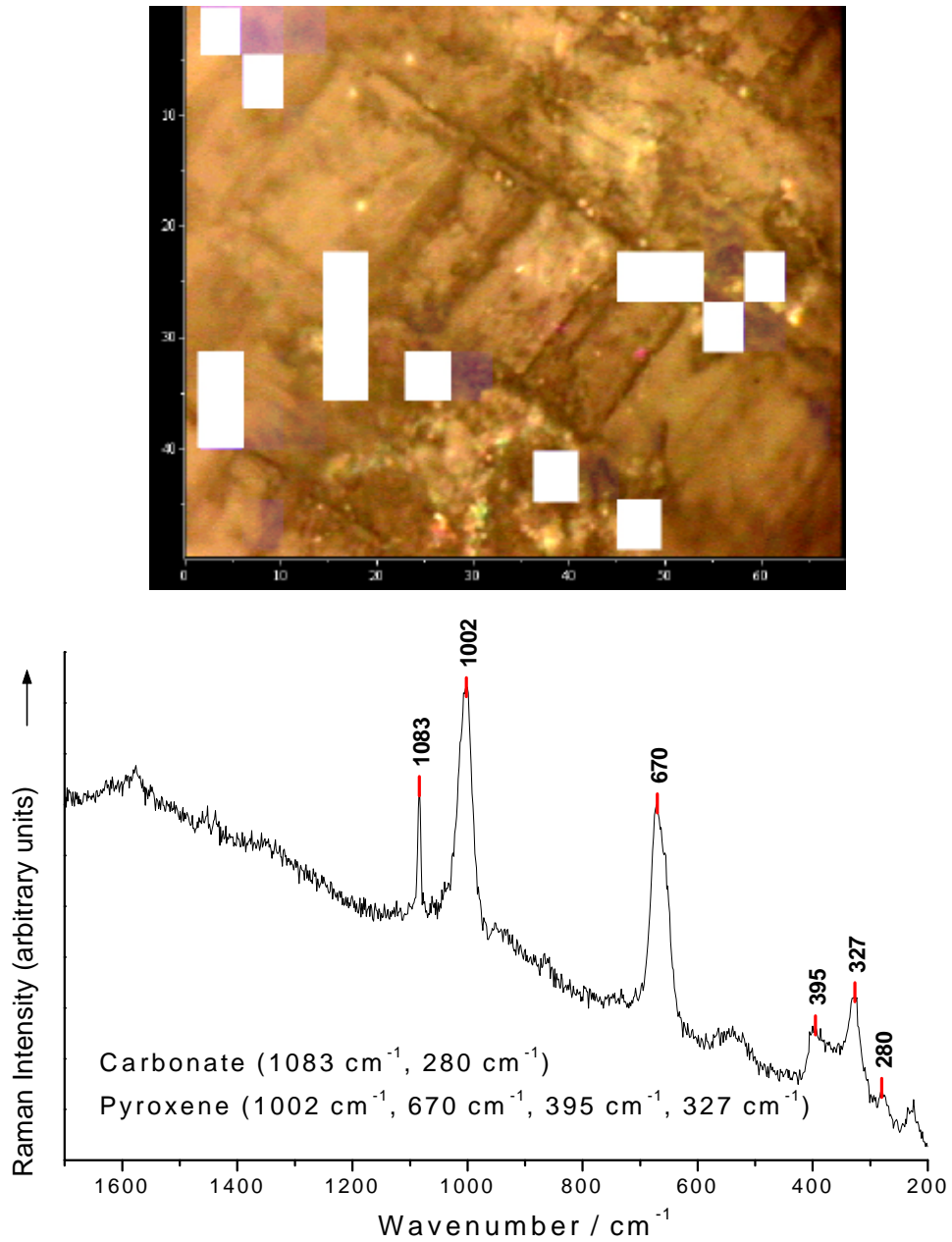


Figure 6.3: Sample of the shergottite SaU 060 with single grains of Calcite intergrown with pyroxene and Raman spectrum recorded on a pyroxene grain (the white spots localize the calcite grains as measured with the Raman scan).

the minerals from the same class as for example K-feldspar and Na-feldspar there are important distinct features (e.g. in the region from 300 to 500 cm^{-1} Fig. 6.1). The spectra measured on the Zagami meteorite can be directly attributed to whitlockite, apatite and pyroxene by simple comparison (Fig. 6.2). Figure 6.3 shows a simple example of a spectral features overlap. In this case the characteristic Raman features of pyroxene and calcite are easily recognized. Next to

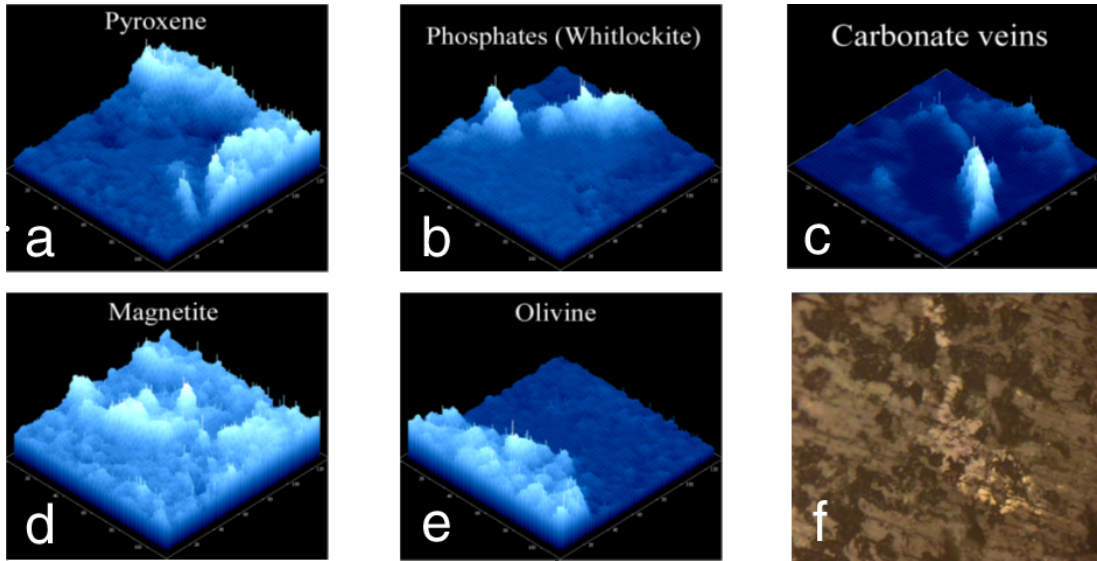


Figure 6.4: Surface scans on DAG735 Mars Meteorite: a) pyroxene distribution b) whitlockite distribution. c) carbonate distribution. c) magnetite distribution. e) olivine distribution. f) white light image.

an easy identification of organic and inorganic compounds, Raman spectroscopy, when used in conjunction with an imaging technique, might provide new insights into the origin and formation of the investigated sample by resolving the fine spatial distribution of different components. The scans performed on a few rough cut surfaces of Mars meteorites are meant to emphasize some of the advantages Raman spectroscopy has to offer when combined with an imaging technique [88].

In most of the meteorites investigated up to now, carbon is present either as graphite or as carbonates, rarely as diamonds [74, 75], while in SNC meteorites carbon has been only found in form of carbonates. Graphite or diamond have not been observed. Among carbon-bearing phases, reduced carbon is of special interest because it might be the only remainder of ancient life on Mars. The harsh environment on Mars (i.e. dry, low temperature, large temperature cycles,

high level of UV light, low oxygen, intense physical weathering) may destroy most of the carbonaceous phases. Thus it would be very important to identify for instance graphite in Martian rocks. Raman spectroscopy is well recognized as a promising technique for detecting carbon-bearing and other light-element-containing phases [96]. During our Micro-Raman measurements we found, to the best of our knowledge for the first time, graphite in the SNC shergottite Say al Uhaymir 060 (Fig. 6.5). The origin of these carbon compounds always comes

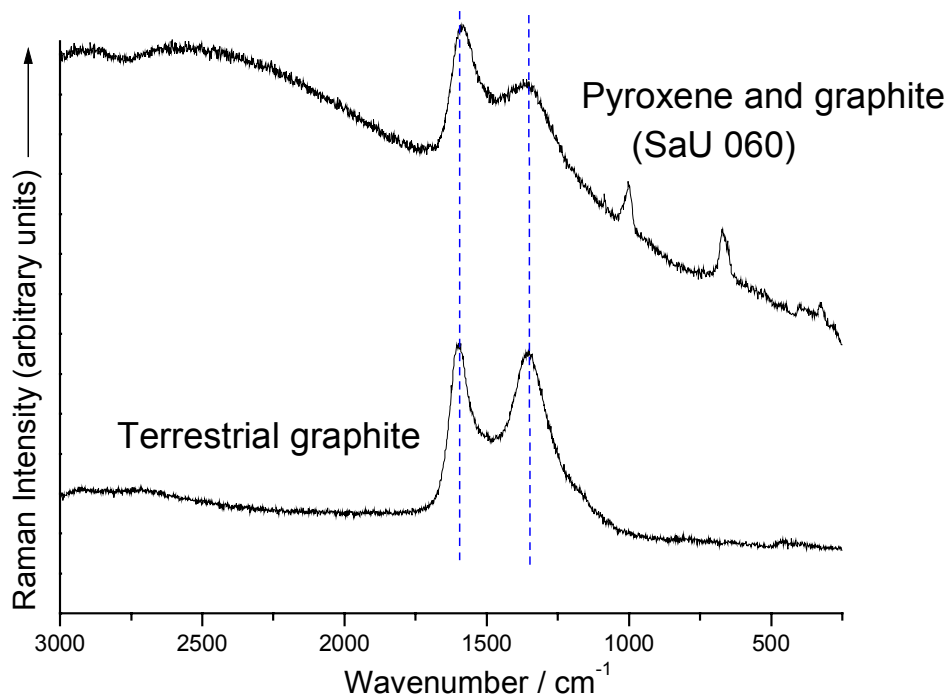


Figure 6.5: Raman spectrum of carbon containing material in SaU 060 meteorite compared with a Raman spectrum measured on terrestrial graphite.

under discussion since on Earth the carbon based minerals have mostly a biogenic origin. Since Raman spectroscopy is basically a measurement of the molecules vibrations, to differentiate among the biotic or abiotic origin of such a mineral using this technique is extremely difficult if not impossible. The crystallographic structure is virtually the same for the mineral whether it is the result of a biotic or an abiotic process. Other information has to be used in order to be able to make assessments on the biogenicity of the mineral. The spatial distribution of different components can provide clues in this direction. Calcite in meteorites is often regarded as a product of terrestrial weathering. In SNC meteorites it is

sometimes supposed to be of martian origin. Textural features can help to solve part of this problem. The calcite distribution on the investigated surface ($100 \times 100 \mu\text{m}$) of DAG 735 meteorite is an example (Fig. 6.4). Even if this meteorite was reported as less weathered and without carbonate contamination, the vein shape of the calcite distribution strongly suggests the origin of this calcite as the weathering processes on earth at the landing site through water infiltrations from the soil. The same type of veins are observed on the NWA 1068 slice. Actually, on this surface, the calcite veins are clearly recognized even by looking at the simple image of the surface (Fig. 6.6 a). The calcite distribution (Fig. 6.6 b.) obtained by Raman mapping is matching the visible veins. The apatite and olivine distributions (Fig. 6.6 c- d) are shown also. For the SaU 060 surface (Fig.

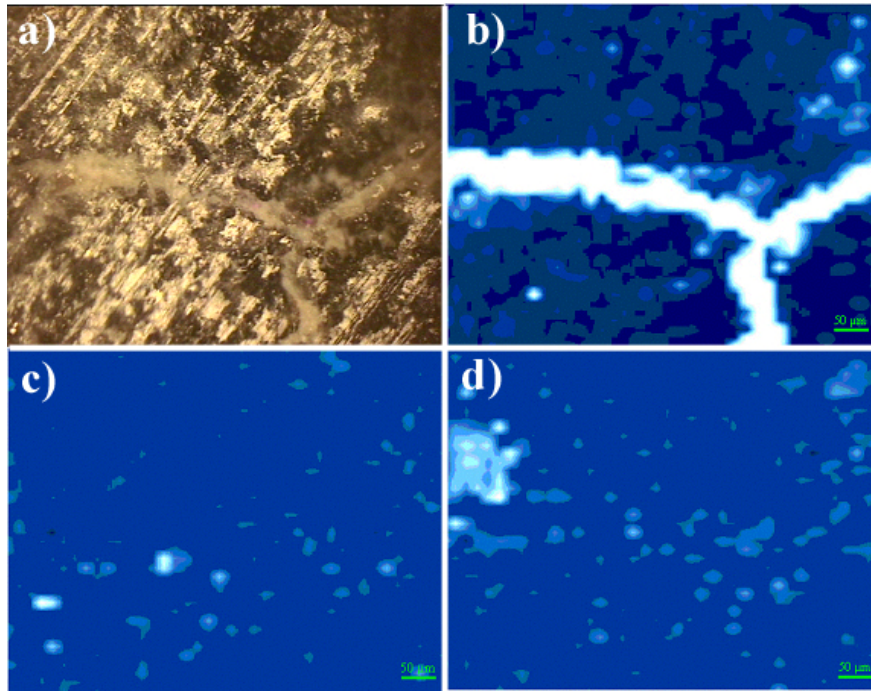


Figure 6.6: Surface scans on NWA1086 Mars Meteorite: a) normal image. b) calcite distribution. c) apatite distribution. d) olivine distribution.

6.3) calcite is present in small quantity scattered over the surface. In this case the spatial distribution suggests either a contamination in laboratory by handling the sample or by surface weathering of the meteorite in the Earth's atmosphere. Since SaU 060 is not an observed fall but a find with a considerable time on earth, there is a great possibility that the investigated calcite has grown on earth due

to a common weathering process. The information from the immediate vicinity of calcite grains might confirm or discard other suppositions. The coexisting minerals are pyroxene and graphite and these points to a magmatic origin of the calcite if it is assumed that the calcite was formed not on earth but at the same time with the rock on Mars. The main advantage of Raman spectroscopy when

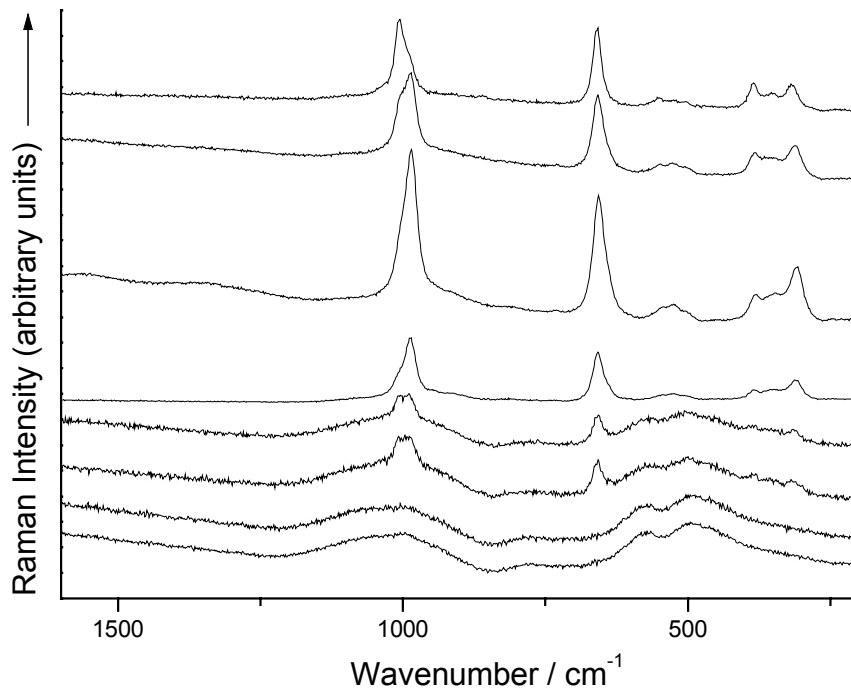


Figure 6.7: A line scan on NWA 856 meteorite. The change of crystallinity suggest the existence of a shock event in the history of the meteorite.

combined with an imaging technique is the amount of information that such an investigation provides in terms of mineral characterization of the sample. At the same time, the amount of information produced is a disadvantage in terms of data transfer limits for an automated investigation on a remote planet. There are generally two ways of performing Raman imaging. One method involves scanning point by point on the whole surface of interest and the other is to use a spectrometer with image preserving capabilities. The spectrometers based on an acousto-optical tunable filter have this capability. The present breadboard of the MIRAS spectrometer is built around such a filter. For now the imaging capabilities are not exploited since we are using a point detector - a photon

counter avalanche photo-diode (APD). Still, the basic capabilities were tested using a slightly different setup as described in Section 9.

Another problem that Raman spectroscopy can address is the crystallinity of the sample, with direct significance for inferring the major thermic events in the history of the sample. Usually a crystalline sample produces a Raman spectrum characterized by sharp bands. For the formation of crystalline minerals there are specific conditions (e.g. the variation of temperature and pressure in time) which have to be met. The rapid solidification of melted rocks is normally accompanied by the formation of some amorphous phases which are producing Raman spectra with large bands. To illustrate this fact we made on NWA 856 a linear scan on a pyroxene crystal from its inner part towards its margins. The spectra from such a linear scan of roughly $30 \mu\text{m}$ are shown in Figure 6.7. The change of crystallinity from the fairly crystalline pyroxene (upper spectrum) to the glass like phase of maskelinite (lower spectrum) suggests a shock event which produced the meteorite. The pyroxene grains seems to be surrounded by melted plagioclase.

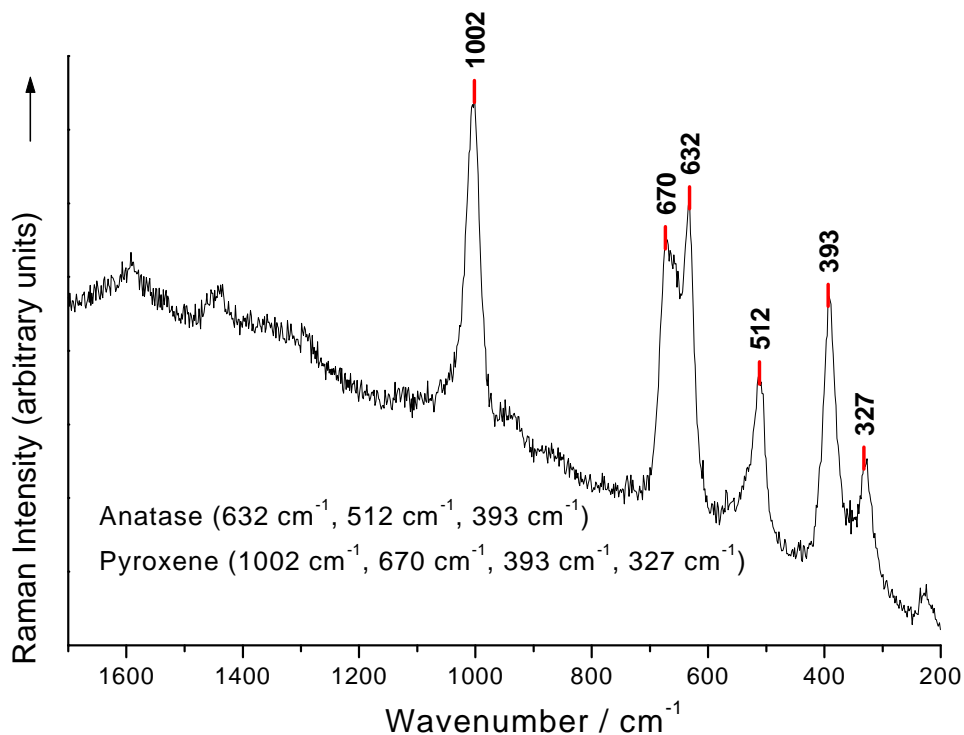


Figure 6.8: Raman spectra of anatase and pyroxene in SaU 060.

Another advantage offered by Raman technique, is the fact that it provides

direct information on molecular or crystal structure and therefore is best suited to distinguish polytypes (minerals with the same chemical composition but different crystal structure), e.g. rutile and anatase or pyrite and marcasite. During our preliminary study we found for the first time anatase in the SNC shergottite SaU 060 (Fig. 6.8). The reason that anatase had not been found before in SNC meteorites is surely due to the fact that electron microprobe analysis cannot distinguish between rutile and anatase whereas by means of normal x-ray diffraction one is not able to investigate such small grains in the matrix. However micro-Raman spectroscopy can easily offer the information needed without destroying the sample.

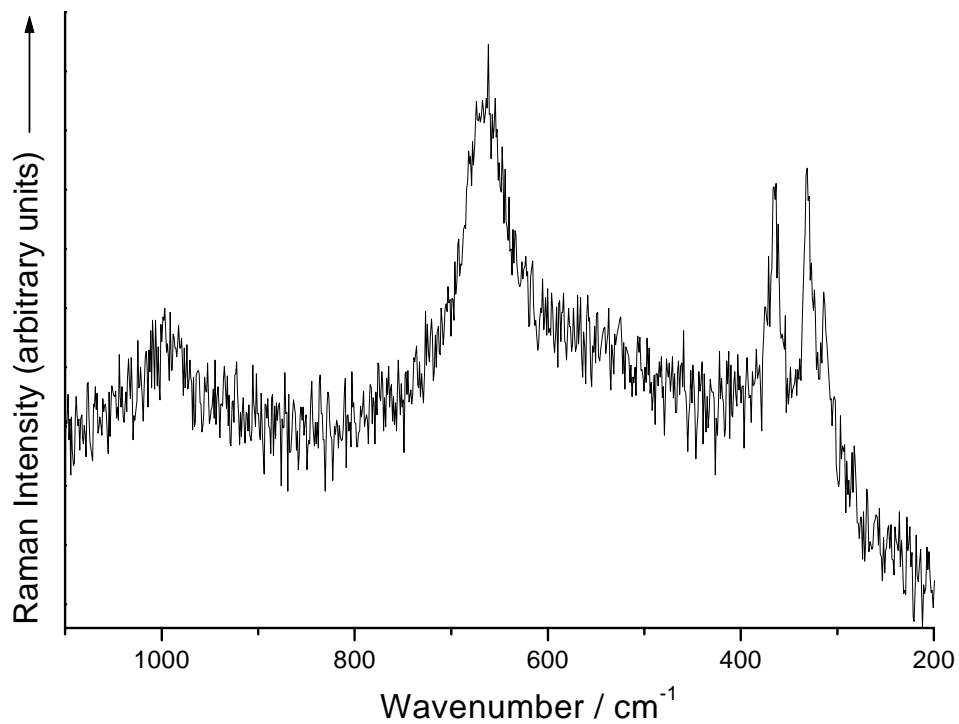


Figure 6.9: Overlapped Raman spectra of pyrite and magnetite from NWA 1068 olivin-phyric shergottite.

The existence of pyrite may be a hint to prebiotic synthesis of biomolecules on Mars [100, 101]. Therefore the evidence of pyrite in SNC meteorites is an important argument for the discussions about possible life on Mars. Whereas the iron sulfide pyrrhotite can often be found especially in basaltic shergottites, pyrite is extremely rare. During our investigations of SNC meteorites by means

of micro Raman spectroscopy we found pyrite as a hitherto undescribed phase in the picritic (olivine-phyrical) shergottite NWA 1068 (Fig. 6.9).

Chapter 7

MIRAS - Instrument Design and Construction

The envisaged planetary missions require space-born instruments, which are highly miniaturized with respect to volume and mass and which have a low need in power. The technical developments in the last years have introduced a new generation of small Raman systems suitable for robotic mineral characterization on planetary surfaces. Raman systems have been developed in this direction. A flight Raman spectrometer for the Athena rover scientific instrument was proposed by Haskin and Wang [95]. A prototype of a miniature laser-Raman spectrometer with a 852 *nm* laser, CCD detector system and confocal microscope was developed by Dickensheets *et al.* [20]. A Remote pulsed laser Raman spectroscopy system for mineral analysis on planetary surfaces is presented by Sharma *et al.* [79]. UV resonance Raman used for an easy identification of endolithic organisms and their background mineral matrix is discussed as a possible technique for a future remote planetary mission by Storrie-Lombardi *et al.* [85]. Proposals of a Raman system for future planetary missions like the ExoMars Mission 2009 have been submitted [61, 87].

7.1 Instrument Requirements

The instrument design, performance and operation have to fulfil certain requirements that must be met in order not to compromise the scientific return of the mission. Part of the requirements are imposed by the scientific goals set for the mission, and the other part are demanded by the technical details and particularities of the proposed mission.

The requirements for a possible planetary mission to Mars as they were set for MIRAS are presented in the following two tables (table 7.1 and 7.2)¹.

The scientific questions expected to be answered by a Raman spectrometer on such a mission as well as the main requirements imposed by these scientific goals are summarized in table 7.1. The most important characteristics are the spectral resolution and the laser wavelength. A laser in the NIR region was considered for minimizing the chance of fluorescent behavior of the investigated sample under the laser light. Detecting the inelastically scattered light up to 3800 cm^{-1} relative to the laser line with a detector based on silicon² requires a laser wavelength shorter than 750 nm . For testing purposes a laser at 785 nm was used due to the availability of components tailored for this wavelength (e.g. laser diodes, interference and notch filters, anti-reflex coatings for optics). The proposed resolution of the spectrometer was chosen to be equal to that of a medium-class laboratory Raman spectrometer ($\approx 5\text{ cm}^{-1}$) for the region where characteristic vibrations for most of the minerals are, namely from 150 cm^{-1} ³ to 1900 cm^{-1} , and for the region of interest for detecting hydrated minerals and organic structures based on carbon (2400 cm^{-1} to 3800 cm^{-1}).

The mission itself imposes requirements on the instrument, requirements which normally prevail over the scientific ones. A summarized view of the mission set requirements is presented in table 7.2. Apart from an adequate radiation shielding and a robust structure capable of sustaining the strong vibrations and tensions caused by travel and large temperature & pressure variations, the most important requirements are concerned with the instrument mass and volume, energy consumption and data amount produced for achieving the scientific goals. For these requirements an upper limit of 1.8 kg for the mass, at a volume of

¹extracted from the MIRAS proposal to DLR

²cutoff wavelength is around 1050 nm

³this lower limit is imposed by the elastic light filtering solution adopted (*see* Section 7.3.2)

⁴See abbreviations at page no. 161

MIRAS Scientific Requirements		
No.	Requirements	Value
Sci. 01	Surface investigation of extraterrestrial rock and soil with regard to mineral composition and crystal lattice structure by in-situ-Raman Spectroscopy	-
Sci. 02	Detection and characterization of anorganic and organic compositions in extraterrestrial soil and rocks	-
Sci. 03	Search of extant life by means of Raman Spectroscopy	-
Sci. 04	Detection of water in planetary soil and rock	-
Sci. 05	Investigation of raw material without pretreatment of the surface	-
Sci. 06	Investigation to be performed during night as well as normal planetary daylight	-
Sci. 07	Preferred wavelength of illuminating laser	785 nm
Sci. 08	Spatial resolution	10 μm
Sci. 09	Minimum total illumination energy at sample position	5 mW
Sci. 10	Minimum number of spectra to be a acquired	120
Sci. 11	Measurement of stokes Raman signal with a spectral bandwidth in terms of wavenumber	200 cm^{-1} – 3800 cm^{-1}
Sci. 12	Spectral resolution in the wavenumber range 200 cm^{-1} – 1900 cm^{-1} , 2400 cm^{-1} – 3800 cm^{-1}	5 cm^{-1}
Sci. 13	Spectral resolution in the wavenumber range 1900 cm^{-1} – 2400 cm^{-1}	10 cm^{-1}
Sci. 14	Internal standard for internal wavenumber calibration required	-

Table 7.1: MIRAS Scientific Requirements

approx. 3.5 dm^3 was set. The power need for normal functioning should be no more than 6 W and the data link budget for a minimum mission lifetime was set at around 2 Mb.

7.2 Proposed Designs

The basic design is thought to be a modular construction. The main components that are brought together to build the device are the laser unit, the Raman head, the Rayleigh filtering box, and the spectral sensor (spectrometer with a matching

MIRAS Mission Requirements		
No.	Requirements	Value
Mis. 01	Total dose radiation (4mm Al shielding assumed)	20 krad
Mis. 02	Adequate measure for SEE ⁴ treatment is required for memories; SEE rate has to be taken into account	10^{-10} SEU ⁴ /bit/day
Mis. 03	Adequate measure for SEE treatment is required for linear parts; SEE rate has to be taken into account	1000 SEU/day
Mis. 04	To minimize proton induced SEU, second layer shielding design is recommended (combination of high and low Z materials)	-
Mis. 05	Materials recommended for structure/housings are materials with high carbon content (C/SiC, CFRP, B ₄ C)	-
Mis. 06	Electronics must be SEU safe	-
Mis. 07	Temperature (operational)	-55°C to +60°C
Mis. 08	Temperature (storage)	-55°C to +60°C
Mis. 09	Nominal power consumption of instrument	6 W
Mis. 10	Peak power consumption of instrument	10 W
Mis. 11	Total mass of instrument	1.8 Kg
Mis. 12	Instrument volume; sensor head and main part of instrument may be separated and connected by optical fibres	3.50 dm ³
Mis. 13	Maximum data uplink rate (command)	tbd
Mis. 14	Maximum data downlink rate (control& science)	tbd
Mis. 15	Compatibility with vacuum environment	10^{-12} hPa
Mis. 16	Compatibility with vibration environment	tbd
Mis. 17	Compatibility with shock environment	250g/38ms
Mis. 18	Compatibility with primary power supply	28V/10W
Mis. 19	Minimum operation time per day (not interrupted)	1 hour
Mis. 20	Minimum mission lifetime (on planetary surface)	7 days
Mis. 21	Maximum data volume within minimum mission lifetime	2 Mb

Table 7.2: MIRAS Mission Requirements

detector). There is no fixed configuration for the use of such a spectrometer on a planetary mission. Different configurations are directly linked to the different scenarios of using such a Raman device:

- The whole instrument can be mounted on the planetary lander having a common system for sample retrieval and sample handling. Sample can be shared with other instruments.
- Sensor head is integrated on lander robotic arm with no electronics and movable parts in the sensor head. The main box is mounted on the lander platform including light source and spectrometer. The sensor head and the light source, as well as spectrometer are linked via optical fiber.
- Sensor head integrated into a MOLE⁵ [69]. No electronics and movable parts are placed into the sensor head, the main box being mounted on the lander platform. Optical fiber connections make the connections with the sensor head.
- The whole device integrated on the rover (robotic arm as option). No electronics and movable parts in the sensor head.

Depending on the technicalities of the mission, the Raman device has to be easily adapted. The MIRAS approach has different designed Raman sensor heads (the focusing and collecting optics) linked with the spectral sensor and the laser unit either directly or through optical fibers. For testing purposes two configurations were chosen having different spectral sensors. One configuration is based on a dispersive Hadamard transform spectrometer [73], and the other is based on a filter-like spectral sensor built around an acousto-optic tunable filter (AOTF).

7.2.1 Hadamard Spectrometer Based Design

A novel and promising approach is the Hadamard-Transform-Spectrometer. Its high efficiency is achieved by combining a specially adapted grating with a multi-slot array, operating as the subsystem aperture. The combination of the multi-slot array, the adapted grating and the CCD generates so-called "sub-pixels" which enhance the spectrally resolution considerably.

⁵a self-penetrating subsurface sampling device

In this concept a spectrometer with a so-called double array architecture [72], working as Hadamard transform spectrometer [71] has been investigated. The component has a specially adapted grating as well as an additional multi-slit-array as entrance aperture. This architecture provides a significantly higher throughput along with improved sensibility and spectral resolution compared to commercial spectral sensors. The detector consists of a CCD matrix with a length of 25,6 mm. The resolution of 5 cm^{-1} is reached for the whole spectral range (from 785 nm to 1100 nm) with a total length of about 55 mm for the Hadamard spectrometer component [73]. For the detection of very weak signals a cooling of the CCD is necessary.

This approach was theoretically investigated in the group of prof. Riesenbergr at Institute for Physical High Technology in Jena.

7.2.2 AOTF Based Design

The spectrometer core of this concept is a tunable monochromator, i.e. a so-called AOTF (acousto-optic tunable filter). The AOTF operation is based on the diffraction of light on inhomogeneities created in an anisotropic crystal medium by a travelling acoustic wave. The incident light is diffracted with a narrow spectral bandpass when a RF signal is applied to a piezoelectric transducer element which creates in turn the acoustic wave inside the crystal. By changing the frequency of the applied RF signal the spectral bandpass can quickly be tuned. AOTFs have been used for Raman applications and their potential in this field was demonstrated [18, 28, 56]. An important characteristic of the AOTF is the ability to transmit images and therefore the use as imaging spectrometer is possible. For the setup, an avalanche-photo diode (APD) used as a photon counter module serves as a detector. This approach was implemented and tested in the breadboard version of MIRAS.

7.3 Breadboard Setup

The testing breadboard was built as shown in Figure 7.1. The individual components are a laser diode lasing at 785 nm, an interference filter built for 785 nm, two notch filters, a microscope objective optimized for NIR spectral region from Mitutoyo and an AOTF unit with a photon counting module based on an APD

as the spectral sensor.

The laser beam is reflected from the first notch filter into the microscope objective after passing through the interference filter. The incidence angle onto the notch filter is close to 5° and therefore close to 100% reflection of the laser light is achieved. The microscope objective, having a large numerical aperture (0.5 to 0.8) focuses the light on the sample. The scattered light is collected by

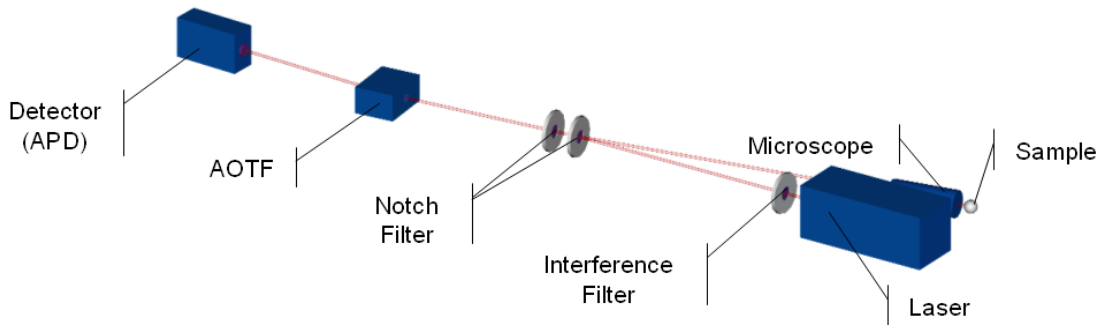


Figure 7.1: MIRAS -Unfolded setup based on an acousto-optic tunable filter (AOTF)

the same microscope objective and collimated onto the first notch filter. Only the spectral components outside the notch band are transmitted further towards the second notch filter. The two notch filters accomplish a Rayleigh rejection of 10^{-12} at the laser wavelength. After the filtering box the Raman signal reaches the entrance to the AOTF. The diffracted beams (first order beams, *see* Figure 7.2) are leaving the filter at approx. $\pm 7.5^\circ$ with respect to the incident light direction. The diffracted beam which has the polarization close to the polarization of the incident laser is collected and focused on the active area of an APD detector. In the following sections all the components are described in more detail.

7.3.1 Laser

To obtain Raman spectra of sufficient quality, the laser beam quality and shape as well as the selected wavelength play a major role. A continuous wave laser illumination during the measurement is preferred to reduce the necessary laser power and also keep the overall measurement time as short as possible.

Laser diodes are efficient (50% conversion rates are normal) , compact and inexpensive light sources. They are mass-produced for applications like bar code

scanners, CD players or computer optical drives. However, their use for Raman spectroscopy has been limited due to the large spectral laser linewidth and the problematic control of the output frequency. This problem can be overcome with External-Cavity-Diode Lasers (ECDL). The Diode Laser DL 100 from Toptica is such a system built in Littrow scheme.

A normal laser diode has a very short resonator (about $300 \mu\text{m}$, being formed by the cleaved facets of the semiconductor material) with a poor reflectivity of typically below 30% from the facet resonator cavity, leading to a large free spectral range⁶. In an ECDL however, the diode strays light by feeding back a part of the emitted laser light spectrally filtered into the laser diode. In most ECDLs today, an external grating situated in front of the diode laser is used for this purpose. While the first order from the grating is back-reflected into the laser diode, the zero order is coupled out for use in the experiment.

The laser used here has such an extended cavity set-up (Littrow configuration). Optical feed back into the laser diode from the first order of a grating builds the external resonator between the rear facet of the laser diode and the spectrally selective grating. The linewidth is therefore drastically reduced and the wavelength of the laser diode may be eventually controlled by tilting the grating (within the gain profile of the laser diode). Active temperature control with a Peltier cooler (TEC) connected to the temperature control unit minimizes slow thermal drifts of the diode laser resonator.

The diode used for the MIRAS breadboard (see Fig. C.2) has an output power of 80 mW at 785 nm . The power after the external resonator is of only 40 mW . The beam shape coming out of the system is not circular having an oval shape⁷ with radii in the rapport of 1:1.7. For maximizing the coupling with the microscope objective the beam shape was corrected using an anamorphic lens system.

7.3.2 Filter Box

In the breadboard version of MIRAS, two notch filters (Kayser Optical Systems Inc. HSPF-785-1.0 catalog number) serially mounted were used to achieve a

⁶typically in the range of 100GHz

⁷this is a characteristic of the diode, dictated by the way the junction is geometrically formed. In the meanwhile there are diodes available with a circular beam output

sufficient laser suppression. The notch filters used are of a holographic type having a maximum suppression factor of 10^{-6} centered at 785 nm when used at 5° incidence and a transmission coefficient for wavelengths out of notch band of over 75%. The notch band has a width of approx. 350 cm^{-1} with an edge width on the Stokes side of 86 cm^{-1} . Normally this type of notch filters can be used up to temperatures of $+80^\circ\text{C}$ without sustaining damage to the holographic gelatine substrate. This should be fully compatible to the Mars mission requirements with respect to maximum temperatures. Thermal cycling must also be taken into account. As an alternative, a Rayleigh filter box, making use of reflecting coatings, have been considered. The preliminary assessment and optical design studies⁸ show that a suppression of 10^{-12} for the laser light and a transmission for the Raman signal of up to 70% will be achievable.

7.3.3 Raman Head: Optics

Quantification of mineral proportions in rocks and soils by Raman spectroscopy on a planetary surface is best done by taking many narrow-beam spectra from different locations on the rock or soil, with each spectrum yielding peaks from only one or two minerals. Therefore a microscope lens for focusing the laser light on the sample is to be employed. The system must have a large working distance for an easy positioning relative to the sample⁹ and at the same time a large numerical aperture for maximizing the collected backscattered signal.

The breadboard uses the microscope lens from Mitutoyo (NIR x100, f=200). Reflective optics have also been considered as an alternative but were not implemented in the final setup. Significant reduction of lens size is feasible with comparable performance. The total laser power reaching the sample is only 12 mW , after passing through the microscope lens.

7.3.4 Acusto-Optical Tunable Filter

The AOTF system is made of a tellurium-dioxide crystal¹⁰ with piezoelectric transducers mounted on a side. By applying a radio frequency signal to the

⁸optical design layouts were tested in ZEMAX software packet

⁹a robotic positioning and samples of different shapes and sizes

¹⁰anizotropic material

piezoelectric transducer, an acoustic wave is created inside the crystal. The cutting of the crystal makes the creation of static waves inside the crystal possible. This acoustic wave spatially modulates the refractive index throughout the crystal, and this leads to the diffraction of light. The principle is schematically shown in Figure 7.2. The entrance aperture is of $5 \times 5 \text{ mm}$, having an acceptance angle

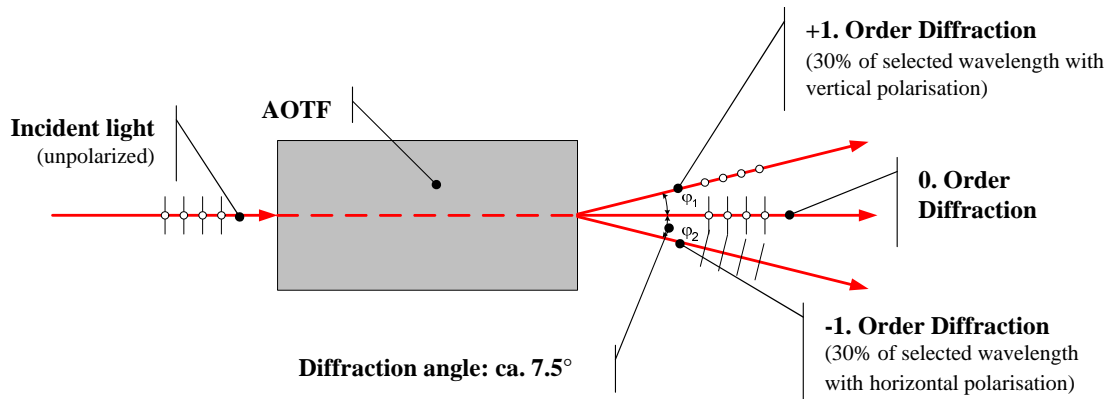


Figure 7.2: AOTF - functioning principle

of 5° in the horizontal plane¹¹ and of 3° in the vertical plane. The output of the AOTF consists of 3 beams. The first order diffracted beams are linearly polarized with polarization directions perpendicular to each other. The diffraction efficiency is of approx. 30% for each first order beam. The separation angles of the two relative to the incident beam is of $\pm 7.5^\circ$. The filter can address wavelengths from 650 to 1150 nm for this using RF from 230 MHz down to 125 MHz , with a switch speed between two spectral positions of 1 ms . The spectral resolution is 0.31 nm at 633 nm and 0.64 nm at 970 nm .

The power needs of the system is 2 W for the RF generator and an overall 10 W including the control electronics. The warm-up time is in the range of 15 minutes. Thermal stabilization of the crystal is not required as long as there is an internal calibration standard.

The unit used in our experiment showed a slight drift for the first order diffracted beam as the diffracted wavelength was moving beyond $\approx 920 \text{ nm}$. This is creating difficulties at collecting and focusing the diffracted beam onto the detector active area. The filter calibration curve is a non-linear function (diffracted wavelength as function of the RF applied). By using a Hg-lamp the system can be calibrated

¹¹the figure's plane in figure 7.2

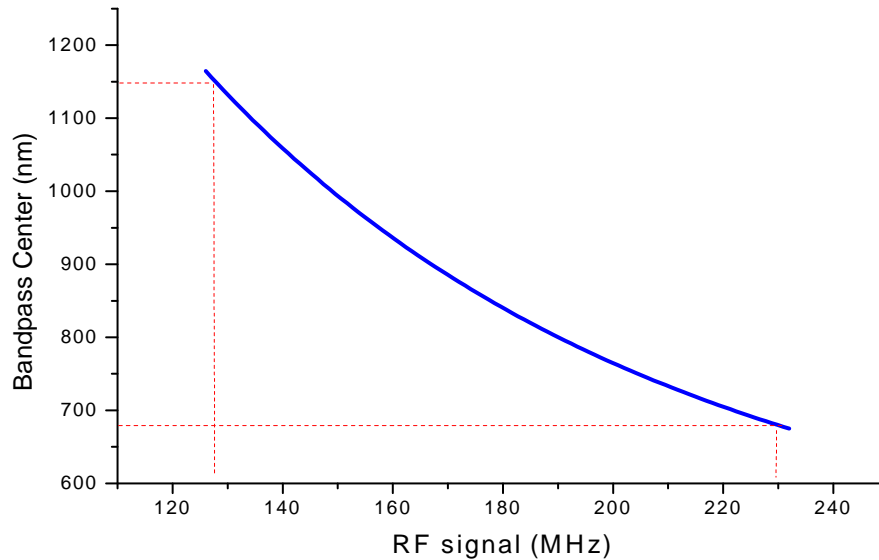


Figure 7.3: AOTF - calibration curve

roughly in 20 points. The finally calibration curve as recommended by the manufacturer is a polynomial function of grade 5. The actual implementation of the calibration curve in the spectrometer control software is described in section 8.2.

7.3.5 Detector

A single photon counting module from PerkinElmer (SPCM-AQR-15) was used for the detection. The module is based on an avalanche photo diode operated in 'Geiger mode' and active quenched in order to shorten the dead time which normally occurs after each photon count event. The diode is a silicon diode and therefore has similar wavelength sensitivity as all silicon based detectors (cut off at $\approx 1050 \text{ nm}$). The quantum efficiency of the module, as stated by the manufacturer, is shown in Figure 7.4. The peak QE is stated to be $\approx 72\%$ at $\lambda 700 \text{ nm}$ with values of $\approx 65\%$ at 785 nm , going down to less than 2% at 1050 nm . The active area of the SPCM-AQR-15 detector has a diameter of only $175 \mu\text{m}$. This becomes a problem when optically interfacing this detector to the exit of the AOTF. The focusing lens has to behave like an acromat for the spectral region of interest. When focusing the exit beam from the AOTF onto the detector, due to the slow drift discussed in Section 7.3.4, the focused image moves, modifying the actual total throughput of the system. Another problem can be encountered

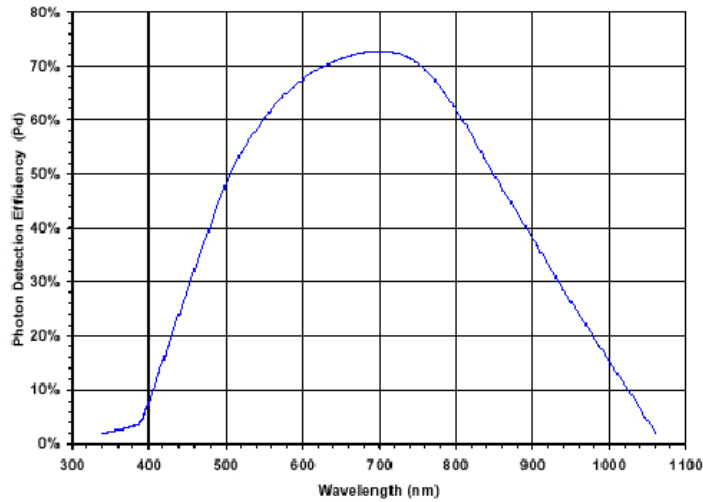


Figure 7.4: Avalanche Photo Diode Quantum Efficiency.

especially when measuring with low integration times¹² and the system is exposed to low frequency vibrations. The low frequency vibrations may cause the focused image to move on the detector surface¹³ (or even partially out of it) and this periodical change in the incident intensity might create beating into the recorded signal¹⁴.

There are other different factors that have influence on the recorded signal when using an APD as photon counter. Among them are the dark count instabilities (not detected for our unit), pile-up and afterpulsing (*see* Section 8.2), diode afterglow and junction heating¹⁵. The only effect that influences the overall signal in our application is the pile-up effect. The software implementation correcting this effect is described in section 8.2. Other characteristics for the detector are: a detection range between 400 nm and 1050 nm and a dead time of 50 ns. The maximum count rate is of 10^7 counts/second with the dark counts at the room temperature at 50 c/s. The overall size of the unit is: 127 x 63,5 x 33,5 mm. The typical power consumption is 2,5 W with a maximum of 6.5 W at high count rates.

¹²under 100 ms

¹³spatial inhomogeneity of the detector surface makes the recorded signal change

¹⁴two periodic events - the low frequency movement of period τ_1 and the integration time interval τ_2

¹⁵QE modifies with the temperature hence temperature control for the unit is required

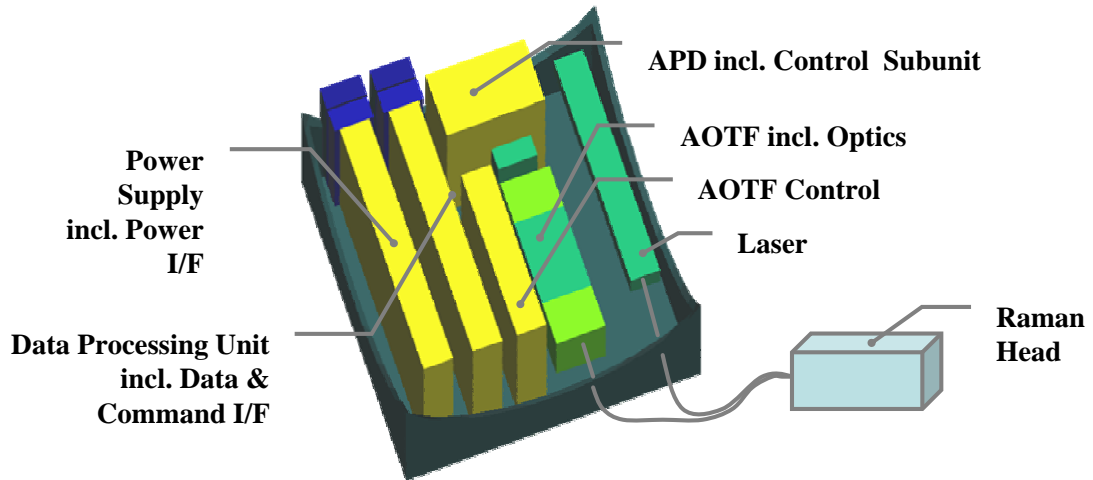


Figure 7.5: MIRAS -Folded setup based on an acousto-optic tunable filter (AOTF). The overall dimensions are 150 x 150 x 100 mm for the MIRAS central unit and 35 x 35 x 80 mm for the Raman head.

7.4 Conclusions

After the experience gained from the breadboard tests, the conclusions that were drawn regarding the main mission requirements (*see* Section 7.1), are summarized in Table 7.3 and 7.4. Both designs meet the requirements with regard to the mass constraints. The AOTF based spectral sensor is marginally heavier than the one based on the Hadamard - transform spectrometer. The difference arises mainly from the need of additional optics for matching the exit of the AOTF with the

Mass Budget	AOTF	Array Spectrometer	Remarks
Central Unit	1650	1600	Mass in g
Structure	300	300	
Power Supply(PS)	300	300	
Data Processing Unit	300	300	
Laser	300	300	
Spectrometer	450	400	
Sensorhead	150	150	
Total Mass	1800	1750	Mass in g

Table 7.3: MIRAS Mass Budget

Power Budget		AOTF	Array	Remarks
		AOTF	Spectrometer	
Central Unit		19157	12086	mW
	Power Subunit	5747	3626	at 70% efficiency
	Laser Control Unit	1000	1000	
	Laser Head incl. TE cooler	3760	3760	80mW output diode eff. 40% 350mW TE 10% eff.
	AOTF Power Amplifier	4000	-	7200(BB)
	AOTF Synthesizer	500	-	1800(BB)
	AOTF Modulator	500	-	1000(BB)
	AOTF Thermal Control	0	-	no TEC foreseen ¹⁶
	APD Detector Subunit	2500	-	6500 mW peak at high count rates
	Spectrometer Slit Ctrl.	-	50	
	CCD Control & Readout	-	1000	
	CCD TE Cooler	-	1500	
	Experiment Control and Data Acquisition	1000	1000	
	Data and Command I/F	50	50	
Sensorhead		0	0	
Total Power		19157	12086	mW

Table 7.4: MIRAS Power Budget.

entrance of the APD detector.

Concerning the instrument volume, both devices can be accommodated in a volume of approx. 2.35 dm^3 as shown in Figure 7.5. The unfolded setup used for the breadboard version is motivated by the need of having a larger maneuverability for different components in the alignment process, which necessitates extra positioning of mechanical parts.

With regard to the total power need for the instrument, the first estimations based on the breadboard are over the initially set requirements. As shown in Table 7.4 the power needs estimations for the AOTF based instrument are roughly 3 times larger than the required 6 W, and for the array spectrometer is 2 times

¹⁶the shifts due to long term thermal instabilities are followed by using an internal calibration line

larger than required. The differences between the two models mainly arise from the higher power needs for generating, amplifying and sustaining the RF field for the AOTF as well as from a higher power need of the APD at higher counting rates. Regarding the command and data link budget, the instrument does not

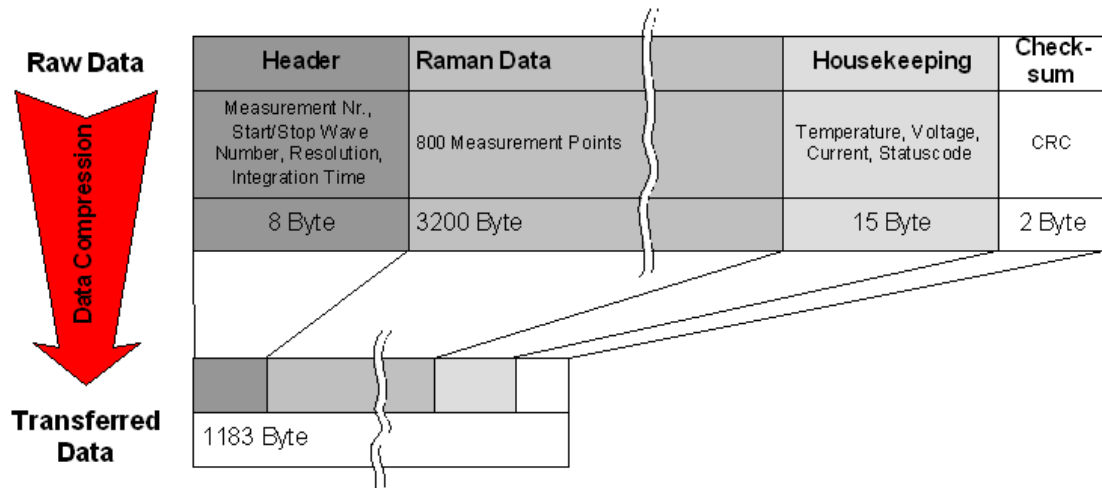


Figure 7.6: Data structure and achievable compression.

need more than the upper limit of 2 Mb for minimal operation time, if the system does work automatically and data is compressed on the main processing unit as shown in Figure 7.6.

7.4.1 Extended MIRAS

The conclusions drawn from the MIRAS study are used for further developing a combination of a Raman spectrometer and a microscope. The project is planned to continue under the name of "Extended-MIRAS" [62]. The basic approach is shown in Figure 7.7. The microscope is having a design close to the device provided for the Beagle 2 mission and is developed by the group of Prof. Thomas, N. at Physikalisches Institut, University of Berne [89]. The Raman spectrometer is planned to be a Hadamard transform unit. The connection between the two functional units is planned to be made with a dichroic mirror which directs the microscope image to the microscope detector while allowing the Raman scattered light to pass through to the Raman section of the instrument. The use of a single objective lens for the Raman spectrometer and the microscope ensures that the

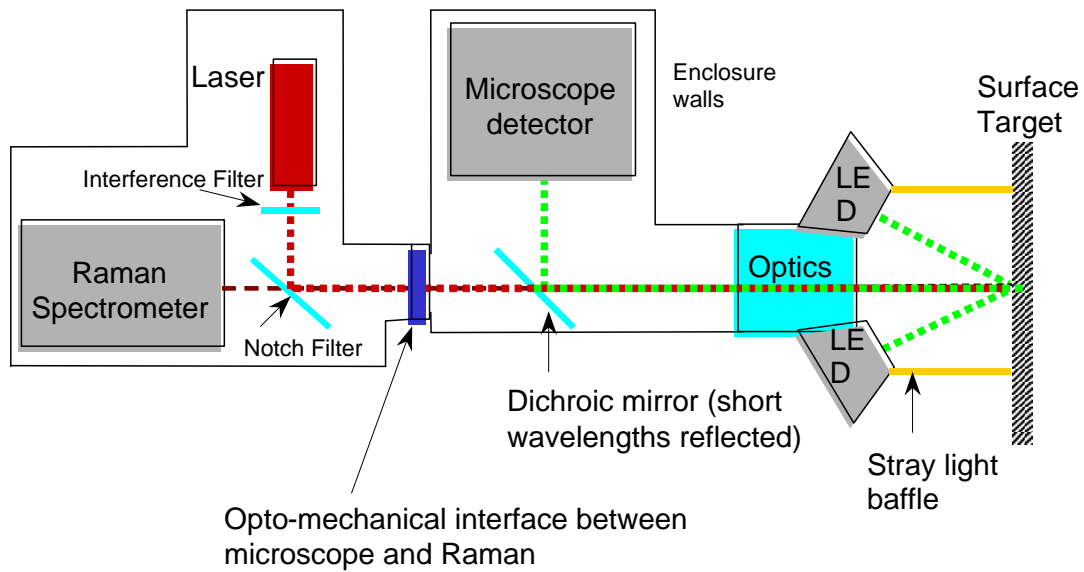


Figure 7.7: Extended-MIRAS: Raman-Microscope combined instrument configuration.

position of the laser spot on the sample is known. This allows one to place the Raman spectrum into context with the visible image.

Raman measurements performed with the breadboard version of MIRAS are presented in chapter 9.

Chapter 8

MIRAS - Software Implementation

A PC-based instrument control software was specially designed for the MIRAS instrument. The software controls both the AOTF RF-generator (*see* Section 7.3.4) and the APD photon counter module (*see* Section 7.3.5). Since both primary PCI cards used for controlling the two devices are counters, the whole control unit could have been implemented on only one PCI card having multiple independent counters (is the case of both ADLINK PCI-7230 and PCI-8554 used). For the generation of the driving signal of the AOTF the ADLINK PCI-7230 counter card was used as a pulse generator and for the APD signal detection the ADLINK PCI-8554 card was used as counter. Due to extremely high counting rates for the APD, two counters on the card were used in cascade, offering a total dynamic range of 2^{32} (roughly 4 billion counts)

8.1 Measuring Procedure

The AOTF based setup was used with only one point detector (APD), collecting just one of the two diffracted beams (*see* Section 7.3.4). The measurements were

done on a single channel, therefore measuring each spectral point at a different time (the AOTF functioning principle gives no alternatives). The measurement procedure basically consists of driving the filter to the spectral position where the measurement is to be done, integrating for a certain time interval and then reading the detector, followed by the movement of the filter to the next spectral position. Special attention has to be given to starting the measurement after the AOTF has stabilized at the desired position. Usually the switch interval between two spectral positions is in the range of 1 *ms*¹. After the filter has reached the spectral window to be measured, both counters (PCI-8554 cascaded) are reset and the time of reset noted. When the interval of accumulation has passed, the counters are read and the reading time is noted. The acquired count value is then processed and the measuring cycle can be repeated.

8.2 Data Processing: Corrections

After the point measuring procedure delivers the data point (recorded counts at a certain RF applied on the AOTF crystal), there are a series of data processing steps which are applied to this data point in order to correct for various undesirable effects.

Time corrections The acquired count value has to be corrected for the deviations in accumulation time due to operating system internal processes (e.g. processor interruptions). This correction is performed by closely monitoring the interval between resetting and reading the counters, independently from the timed triggering provided by the operating system.

Detector sensitivity An optional correction is for the detector sensitivity. These corrections are made linearly on four different spectral regions as shown in Figure 8.1. The exact spectral response of the detector can be implemented if exact values for the reported intensities are needed.

¹When the frequency of the RF is changed, the time it takes for the acoustic wave to fill the AOTF crystal is typically only 20 μsec . 1 *ms* accounts for possible switching delays in the electronics.

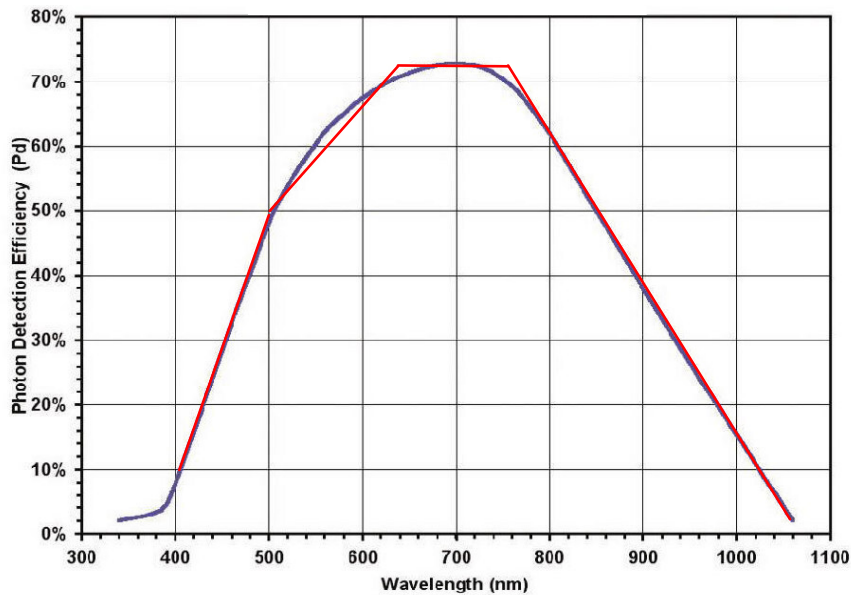


Figure 8.1: Detector quantum efficiency and the first linear approximation used for correction. The four linearly approximated regions are ≈ 400 to 500 nm, from 500 to 650 nm, from 650 to 750 nm and 750 to 1100 nm.

Pile-Up and Afterpulsing corrections Depending on the counting rate at which the detector was measuring, there is another correcting factor that has to be applied. At low counting rates the correction is:

$$\text{correction factor} = \frac{1}{1 - (t_d \cdot C_R)} \quad (8.1)$$

where t_d is the module's dead time between two counting events and C_R is the reported counting rate. At high counting rates, this correction factor grows exponentially (*see* Figure 8.2). This is also known as pile-up correction and is used when separated photons no longer produce at the detector separate signals (e.g. a second photon arrives during the detector's dead time frame created by the recording of the first photon). If the saturation point is reached, the counting rate will start to decrease with the increasing intensity of the incoming signal. Therefore at high levels of light intensity the counting rate will reach zero.

There is another correction that is usually employed when using photon counting devices, namely the afterpulsing correction. APD afterpulsing are multiple output counts for a single input photon. The afterpulse pulses are time delayed compared to the signal from incident photon and the time delay is proportional

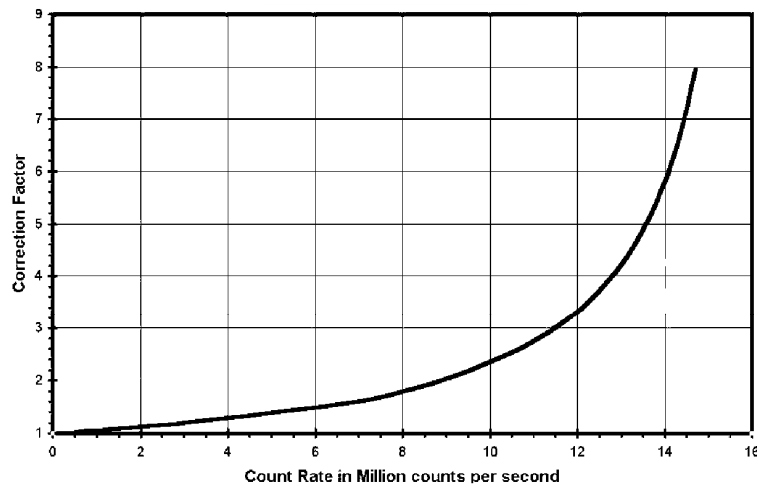


Figure 8.2: Typical correction factor due to pile-up effects.

to the path length for the electron propagating in the active area of the detector. The pile-up correction has to be performed before the afterpulse correction or any other corrections, because the pile-up effect is nonlinear. The pile-up is affected by the signal strength, signal background and afterpulsing and therefore, data has to contain the information from all these factors when the correction for pile-up is performed. Having large integration intervals, the afterpulsing will add up to a quasi-constant offset which is of no importance for our measurements. In this case a correction was not necessary to be implemented (*see* Figure 8.3).

In the above mentioned configuration, the primary values that are used for building a spectrum are the counts from the APD and the RF signal sent to AOTF. The driving limits for the AOTF were 126 MHz (approx 1164 nm) and 232 MHz (approx 675 nm), with a precision in positioning at a certain frequency of 10 kHz (approx 0.58 cm^{-1}). As recommended by the producer of the AOTF unit, the calibration curve is a polynomial function of grad 5 which helps translating from MHz to nm . The inverse transformation is no longer possible using the same function². Since the software interaction with the user is mainly made by communicating the values in nm or cm^{-1} , for not having differences between the direct and inverse transformations, the calibration curve was sampled in approx. 100 points and the intervals between points were considered line segments. The curve created in this way is the actual calibration curve implemented into

²one needs the analytical solutions for a general polynomial eq. of grad 5

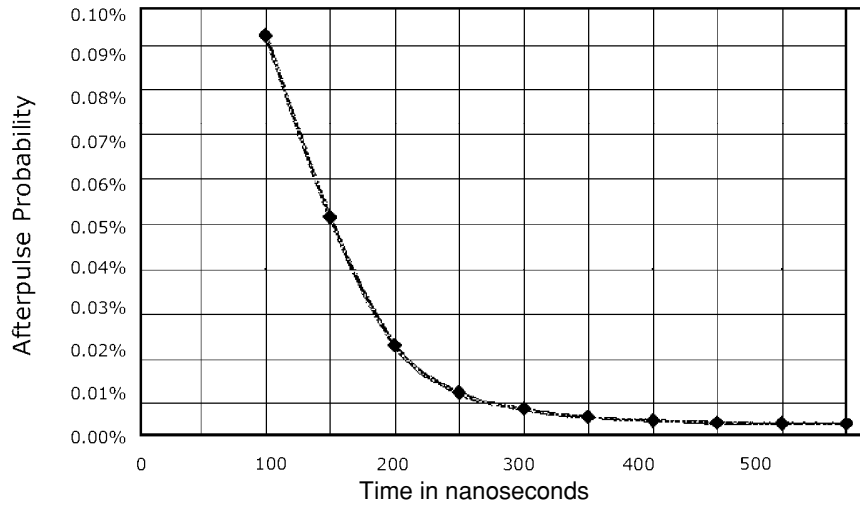


Figure 8.3: Afterpulsing probability for an APD photon counting device.

the controlling software for the AOTF. Aside from the calibration errors already existing in the calibration curve provided by the manufacturer (up to 5 cm^{-1}), a non uniform error of up to 5 cm^{-1} is further introduced into the calibration profile by using this linear approximation on intervals.

The normal measurement involves fixing the start and end of the spectral interval to be measure, the driving step size and the time of integration for a measuring point.

In order to allow for an adjustment of the sample in front of the microscope's objective, in such a way that a maximum Raman signal is collected, or for aligning the exit of the AOTF with the collecting optics of the photon counting module, a function was implemented into the controlling software which enable the user to drive the filter back and forth between two different wavelengths and compare the intensity differences at these two spectral positions (see Figure 8.4). Other options, for example, allows the user to drive the filter manually, change the calibration file and the displaying units between MHz , nm and cm^{-1} .

8.3 Supportive Database: Implementation

The database implementation described here, which is still far from being comprehensive in structure and content, provides a framework for a spectral in house database which will be of use to mineral related investigations. With small modifi-

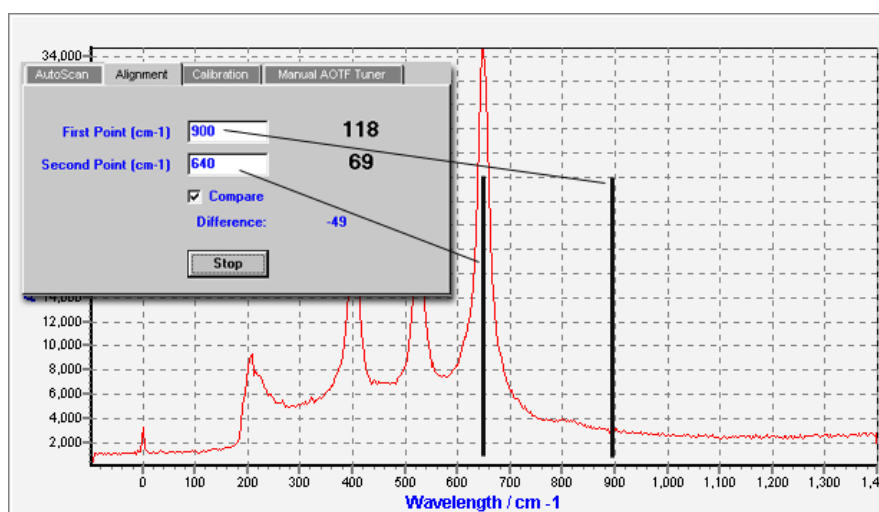


Figure 8.4: User interface for the alignment function

cations, other types of materials can be accommodated. The only difference is the classification which for the minerals was implemented directly into the database structure. The technical approach is to have a relational database implementation with indexes defined for the tables that are of interest and are usually searched (raman band positions, mineral names etc.). The basic structure is shown in Figure 8.5. This structure does not show the tables for storing the structure information, microprobe analysis, X-Ray diffraction spectra and everything else which may contribute to a full characterization of the mineral. There are external databases which are linked to the mineral database and hold scientific references, classification information or different other classifications. The database also has a user interface (*see* Figure 8.5, C.6, C.7, C.8). The way in which the Raman spectra are chosen is explained in section 6.1.

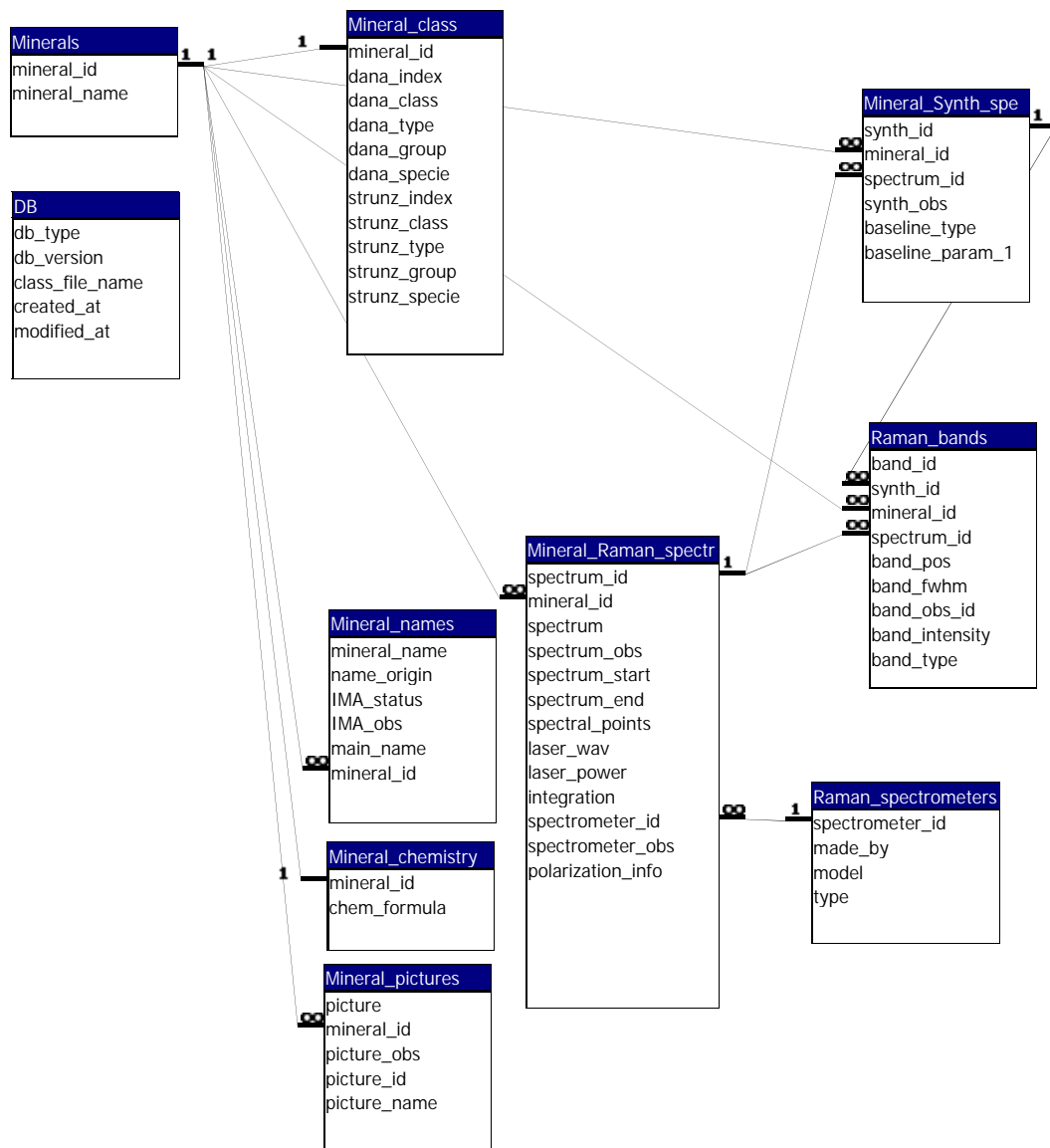


Figure 8.5: Employed relational database structure for Raman spectra of minerals.

Chapter 9

MIRAS - Bread Board Measurements

The AOTF filter used on the breadboard version of MIRAS was constructed by IFU GmbH and it was custom made to work at high resolutions (specified at 5 cm^{-1}). In Figure 9.1 the Raman spectrum of olivine is recorded with a 500 ms integration time per point and with different spectral step sizes. Measured with a laboratory Raman spectrometer, the two bands characteristic of olivine are at 825 cm^{-1} and 856 cm^{-1} . The breadboard measurement shows a good separation of the two bands ($\approx 65\%$) and therefore a resolution at least better than 15 cm^{-1} .

The system was not optimized in terms of throughput. From the initial 40 mW (80 mW diode output) of the laser, only approx 12 mW reached the sample, due to losses on the anamorphic lens system, at the notch reflection and on the microscope lens. From here, the Raman scattered light collected by the M.O. is sent with approx 32% losses to the filtering box. The notch filters each have a transmission of $\approx 80\%$ and therefore the loss after the filter box is 36% . The AOTF has a diffraction efficiency of maximally 30% for each first order diffracted beam and the optical system that focuses the light onto the detector has a transmission of maximally 88% . Due to the estimated mismatch between the detector active area ($175\text{ }\mu\text{m}$) and the size of the image created by the focusing lens (ap-

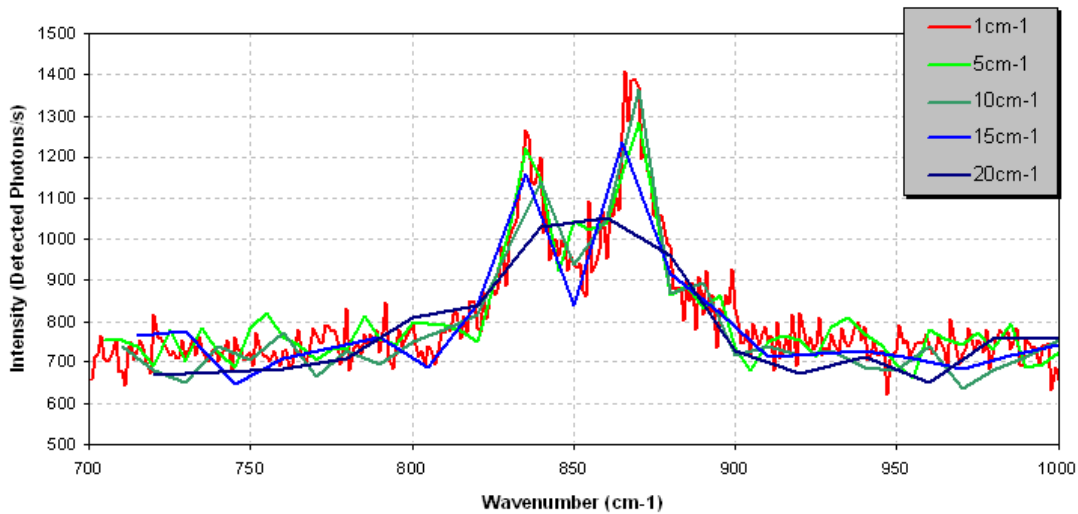


Figure 9.1: Raman spectra of olivine measured with the MIRAS breadboard (AOTF configuration) using different spectral step sizes in recording. Integration time per measurement point is 500 *ms*.

prox. 200 μm), the losses are of approx. 24%. The total signal that reaches the detector is therefore only about 10% of the initial Raman signal. The maximum achievable throughput by collecting both diffracted beams from the AOTF and managing to bring the whole diffracted light onto the detector with simple optics coated for NIR, is approx. 36%. With all this poor throughput the sensitivity of the detector still permits integration times of a few hundreds microseconds when measuring a mineral with a medium scattering power as olivine. Figure 9.2 shows the same olivine spectrum measured using different integration times (the spectra are normalized to counts/second). The two bands are still visible at 300 *ms* integration time. The noise level is normally higher.

Other Raman spectra measured with the breadboard version of MIRAS are shown below in Figure 9.3 for a silicon crystal with integration times of 1 *s* per point, and in Figure 9.4 for a polycarbonate matrix. The regions over 3000 cm^{-1} are not accessible due to the very low quantum efficiency of the detector in that spectral region. Due to the sequential measurement procedure, with each spectral point being measured at a separate point in time, even if the integration time per point is small, the overall time needed for recording the whole spectrum is large. For a remote planetary use of such a system, this translates into energy consumption. A multichannel detection approach (like the Hadamard-transform

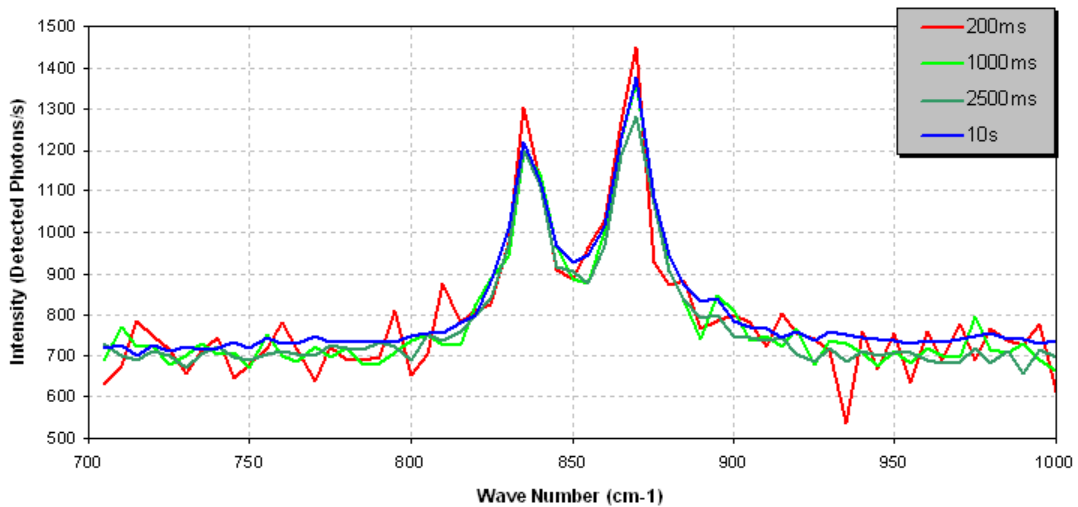


Figure 9.2: Raman spectra of olivine measured with the MIRAS breadboard (AOTF configuration) using different integration times. AOTF scan step set at 5 cm^{-1}

spectrometer is) seems more suitable. The use of an AOTF based system has advantages over other systems if the experiment requires imaging capabilities or if only specific substances are monitored and short spectral intervals are recorded. An example of a Raman image taken through the AOTF is shown in Figure 9.5. The point APD detector was replaced by a planar CCD and the sample illumination was performed from aside, with a spot size on the sample of approximative $50 \mu\text{m}$. The signal-to-noise ratio of a Raman spectrum is poor when a sample is stimulated by a low-power laser beam of broad diameter, hence for illustration purposes a powerful scatterer was used. The sample consists of anatase (TiO_2) with polyethylene beads embedded. The image taken at 641 cm^{-1} shows the distribution of anatase. At 580 cm^{-1} there is no intense vibration neither for TiO_2 nor for polyethylene. The Raman signal strength produced by a mineral in a rock or soil is not related in a simple way through the Raman scattering cross section of that mineral to its proportion in the rock. Therefore, the intensities in the images only roughly show the spatial distribution of a certain component without assessments on the mineral concentration being possible. Imaging with this method has the advantage of being fast but the method is hindered by image phantoms created by reflections and fluorescence [56, 90].

Comparing the two proposed designs, for a standard Raman experiment, the

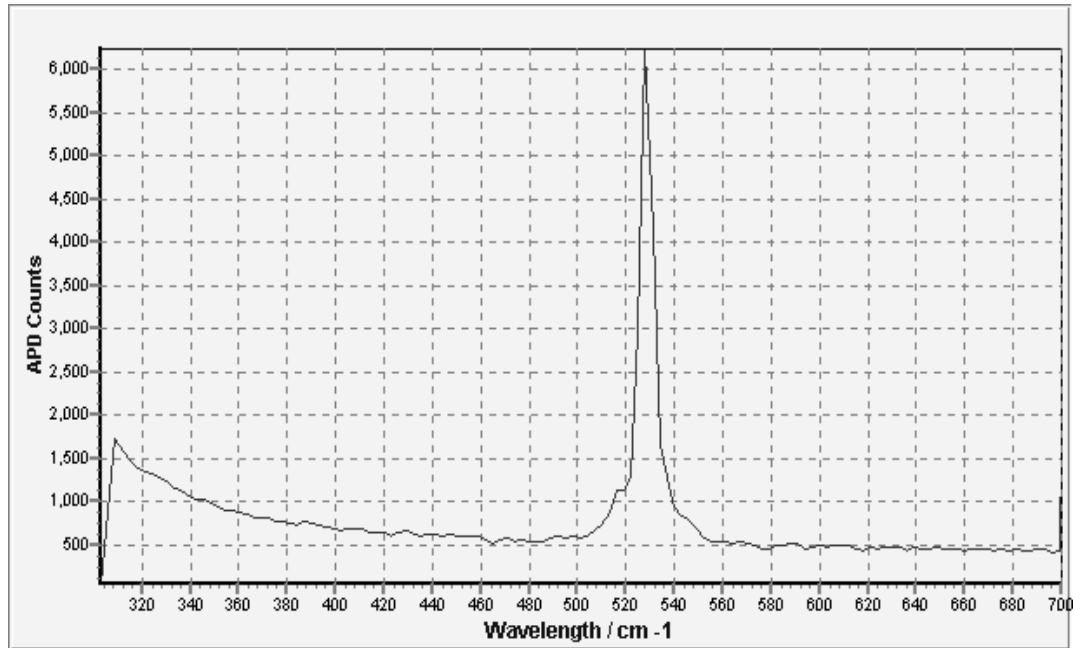


Figure 9.3: Raman spectrum of Silicon measured with the BB version of MIRAS. Integration time of 1 second per point.

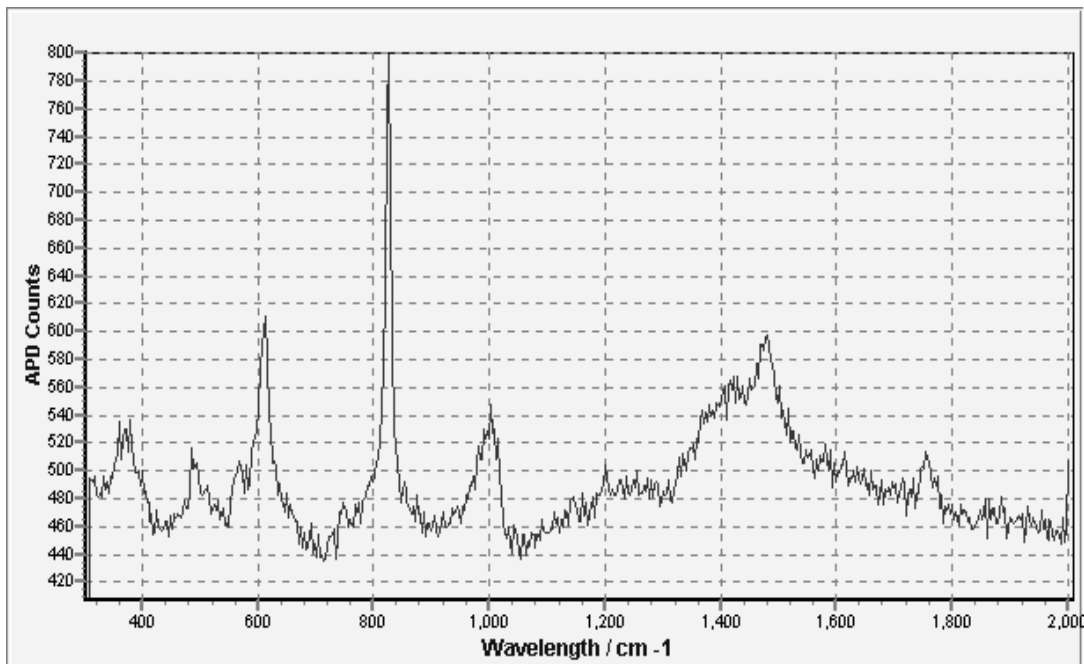


Figure 9.4: Raman spectrum of a polycarbonate matrix measured with the BB version of MIRAS. Integration time of 10 second per point.

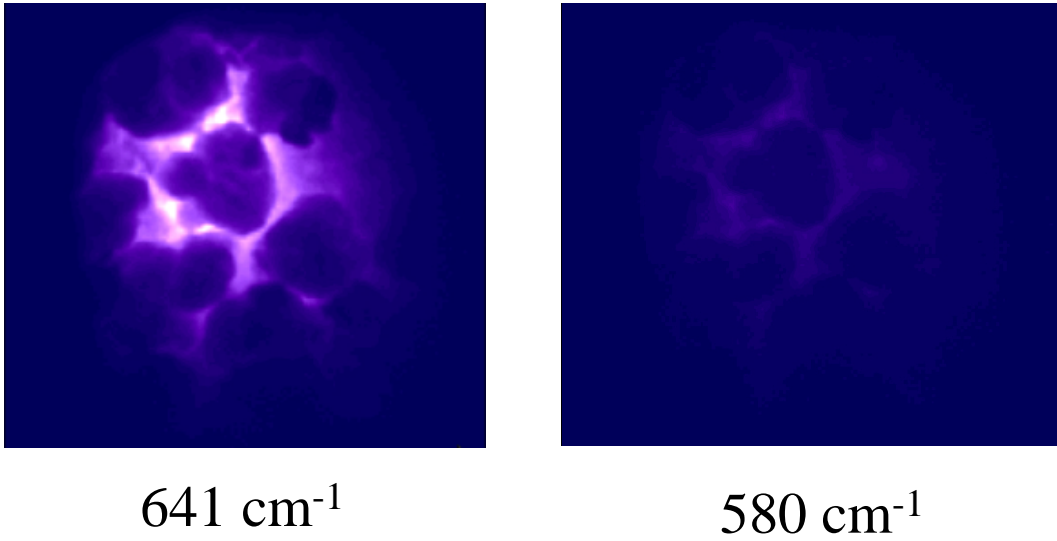


Figure 9.5: Image taken through the AOTF of a mixture of polyvinyl particles in TiO₂. The band at 641 cm^{-1} is characteristic for TiO₂. The integrating time is 10 s for each frame.

choice is for a dispersive multichannel spectral sensor of type Hadamard-transform (even if the performances for Raman applications for the Hadamard-transform spectrometer were only theoretically estimated). The approach using an acousto optical tunable filter (AOTF) as the wavelength selecting and deflecting element remains as an alternative when special experimental conditions are to be met (looking for known substances, imaging etc.). Even if the scientific relevant performances for the AOTF based design are comparable to the Hadamard transform spectral sensor, the AOTF set-up has higher power needs over comparative longer times. Since the power resources are very limited in a remote planetary mission, the Hadamard approach is the preferred one.

Chapter 10

Remote Raman Spectroscopy for Planetary Prospecting

Since the advent of the space age in 1957, all planets in the solar system, except Pluto, have been visited by space craft. Dedicated missions were launched to observe the planets, comets (e.g. Halley), asteroids (e.g. Eros), interplanetary dust or the Sun. Remote sensing instrumentation, such as cameras operating in the infrared, visible or ultraviolet regime or even X-ray and Gamma spectrometers have been used as imaging devices for mapping areas of interest. The Moon is the best example for remote (and in-situ) studies of the mineralogy of extraterrestrial surfaces. The reason for this is that during the Apollo Lunar missions about 450 kg of rock and soil have been collected and brought back to Earth for further analysis in laboratories. Therefore, remote sensing observation could be directly compared to in-situ observations. To a limited extent this applies to Mars due to in-situ observations by Viking and Pathfinder missions. Remote Raman spectroscopy (RRS) would be a new tool for performing in-situ and/or remote studies of bodies in our solar system. Such a Raman instrument should be capable of identifying and mapping the minerals on surfaces or measuring atmospheric

compounds, and therefore add a new analysis tool to the existing remote sensing instrumentation. While remote Raman spectroscopy from orbiting instrument platforms would open a new field of research, in-situ Raman spectroscopy using a lander or Rover, e.g. for Mars, has been already a well established research field for about a decade[97, 95, 20]. The range for such a remote measurement device is from about 10 m to 100 m in the vicinity of a landing site on a planetary body[79].

The goal of remote Raman scattering experiments is the mineralogical characterization of the planetary surface, extending the presently possible qualitative analysis (via reflectance or infrared spectra). A very interesting application would be the Raman analysis of hot surfaces, such as Mercury, since then the anti-Stokes shifted Raman lines can be easily measured and the plight of fluorescence in the Stokes domain will be minimized. Normally, RRS should make use of a sensor placed on an instrument platform (satellite), orbiting a planet, asteroid, moon or comet. The instrument consists, in general, of a laser (most likely a pulsed laser) and a spectrograph, combined with a telescope for the observation of the scattered light. Since there are some examples in the literature using solar radiation as a light source to study Raman scattering of planetary bodies[110], it might be possible to design an instrumentation just using a spectrograph and a slit camera or telescope working in the UV region and using the Ly- α solar radiation as a distinct solar line (Raman scattering of H₂ for Ly- α has been observed for Uranus atmosphere by Yelle et al. [110]). Since the Raman cross-sections for minerals are much weaker than those for hydrogen molecules, it is expected that such a sensor should have a wide dynamic range.

10.1 Micro Raman and Raman LIDAR

Raman spectroscopy is currently carried out as an in-situ technique with distances from probe to instrument ranging from a few millimeters to centimeters only. In most cases it is essential to investigate a tiny fraction of the probe surface, hence the use of microscope optics in order to generate an illuminated spot of only a few micrometers in diameter. The optical power of the - mostly - continuous wave (cw) lasers (used for Raman excitation) is in the order of a

SUBSYSTEM	MICRO RAMAN	RAMAN LIDAR
Laser Type	Laser diode, Nd:YAG	Excimer, Nd:YAG 3 rd harmonic
Laser Wavelength	VIS, NIR, UV	UV
Laser Power	(100) mW	(1000) mW
Transmitter Optics	Microscope	Beam expander
Receiver Optics	Microscope	Telescope
Receiver Aperture	(0.00002) [m ²]	(0.8) [m ²]
Power-Aperture-Product	0.002 [mW · m ²]	800 [mW · m ²]
Spectral Analyzer	Grating, Filter Fourier-Transform	Grating
Detector	CCD chip	APD, PMT
Measurement Range	mm to cm	Km
Measurement Time	sec to min	min

Table 10.1: Comparison of average subsystem properties for a Micro Raman system and a Raman LIDAR. Numerical values in brackets are mean representative data for this class of instrument, which may vary due to individual instrument layouts.

few mW, due to the extreme small distance to the probe and the necessity not to degrade or even destroy the probe material during its examination. Raman LIDAR systems, on the other hand are being used to perform single- or multi-species analysis of atmospheric trace constituents, and mainly comprise the same optical subsystems as needed for an RRS instrument for surface investigations. A typical Raman LIDAR is using a laser wavelength in the UV region (e.g. 355 nm) which offers a number of operational advantages such as: highly efficient detectors (e.g. avalanche photodiodes, photomultiplier tubes), efficient suppression of background radiation (solar blind region - in case of low altitude instrument location) and enhanced cross-sections for atmospheric Raman scattering.

Table 10.1 compares representative values for both instrument families, covering all major subsystems. Table 10.1 can only provide initial and coarse data, since the technical characteristics of existing instruments vary considerably. The goal is to identify the major differences and also to show similarities that can be used during the extrapolation of laboratory Micro Raman Spectroscopy and LIDAR Raman Systems towards Remote Raman Spectroscopy. The Power-Aperture-Product (PAP) is a well established numerical parameter for the comparison of instruments that are sharing the same physical background, but are

different in size and power. Here, it is immediately visible that a laboratory scale Micro Raman system and a conventional Raman LIDAR are being operated in substantially different PAP regimes.

10.2 RRS Instrument Simulator

A thorough numerical analysis of the link budgets for a RRS instrument has been performed by implementing a flexible and easy-to-use numerical tool, enabling interested users to perform their own investigations. The RRS simulator is a numerical tool based on spreadsheet tables and is structured in a sequence of activities which address the following aspects: optical transmitter (laser), sounding geometry (orbit data), target characteristics (Raman scattering), optical receiver (telescope), atmospheric properties and optics efficiencies. All these aspects are summarized in the following formula, on which the RRS simulator is based:

$$P(x, \lambda_0 \pm \Delta\lambda) = \frac{c\Delta t}{2} P_0(\lambda_0) \frac{A\eta O(x)}{x^2} R(\theta = \pi, x, \lambda_0) \tau(s, \lambda_0, \lambda_0 \pm \Delta\lambda) \quad (10.1)$$

In eq. 10.1 P stands for the received Raman signal, $P_0(\lambda_0)$ is the emitted laser power, λ_0 the wavelength of the emitted laser power, $\delta\lambda$ the wavelength shift of the Raman signal, A the aperture of the receiver optics, η the efficiency of the instrument, $O(x)$ the overlap integral of the emitted laser beam and the field of view of the receiver, x the distance between instrument and target surface, R is the Raman backscattering coefficient and t the atmospheric transmissivity. The RRS instrument will not only receive photons from the target surface, originally emitted by the transmitter's laser, but also a (significant) background signal, originating from a number of potential sources: including, direct solar radiation (on the sun oriented side of the target), scattered sunlight (e.g. from Earth surface onto the dark Moon surface), scattered sunlight within a local atmosphere near the terminators, stellar background radiation (not to be confused with the 3 K cosmic background), zodiacal light (near the celestial equator), galactic background radiation (near the galactic equator), etc. Due to the character of the current study, the influence of these above-mentioned radiation sources is limited to those with significant potential impact on RRS measurements (e.g. due to their intensity and/or their geometric placement relative to the instrument platform).

For this reason the effect of background radiation was limited to direct solar radiation (on the sun oriented side of the target) and the stellar background radiation. Depending on the particular scenario, specific elements need to be considered. As a consequence, a series of most probable scenarios were considered.

For an '**Earth surface towards moon surface**' scenario, in order to have minimum background illumination from the lunar surface, only RRS soundings around New Moon appear meaningful. However, even then, the surface is receiving the full albedo radiation from Earth, having an average value of 0.3. This reflected light from the illuminated earth disk (Earthshine) is acting as a background irradiance on which the weak Raman shifted signals are superimposed.

For a '**Low Earth orbit to Mars**' scenario, any RRS soundings from an Earth orbit are superimposed on the solar background signal on the Martian surface, since Mars is an outer planet from Terra's point of view. The mean distance of Mars from the sun is 227.9 millions km, equalling 1.523 Astronomical Units (AU). Based on the solar irradiance at Earth (1367.6 W/m^2), the value for Mars is reduced by the inverse square of its distance to the sun, yielding 589.2 W/m^2 . This value has to be taken into account as a background signal for RRS investigations from an Earth orbit towards Mars. The other sources - atmospheric scattering, Earthshine, galactic background radiation (near the galactic equator) and Zodiacal light - are candidates for future investigations e.g. when detailed satellite orbits have been established and a suitable RRS viewing geometry and its dynamics can be simulated.

10.3 Input Parameters and Numerical Simulations

The following sections are addressing the main control parameters as they are appearing in the RRS simulator. Due to the open concept of this tool, it is always possible to add, modify or remove these parameters, if necessary.

Optical Transmitter The optical properties of the laser are among the driving factors for the numerical analysis of the RRS link budget. Since it is not the task to investigate a specific RRS instrument with dedicated characteristics, the simulation is concentrating on overall signal strength. In terms of Raman

spectroscopy this means an integrated analysis across the complete spectrum. Basically, two operational modes need to be addressed for a RRS instrument:

1. pulsed operation where the laser is emitting a bulk of photons within a very short time interval (typically in the ns region) and
2. cw operation where the laser is emitting its radiation for a given time window (>seconds).

The pulsed operation mode offers the advantage that the backscattered Raman information exclusively originates from a well-defined footprint area (where the laser pulse hits the ground). Since the necessary pulse energy needs to be high; the pulse repetition frequency will be low (the laser is power-limited); leading to a sequence (or chain) of separated footprints. In this case, the receiver of the RRS instrument needs to be operated in a time-gated mode. With this synchronized mode, it is possible to reject all unwanted background photons significantly. Therefore, the technical capabilities of the laser and its transmitter optics (pulse energy, pulse repetition frequency, footprint size) need to be addressed in conjunction with a suitable orbit definition (satellite speed, height above ground and inclination). CW operation has the advantage that the subsatellite track is a line across the surface with a path corresponding to the duration of the measurement and the actual orbit data. The receiver will also be operated in a continuous mode which means that the detector of the RRS will be recording a continuous base signal due to the above-mentioned background sources. Due to the fact that the RRS sounding is based on wavelength-dependent information and not on intensity-related information like DIAL sounding (differential absorption LIDAR), it is not necessary to monitor the energy of the emitted laser pulses or the average power of the emitted radiation (in case of CW operation). This monitoring can be limited towards a standard housekeeping function (general control of laser health status). In both cases, the wavelength of the laser needs to be monitored with high accuracy. The laser (independent if being operated in pulsed or CW mode) will not be emitting the raw beam towards the target. Since the distance between the RRS instrument and the target surface will be large (several kilometers) compared to any instrument dimension the beam needs to be collimated in order to generate a well defined and minimum footprint size. Minimizing the footprint size is necessary to achieve a geometric resolution on the planet surface that suits

the needs of the user community. Currently there are no fixed values available but the driving effort is directed towards a minimized footprint size. Limiting the footprint size is achieved by reducing the original divergence angle of the raw laser beam, which is determined by the physical properties of the laser resonator. The laser beam will be expanded from its original diameter (a few millimeters) to a diameter of several centimeters or even decimeters. This expansion has an additional positive effect: the average power density on the surface of the optical components will be reduced significantly. This leads to longer lifetimes of the optical components.

Sounding geometry Independent from the scenario, the most economic sounding geometry is Nadir¹ oriented in order to generate maximum energy density within the laser spot on the surface and to achieve maximum return signals. Target orientations with significant deviation from the vertical orientation relative to the above line-of-sight (LOS) only have to be considered in a near-field scenario, e.g. in the case of a lander or a rover vehicle, sounding towards a tilted surface, e.g. a sloping hillside.

Target characteristics The intensity structure and spectral composition of the backscattered signal will be widely influenced by the structure and composition of the target surface. This includes the effective signal strength directly linked to the Raman scattering coefficient, albedo, composition, roughness, geometric orientation of the soil surface relative to the RRS instrument, orbit height and instrument position. Due to the preliminary status of this study, the RRS simulator only includes a coefficient for the Raman scattering power (inelastic return signal), the albedo (background intensity) as well as the orbit height (distance from the RRS instrument to the target surface). The other parameters are regarded as less dominant and need to be addressed within future study activities.

Raman scattering cross sections and scattering coefficients (theoretical approach) Since the envisaged monitoring scenario is based on object distances that are extremely large compared to conventional laboratory Raman spectroscopy, it is not planned to investigate a small fraction of soil or mineral

¹The point of the celestial sphere directly opposite the zenith and directly below the observer.

surface, representing a few scatter centers. The goal is to monitor a comparably large footprint area and, therefore, also averaging over this area. It is, therefore, necessary to perform a transformation of in-situ Raman scattering cross sections into remote sensing-scale Raman scattering coefficients. The RRS simulator uses an approach that has successfully been applied for numerous atmospheric LIDAR investigations[63]. The microscopic scattering cross-sections were determined within laboratory investigations; however, the differential and absolute Raman scattering cross sections are mainly reported for gases and depend on the polarization of the incident radiation, the angle between incident and observed radiation, and the polarization of the observed radiation. Most values in the literature[24] are given for an angle of 90 degrees between incoming and observed radiation, and linear polarization in the z-direction for both incident and observed radiation, where the incoming radiation typically propagates in the x-direction, and the observed radiation in the y-direction (in a Cartesian coordinate system). This is referred to as the zz scattering cross section. Since for a RRS experiment, different polarizations and angles of observation are involved, corrections have to be employed (Hirschfeld, or the James and Klemperer approach [29, 77, 31]). A simpler approach will be the comparison of measured signal strengths for different materials of interest and the extrapolation of the results to a more complex surface (eg. a mineral mixture). In our estimation, a Raman spectrum of CCl_4 (liquid) and one of anatase (TiO_2 - solid) were measured with the same backscattering configuration. By recording the overall Raman signal from 200 to 1600 cm^{-1} , it was observed that anatase scattered back 290 times more Raman photons than did CCl_4 . Our main concern is not to acquire Raman cross-sections for a solid species but trying to compare the scattering power of a solid surface versus a liquid /gas sample. Therefore, the actual value of the Raman cross-section for anatase is not important. The important parameter is the relative scattering power of a solid versus a gas/liquid sample, since for these samples the intensity of the Raman signal returned to a LIDAR set-up is being measured.

Furthermore, by comparing different minerals, the scattering power of a surface composed of different minerals might be estimated - for example relative to CCl_4 . In our chosen example anatase is 290 times stronger than CCl_4 , potassium feldspar is 1.1 times stronger, magnetite is 0.5 times weaker, and so on. In this way, a quick and rough estimation of the returned Raman signal for a

MINERAL	Artificial microscopic cross sections $/10^{-33} [M^2 \cdot SR^{-1}]$	Artificial macroscopic cross sections $/10^{-12} [M^2 \cdot SR^{-1}]$
K Feldspar	1.93	4.83
Na Feldspar	1.93	4.83
Magnetite	0.97	2.43
Olivine	2.36	5.90
Orthopyroxene	2.3	5.75
Pyrite	3.3	8.25
Quartz	2.5	6.25
Ilmenite	1.93	4.83
Hematite	8.8	22
Apatite	3.5	8.75
Black basaltic rock	0.9	2.25

Table 10.2: Microscopic and macroscopic artificial cross section for Raman scattering.

RRS system - to be used for solid surfaces - can be obtained. These relations are summarized in table 10.2, serving as a first baseline for numerical backscattering cross-sections. It should, however, be stated at this point that these estimations are only a first iteration to achieve information about the orders of magnitude for a RRS link budget. In order to establish more concrete numbers more detailed laboratory work on this topic needs to be done during future phases of RRS development work. The transformation into macroscopic data for remote sensing applications can be made by multiplying these artificial microscopic cross sections with the number of scattering centres per reference area (e.g. $1 m^2$). Regarding the intensity of a Raman backscattering signal at the instrument location, it is assumed that the scattering geometry follows the Lambert cosine law and that the scattering surface is flat and perpendicular to the line-of-sight. This appears to be a realistic approach, since small deviations from the normal orientation create only minor angular-dependent intensity variations. Due to the fact that the Raman scattering process is characterized by a very weak efficiency and due to the relatively large distance from the RRS instrument to the surface being investigated, it will be necessary to operate the instrument at high to extreme high Power Aperture product (PAP) values.

Numerical simulations

The subsequent outputs are based on the numerical RRS simulator, as characterized in the section above. The following scenarios have been studied:

1. from Earth surface towards the Moon
2. from Earth surface towards the Mars
3. from local orbit towards Mars surface
4. from a lander or a rover towards a hillside - near field
5. from a lander or a rover towards a hillside - far field
6. local orbit to asteroid

All these scenarios have significantly different geometrical baselines, resulting in very different link budgets. Table 10.3 depicts some driving factors included in the numerical RRS simulations. The size (diameter and area) of the laser footprint on the target surface is not based on an assumption of 1 mrad divergence angle which is a standard value for current LIDAR (including Raman) systems for atmospheric investigations. This case leads to the whole disk of Mars being illuminated by the laser beam ². A 20 μrad divergence was considered (as used by the McDonald observatory, Austin, Texas for lunar ranging measurements).

10.4 Discussion of Simulator Output

Since this tool offers numerous combinations of input variables, only a selection of outputs is included here. These outputs should not be regarded as binding final data, since ongoing technical and scientific development will also influence these parameters. But at least first rough estimates can be derived from these calculations. The calculations were made for different harmonics of a Nd:YAG laser. The laser pulse energy was considered constant for all wavelengths used in our calculations. The change in the number of photons per pulse and the dependence of the Raman scattering cross-section with the laser wavelength were

²Mean equatorial diameter of Mars is $6.79 \cdot 10^6$ m and the projected area of the planet's disk is $3.62 \cdot 10^{13} m^2$

Scenario (Number)	Earth to Moon (1)	Earth to Mars (2)	Local orbit to Mars (3)	Lander (far field) (4)	Lander (near field) (5)	Local orbit to asteroid (6)
Pulse energy [J]	100	100	100	100	100	100
Divergence angle laser beam [rad]	$2 \cdot 10^{-5}$	$2 \cdot 10^{-5}$	$2 \cdot 10^{-5}$	$2 \cdot 10^{-5}$	$2 \cdot 10^{-5}$	$2 \cdot 10^{-5}$
Distance from target [m]	$3.56 \cdot 10^8$	$5.54 \cdot 10^{10}$	$2.5 \cdot 10^5$	5000	200	10^4
Footprint diameter [m]	7120	$1.1 \cdot 10^6$	5.1	Laser diameter	Laser diameter	0.2
Receiver diameter [m]	10	100	100	3	1	20
Raman photons per laser pulse (average) (1064 nm)	$7.2 \cdot 10^{-7}$	$3 \cdot 10^{-9}$	15	33	228	182

Table 10.3: Summarized output from the RRS simulator (laser wavelength set at 1064 nm)

considered. Table 10.4 summarizes these first estimated link budgets and Figure 10.1 is a graphical comparison of the link budgets for different sounding scenarios and different laser wavelengths. One can easily see that the backscattered signals for an RRS instrument will be very weak, even when assuming high power laser transmitters and large to extremely large receiver optics. Some configurations will most probably need integration over a high number of laser pulses in order to achieve useful SNR figures. This means that a careful instrument analysis and simulation will be necessary in order to determine the real detectability of mineral species.

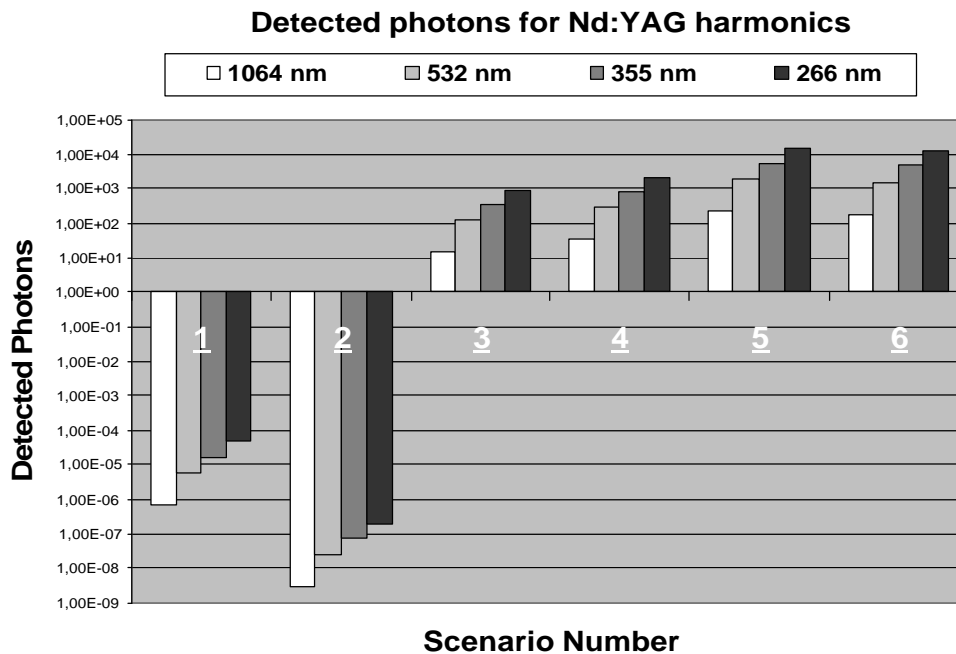


Figure 10.1: Output from the RRS simulator for different harmonics of a Nd:YAG laser and for different scenarios. The scenarios here are noted from 1 to 6 with direct reference to Table 10.3 (page 119) and Table 10.4 (page 121)

10.5 From Laboratory Raman to RRS

In principle, it is possible to perform Raman spectroscopy across distances far beyond the laboratory scale. It is the task of Raman scientists and Remote Sensing specialists to modify the instrument subsystems and their parameters so that

Scenario (Number)	Earth to Moon (1)	Earth to Mars (2)	Local orbit to Mars (3)	Lander (far field) (4)	Lander (near field) (5)	Local orbit to asteroid (6)
	Photons per pulse					
266 nm	$4.72 \cdot 10^{-5}$	$1.95 \cdot 10^{-7}$	956	2150	14900	12000
355 nm	$1.77 \cdot 10^{-5}$	$7.38 \cdot 10^{-8}$	359	807	5600	4480
532 nm	$5.89 \cdot 10^{-6}$	$2.43 \cdot 10^{-8}$	120	269	1870	1490
1064 nm	$7.2 \cdot 10^{-7}$	$3 \cdot 10^{-9}$	15	33	228	182

Table 10.4: Output from the RRS simulator for different harmonics of a Nd:YAG laser and for different scenarios

this new device will meet the requirements for long range RRS sounding. Some subsystems need to be modified radically; especially, the transmitter laser and the receiver optics in order to meet the demanding RRS requirements. A future full-scale RRS instrument will be more or less a gigantic multispectral LIDAR system, characterized by a laser with extreme output power and a receiver telescope with an aperture that is far beyond any current dimensions. The following sections will primarily address technologies and RRS subsystems which - from the present point of view - will need special attention during future development phases. The status of Raman spectroscopy and other technologies at the moment is serving as a base-line for what is needed to meet the requirements of a RRS instrument. It is the very large extrapolation required from laboratory scale towards the envisaged RRS scales that makes it necessary to identify certain technologies as critical ones.

Laser/Transmitter For Remote Raman Spectroscopy, it will be necessary to determine a wavelength suitable for Raman spectroscopy (optimum efficiency for Raman scattering on minerals). Lasers that can be regarded as candidates for future space qualification do exist, detectors and subsequent optics with acceptable characteristics and efficiencies are available or can be made available in the foreseeable future. For a number of reasons, it is advisable to use a pulsed laser for RRS investigations:

- The necessary number of photons is emitted within a very short time; thus increasing the photon density in the case of a fast moving RRS instrument (orbit speed).
- By adjusting the active time gate of the instrument detector it is possible to collect nearly exclusively the backscattered photons from the ground; hence effectively suppressing unwanted background signal (e.g. stellar background) that naturally has CW character. A gate width of 10 ns (typical duration of a Nd:YAG laser) suppresses this background by a factor of 10^8 , based on a pulse repetition frequency of 1 Hz. This approach also suppresses the electronic (thermally induced) noise of the detector itself, since the data acquisition electronics only register detector signals within the established width of the time gate. Reduction factor is the same as above.

- Laser-based Raman spectroscopy can be accompanied by fluorescence interference. In principle, gated signal acquisition could open the possibility to exclude the detection of this fluorescence signal due to its delayed occurrence. Raman scattering occurs almost instantaneously, so that it should be possible to exclusively record the desired Raman signature. Unfortunately the time for fluorescence build-up is only a few nanoseconds, which is about the duration of a pulse from a high power laser. Successful time-gated fluorescence rejection has been demonstrated in a number of laboratory experiments [23]. Here, however, low power lasers with pulses of just a picosecond have been used in order to adjust the time gate around this active window. This instrumental approach cannot be used for an RRS instrument, observing a structured surface since such short time gates would not only reject unwanted fluorescence contributions, but also parts of the surface itself. During a gate of 1 picosecond a laser pulse travels only 0.3 mm. Thus, only a thin slice of the illuminated scenery with a radial extension of just 0.15 mm would be recorded. This is not an applicable observation strategy.

Due to the fact that the distance between the probe (planetary surface) and the RRS instrument itself is extremely great, it is necessary to compensate at least a part of this operational "disadvantage" by a significantly increased average laser power. As a result the transmitter laser for a RRS instrument has to fulfil a number of specific requirements: extremely high pulse energy, short pulse duration, single mode operation, stable spectral operation, high spectral purity, high wall plug efficiency, reliable and long term operation in space. These lasers do not yet exist and power units to operate such a laser with the above-mentioned optical output have not yet been realized. Present activities within the European space industry for ATLID (1-wavelength backscatter LIDAR), WALES (Incoherent Doppler LIDAR) and AEOLUS (6-wavelength water vapour DIAL) will generate reliable experience also in this high power electronics aspect.

Telescope Structure and Primary Optics Recent developments and activities at ESA allow one to estimate whether it will be feasible or not to realize optical structures with apertures of the order of several 100 m^2 . A common ESA / DLR project is aimed at the in-orbit test deployment of a Solar Sail structure

(400 m^2) to be launched in 2005. Another related project is a sailing mission (2500 m^2 ; with a foreseen launch in 2007)[32, 1, 10].

Active Secondary Optics For the RRS receiver optics, an Adaptive Optics (AO) device would be necessary to compensate for surface irregularities of the large-scale primary optics. These perturbations are mainly generated by differential heating and cooling of the large structures as well as by manoeuvre thrusters of the spacecraft. In contrast to terrestrial "anti-turbulence" applications, an AO device aboard a RRS instrument would only have to deal with low to very low frequency corrections, significantly reducing the computational efforts within the AO control loop.

Spectrometer As the received RRS signal will be very weak, the signal losses within the spectrometer must be minimal. An RRS instrument needs a spectrometer with synchronous output across the complete spectral range, since the measurements have to be performed in a minimum amount of time, e.g. on a single pulse basis if possible, and the exact location and structure of the measured Raman spectra are not known prior to their detection.

Detector The detector of a RRS instrument will have to operate at maximum efficiency in order to isolate the optical Raman signal from the electrical background noise. Besides the spectral range, a detector must also be adapted according to its dynamic response (electronic bandwidth). Generally, the bandwidth is inversely proportional to the area of the detector element. For an RRS instrument the bandwidth has to be adapted to the duration of the transmitter laser pulse and to the subsequent pre-amplifier electronics in order to minimize losses within the signal chain which would reduce the number of photons actually registered.

Remote Raman spectroscopy for planetary prospecting will be a demanding technological task. Two well-established scientific "worlds", laboratory Raman spectroscopy and LIDAR technology will have to be brought together in order to realize a high performance RRS instrument. RRS requires the combination of Raman scattering, weak physical interaction for laser remote sensing, with the highest probing distance. Currently, there is no turnkey technology available to

build such an instrument, but a solid basis of key technology that can be used to develop sub-systems for full scale RRS instruments is becoming available.

The work concerning the RRS was performed under the auspices of the European Space Agency, Technical Department, under contract No. 15634/01/NL/LvH and coordinated by Dr. Volker Klein at Kayser-Threde in Munich.

Summary

The present work consist of two major parts. The first part, extending over chapters 1, 2, 3 and 4, addresses the design and construction of a device capable of determining the shell thickness and the core size for monolayer spherical particles in a flow. The second part containing chapters 5, 6, 7, 8, 9 and 10, concentrate on the use of Raman spectroscopy as a space application, namely for use as a tool for *in situ* planetary investigations. This part directly addresses the MIRAS project, a study run under the auspices of Federal Ministry of Education and Research, BMBF and German Aerospace Center, DLR under national registration number 50OW0103. MIRAS stands for "Mineral Investigation by *in situ* Raman Spectroscopy".

Microcapsule Sizing by Elastic Light Scattering

The industrial development of processes based on microcapsules depends on the possibility to provide clear and complete information about the properties of these microcapsules. However, the tools for an easy and efficient determination of the microcapsule properties are lacking, several methods being often required

to describe adequately the microcapsule behavior. Methods for evaluating the individual size and size distribution of both the core and the shell are required together with methods for measuring the mechanical strength, stability in application media, permeability of the shell, etc.

Elastic light scattering measurements provide a possible way of determining properties such as core size, shell size and refractive index. The design and construction of a device capable of measuring the above mentioned parameters for a core-shell particle is the subject of the first part of this thesis.

The basic principle of measurement for the device proposed here consists of analyzing one particle at a time by recording the elastic light scattering pattern at angles between approx. 60° and 120° . By comparing the experimentally recorded phase functions with the previously calculated phase functions stored in a database, the geometry of the scattering object can be identified. In our case the geometry is characterized by two parameters: the shell thickness and the core radius.

In chapter 2 a short overview on the methods used for sizing microparticles is given. Different sizing methods are compared, and the advantages and disadvantages for the general problem of sizing are shortly discussed. It is observed that all sizing methods that are based on elastic light scattering theories are ensemble methods.

Chapter 3 focusses on the theories used for calculating the theoretical scattering patterns with emphasize on the Mie theory. The generalization of Mie theory for layered particles is shortly presented and the far field intensity approximations are discussed.

The last chapter (4) of this first part describes the experimental approach for building an automatic microcapsule sizer. The approach started by O. Sbanski [76] with the development of a software packet for calculating and storing theoretical phase functions for core-shell particles was continued with the designing and construction of a measuring device. The hardware construction and the software with all implemented corrections imposed by the individual setup components are described in detail. For the laser, the monochromaticity, the intensity profile of the beam as well as the planarity of the equi-phase fronts are taken into consideration. The flow cell with three different designs is described, and the influences of the employed design on the light scattering patterns are discussed together

with the optical system used for recording the experimental phase functions. The detection system formed by two identical linear CCD arrays is presented together with the software approach used for data acquisition. Ways of improving the quality and the speed of the analyzing process are discussed. The final section presents measurements run on samples made of homogeneous spheres and also on samples containing industrial microcapsules.

Mineral Investigation by *in situ* Raman Spectroscopy

The envisaged future planetary missions require space-born instruments, which are highly miniaturized with respect to volume and mass and which have low needs of power. A micro Raman spectrometer as a stand alone device on a planetary surface (e.g. Mars) offers a wide spectrum of possibilities. It can assess the chemical analysis via determination of the mineral composition, detect organic molecules in the soil, identify the principal mineral phases, etc. The technical developments in the last years have introduced a new generation of small Raman systems suitable for robotic mineral characterization on planetary surfaces [20, 95]. Two different types of spectrometer were considered for the MIRAS study.

As supporting laboratory experiments for the MIRAS study, the measurements on standard minerals and on SNC Mars meteorites are discussed in chapter 6. The following SNC meteorites have been investigated: Sayh al Uhaymir 060, Dar al Gani 735, Dar al Gani 476, Northwest Africa 856, Los Angeles, Northwest Africa 1068 and Zagami. Pyrite as a hitherto undescribed phase in the picritic (olivine-phyric) shergottite NWA 1068 as well as reduced carbon (e.g. graphite) and anatase in the shergottite Say al Uhaymir 060 are new findings for this class of meteorites.

A detailed description of the proposed designs for MIRAS, with the components used for building the test version on a breadboard is covered in chapter 7. The scientific as well as the mission requirements imposed on the instrument are discussed. The basic design is presented and the main components that are brought together to build the device being the laser unit, the Raman head, the Rayleigh filtering box, and the spectral sensor (spectrometer with a matching detector) are described. The two proposed designs, one based on an acousto-optic tunable filter (AOTF) and the other based on a dispersive hadamard transform

spectrometer are compared to each other. The actual breadboard setup with the detailed description of the components follows in Section 7.3. Further development of a Raman spectrometer for planetary investigations is proposed in combination with a microscope as part of the Extended-MIRAS project.

The software developed for controlling the breadboard version of MIRAS is described in chapter 8 together with a short description of the structure of a relational database used for in house spectra management. The measuring procedures and the data processing steps are presented. Spectra acquired with the MIRAS breadboard version based on the AOTF are shown in chapter 9. The final chapter addresses a rather different possibility of using Raman spectroscopy for planetary investigations. The chapter summarizes the content of four technical notes that were established within the study contracted by the European Space Agency with firma Kayser-Threde in Munich concerning the possibility of applying Raman spectroscopy in the field of remote imaging.

Zusammenfassung

Die vorliegende Arbeit besteht aus zwei Hauptteilen. Der erste Teil, der die Kapitel 1, 2, 3 und 4 umfasst, beschäftigt sich mit dem Design und Aufbau eines Gerätes, welches in der Lage sein sollte, die Schalendichte und die Kerngröße von geschichteten Kugeln in einer Strömung festzustellen.

Der zweite Teil, der aus den Kapiteln 5, 6, 7, 8, 9 und 10 besteht, befasst sich mit der Raman-Spektroskopie als Anwendung in der Raumfahrt, und zwar mit deren Einsatz bei in-situ-planetarischen Erforschungen. Dieser Teil bezieht sich direkt auf das MIRAS-Projekt, eine vom Bundesministerium für Bildung und Forschung (BMBF) und dem Deutschen Zentrum für Luft- und Raumfahrt (DLR) unter der nationalen Eintragsnummer 500W0103 geförderte Studie. MIRAS steht für "Mineral Investigations by *in situ* Raman Spectroscopy".

Größenbestimmung der Mikrokapseln mittels elastischer Lichtstreuung

Der industrielle Fortschritt der auf Mikrokapseln basierenden Prozesse hängt mit der Möglichkeit zusammen, eindeutige und komplette Informationen über die Eigenschaften dieser Mikrokapseln zu liefern. Es gibt allerdings kaum Instrumente

zur schnellen und effizienten Feststellung der Eigenschaften von Mikrokapseln. Zahlreiche Methoden sind häufig notwendig, um das Verhalten von Mikrokapseln ausreichend zu beschreiben. Man braucht Methoden zur Auswertung der individuellen Größe und der Größenverteilung von Kern und Schale sowie zur Messung der mechanischen Eigenschaften, Stabilität in Anwendungsmedien, Schalenpermeabilität usw.

Die Messungen des elastischen Streulichts stellen eine mögliche Methode dar, Eigenschaften wie Kerngröße, Schalengröße und Brechungsindex festzulegen.

Das Design und der Aufbau eines Gerätes, das die obengennanten Parameter für eine Mikrokapsel messen kann, bilden das Thema des ersten Teils dieser Arbeit.

Das grundlegende Messprinzip für das hier vorgeschlagene Gerät besteht in der Analyse einzelner Kapseln, indem das Streuungsmuster des elastischen Lichts bei Winkeln zwischen ca. 60° und 120° aufgezeichnet wird. Werden die experimentell aufgezeichneten Phasenfunktionen mit den vorher berechneten Streuungsmustern in der Datenbank verglichen, so kann die Geometrie des Streuungsobjektes identifiziert werden. In unserem Fall wird die Geometrie durch zwei Parameter gekennzeichnet: die Schalendichte und den Kernradius.

In Kapitel 2 wird ein kurzer Überblick über die Methoden zur Festlegung der Größe von Mikrokapseln gegeben. Es werden verschiedene Methoden miteinander verglichen und Vorteile bzw. Nachteile für das Allgemeinproblem der Größenbestimmung werden kurz angesprochen. Es wird festgestellt, dass alle Methoden, denen die Theorien der elastischen Lichtstreuung zugrundeliegen, "Ensemble-Methoden" sind.

Kapitel 3 beschreibt die Theorien, die oft auf die Berechnung der theoretischen Streuungsmuster angewandt werden, wobei hier die Mie-Theorie im Mittelpunkt steht. Die Erweiterung der Mie-Theorie auf geschichtete Kugeln wird hier kurz geschildert und die Vereinfachungen der Fernfeldstärke werden diskutiert.

Das letzte Kapitel (4) dieses ersten Teils befasst sich mit dem experimentellen Projekt zum Aufbau eines automatischen Mikrokapselanalysators. Das von O. Sbanski [76] begonnene Projekt mit der Entwicklung eines Softwarepakets zur Berechnung und Speicherung von theoretischen Phasenfunktionen für Mikrokapseln wurde mit dem Entwurf bzw. dem Aufbau eines Messgerätes fortgesetzt. Die Hardware und die Software mit allen für die individuellen

Elemente des Aufbaus benötigten Korrekturen werden ausführlich beschrieben. Für den Laser werden Monochromatizität, Strahlstärkeprofil sowie die Planarität von gleichphasigen Wellenfronten berücksichtigt. Die Strömungszelle mit drei verschiedenen Designs wird geschildert. Einflüsse des eingesetzten Entwurfs auf die Eigenschaften der Lichtstreuung sowie das optische, zur Aufzeichnung experimenteller Phasenfunktionen verwendete System werden diskutiert. Das aus zwei identischen linearen CCD-Arrays bestehende Detektionssystem wird zusammen mit der zur Datenaufnahme verwendeten Software präsentiert. Es werden gleichfalls einige Methoden zur Verbesserung der Qualität bzw. Geschwindigkeit des Analyseprozesses angesprochen. Der letzte Teil beschreibt Messungen, welche an homogenen Kugeln sowie industriellen Mikrokapseln durchgeführt wurden.

MIRAS - "Mineral Investigation by *in situ* Raman Spectroscopy"

Die für die Zukunft vorausgesehenen planetarischen Missionen benötigen Instrumente, die in Bezug auf Volumen und Gewicht extrem stark miniaturisiert sind und wenig Energie brauchen. Ein Mikro-Ramanspektrometer als allein operierendes Gerät auf der planetarischen Oberfläche (z.B. Mars) bietet ein breites Spektrum von Möglichkeiten an. Es kann die chemische Analyse durch Festlegung der mineralischen Zusammensetzung auswerten, organische Moleküle im Boden ausweisen, die mineralischen Hauptphasen identifizieren usw. Die technischen Entwicklungen der letzten Jahre haben eine neue Generation kleiner Raman-systeme mit sich gebracht, welche für die mineralische Charakterisierung von planetarischen Oberflächen geeignet sind. Für die MIRAS-Studie wurden zwei verschiedene Typen von Spektrometern berücksichtigt.

In Kapitel 6 werden die Messungen von Standardmineralien und SNC-Marsmeteoriten als unterstützende Laborexperimente behandelt. Folgende SNC-Meteorite sind untersucht worden: Sayh al Uhaymir 060, Dar al Gani 735, Dar al Gani 476, Northwest Africa 856, Los Angeles, Northwest Africa 1068 und Zagami. Pyrit als eine bis jetzt unbeschriebene Phase in dem Picritic (Olivin-Phyric) Shergottit NWA 1068 sowie reduzierter Kohlenstoff (z.B. Graphit) und Anatase in dem Shergottit Say al Uhaymir 060 sind neue Erkenntnisse für diese Meteoritenklasse.

Eine detaillierte Beschreibung der vorgeschlagenen Entwürfe für MIRAS mit

den Bauteilen, die zum Aufbau der Testversion eines Breadboard verwendet wurden, wird in Kapitel 7 geliefert. Es werden sowohl die wissenschaftlichen als auch die Missionsanforderungen an das Gerät diskutiert. Der Grundentwurf wird vorgeführt, wobei die einzelnen Hauptbauteile des Gerätes die Lasereinheit, den Ramankopf, das Rayleigh-Filtersystem und das Spektrometer (mit einem passenden Detektor) darstellen. Die zwei vorgeschlagenen Entwürfe, der eine basierend auf einem akusto-optisch einstellbaren Filter (AOTF), der andere hingegen auf einem dispersiven Hadamard-Transformationsspektrometer werden miteinander verglichen. Der tatsächliche Breadboard-Aufbau sowie eine detaillierte Beschreibung der Bauteile folgen in Unterkapitel 7.3. Es wird ein weiteres Entwicklungskonzept für ein Raman-Spektrometer in Bezug auf planetarische Untersuchungen, im Zusammenhang mit einem Mikroskop als Teil des erweiterten MIRAS-Projektes, vorgeschlagen.

Das für die Kontrolle der MIRAS Breadboard-Version entwickelte Programm samt der Struktur einer zum internen Spektrummanagement verwendeten relationalen Datenbank werden in Kapitel 8 vorgestellt. Die Messprozeduren und die Datenbearbeitungsvorgänge werden zusammen beschrieben. Die mit der auf AOTF basierenden MIRAS Breadboard-Version aufgenommenen Spektren sind in Kapitel 9 abgebildet. Das letzte Kapitel (10) bezieht sich auf eine etwas andere Möglichkeit, Raman-Spektroskopie bei planetarischen Untersuchungen anzuwenden. Das Kapitel fasst den Inhalt von vier technischen Beobachtungen zusammen, welche im Rahmen der von der Firma Kayser Threde in München für die European Space Agency ausgeschriebenen Studie aufgezeichnet wurden. Diese Studie befasst sich mit der Möglichkeit, Raman-Spektroskopie auf das Gebiet der Fernaufnahmen anzuwenden.

Appendix A

Equation Repository

Maxwell equations

$$\nabla \cdot \vec{D} = \rho, \tag{A.1}$$

$$\nabla \cdot \vec{B} = 0, \tag{A.2}$$

$$\nabla \times \vec{E} = -\frac{\partial \vec{B}}{\partial t}, \tag{A.3}$$

$$\nabla \times \vec{H} = \vec{J} + \frac{\partial \vec{D}}{\partial t}. \tag{A.4}$$

Size parameter x

$$x = \frac{2\pi a}{\lambda} \quad \text{where } a \text{ - sphere radius} \tag{A.5}$$

and λ - light wavelength (inside the propagating medium)

Wave equation in spherical coordinates

By switching from the cartesian coordinates (x, y, z) to spherical coordinates (θ, ϕ, r) :

$$x = r \sin(\theta) \cos(\phi), \quad (\text{A.6})$$

$$y = r \sin(\theta) \sin(\phi), \quad (\text{A.7})$$

$$z = r \cos(\theta), \quad (\text{A.8})$$

the Helmholtz equation

$$\Delta\psi + k^2\psi = 0, \quad (\text{A.9})$$

will transform in:

$$\frac{1}{r^2} \frac{\partial}{\partial r} \left(r^2 \frac{\partial \psi}{\partial r} \right) + \frac{1}{r^2 \sin \theta} \frac{\partial}{\partial \theta} \left(\sin \theta \frac{\partial \psi}{\partial \theta} \right) + \frac{1}{r^2 \sin^2 \theta} \frac{\partial^2 \psi}{\partial \phi^2} + k^2 \psi = 0. \quad (\text{A.10})$$

The scalar function $\psi(r, \theta, \phi)$ can be expressed as a product [11]:

$$\psi(r, \theta, \phi) = f_1(r) \cdot f_2(\theta) \cdot f_3(\phi), \quad (\text{A.11})$$

which by substitution in eq. A.10 leads to:

$$\frac{d^2 f_3}{d\phi^2} + \ell^2 f_3 = 0, \quad (\text{A.12})$$

$$\frac{1}{\sin \theta} \frac{d}{d\theta} \left(\sin \theta \frac{df_2}{d\theta} \right) + \left[n(n+1) - \frac{\ell^2}{\sin^2 \theta} \right] f_2 = 0, \quad (\text{A.13})$$

$$\frac{d}{dr} \left(r^2 \frac{df_1}{dr} \right) + [k^2 r^2 - n(n+1)] f_1 = 0, \quad (\text{A.14})$$

where n and l are constants which have to be determined. For eq. A.12 the two independent solutions are:

$$f_{3,e}(\phi) = \cos l\phi, \quad \text{and} \quad f_{3,o}(\phi) = \sin l\phi, \quad (\text{A.15})$$

where o stays for *odd* and e for *even*. Since the solutions in ϕ have to be periodic with a 2π period follows that l has to be an integer.

For eq. A.13 the solutions are the Legendre polynomials [35] $P_n^\ell(\cos \theta)$ with $n = 0, 1, 2, \dots$ and $\ell = 0, 1, \dots, n$.

For eq. A.14 the solutions are the Bessel spherical function of first (j_n) and second (y_n) order (notation $\rho = kr$):

$$j_n(\rho) = \sqrt{\frac{\pi}{2\rho}} J_{n+1/2}(\rho), \quad (\text{A.16})$$

$$y_n(\rho) = \sqrt{\frac{\pi}{2\rho}} Y_{n+1/2}(\rho). \quad (\text{A.17})$$

Every linear combination of j_n and y_n is also a solution, therefore

$$h_n^{(1)} = j_n(\rho) + iy_n(\rho), \quad (\text{A.18})$$

$$h_n^{(2)} = j_n(\rho) - iy_n(\rho). \quad (\text{A.19})$$

are also solutions (Bessel spherical functions of third order).

Therefore the solution for eq. A.10 is:

$$\psi_{e\ell n}(r, \theta, \phi) = z_n(\rho) P_n^\ell(\cos \theta) \begin{pmatrix} \cos(\ell\phi) \\ \sin(\ell\phi) \end{pmatrix}, \quad (\text{A.20})$$

where z_n stays for one of the Bessel spherical function.

The solutions for the vectorial wave equation (see eq. 3.1, 3.2) will be then:

$$\vec{M}_{e\ell n} = \begin{pmatrix} 0 \\ \frac{\ell}{\sin \theta} P_n^\ell(\cos \theta) z_n(\rho) \frac{-\sin \ell\phi}{\cos \ell\phi} \\ -\frac{dP_n^\ell(\cos \theta)}{d\theta} z_n(\rho) \frac{\cos \ell\phi}{\sin \ell\phi} \end{pmatrix}, \quad (\text{A.21})$$

$$\vec{N}_{e\ell n} = \begin{pmatrix} n(n+1) P_n^\ell(\cos \theta) \frac{z_n(\rho)}{\rho} \frac{\cos \ell\phi}{\sin \ell\phi} \\ \frac{dP_n^\ell(\cos \theta)}{d\theta} \frac{1}{\rho} \frac{d}{d\rho} [\rho z_n(\rho)] \frac{\cos \ell\phi}{\sin \ell\phi} \\ \frac{\ell}{\sin \theta} P_n^\ell(\cos \theta) \frac{1}{\rho} \frac{d}{d\rho} [\rho z_n(\rho)] \frac{-\sin \ell\phi}{\cos \ell\phi} \end{pmatrix}. \quad (\text{A.22})$$

These are known as vectorial spherical harmonic functions. l is the mode order and n is the mode number. The mode order (l) actually gives the number of maxima in the radial dependence. The mode number (n) gives the number of maxima in the angular dependence between 0 and 180 degrees. The mode number also specifies the order of the Bessel function that constitute the radial part of the MDR.

Angular Functions π_n and τ_n

$$\pi_n = \frac{P_n^{\ell=1}(\cos \theta)}{\sin \theta}, \quad (\text{A.23})$$

$$\tau_n = \frac{dP_n^{\ell=1}(\cos \theta)}{d\theta}. \quad (\text{A.24})$$

Are defined using the Legendre polynoms with $l = 1$.

Appendix B

Microparticle Analyzer Device - Setup Images

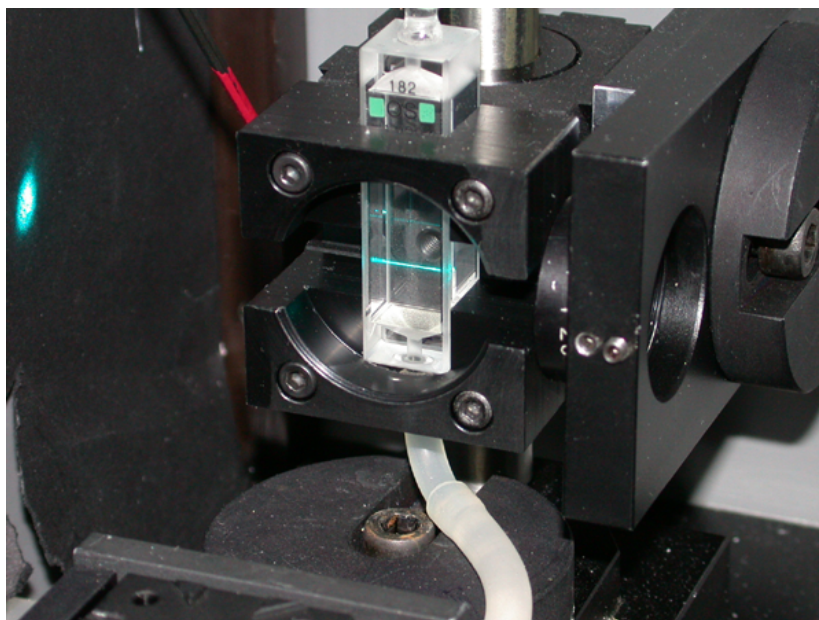


Figure B.1: Flow trough cell with the laser path.

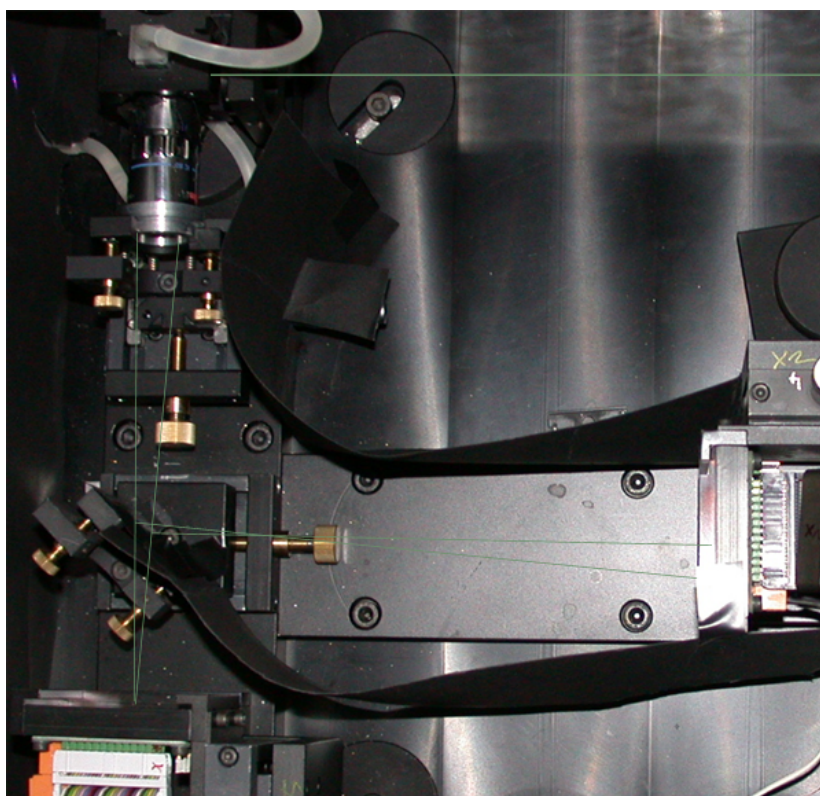


Figure B.2: Complete setup with the schematic ray path depicted

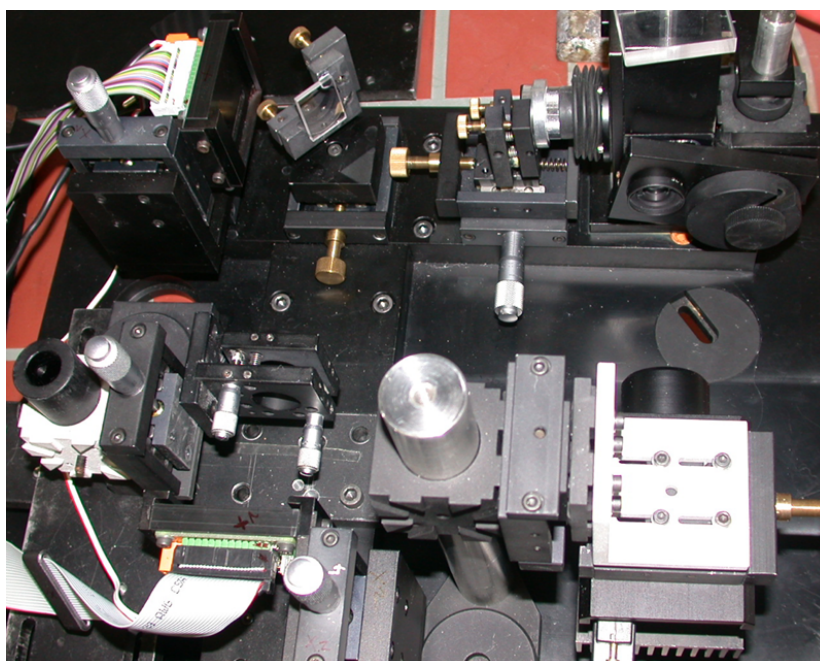


Figure B.3: Complete setup with the flow cell having the collecting optics inside

Appendix C

MIRAS - Breadboard Images

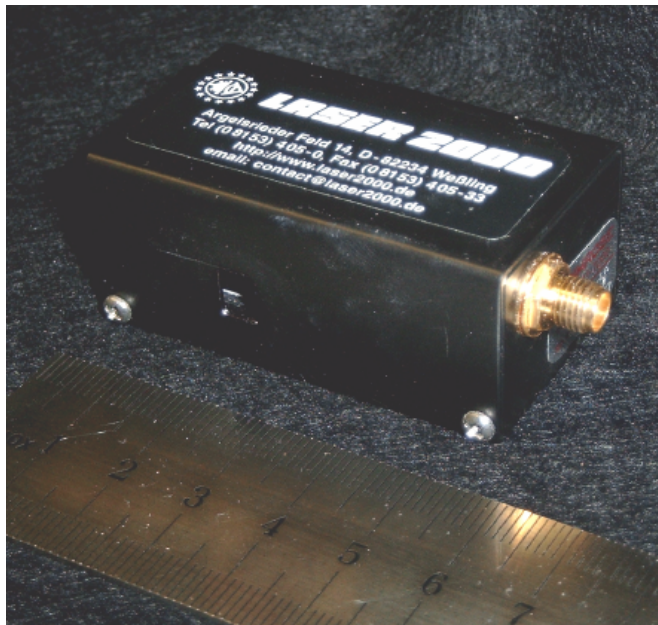


Figure C.1: Acousto-Optic Tunable Filter. Dimensions 50 x 30 x 35 mm and a mass of 85 g

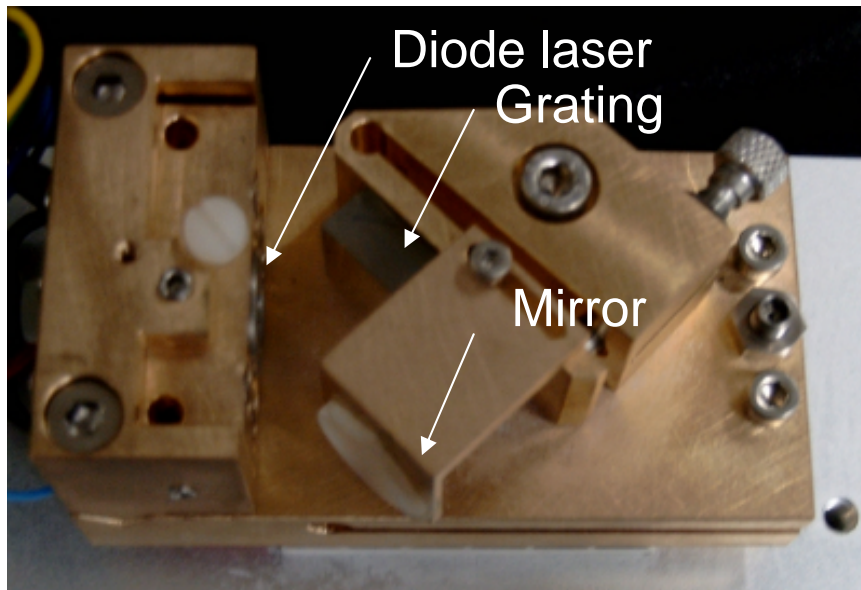


Figure C.2: The External-Cavity-Diode Laser in Littrow configuration. The size is of approx. 8x4 cm.



Figure C.3: The APD based SPCM-AQR-15 photon counter module



Figure C.4: MIRAS Breadboard assembled at Kayser Threde GmbH - Munich

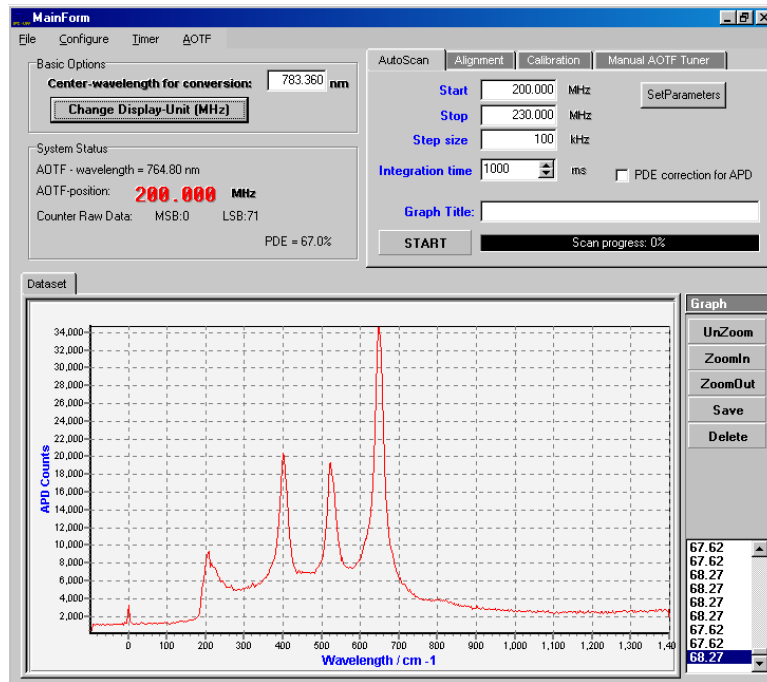


Figure C.5: User interface view for the MIRAS instrument control software

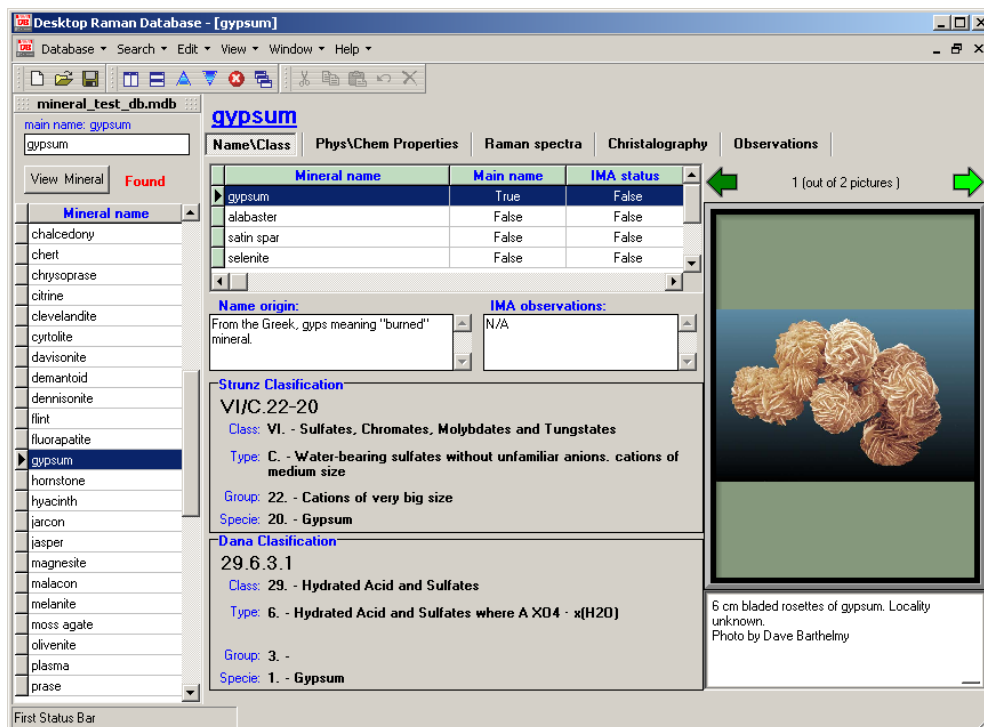


Figure C.6: MIRAS - supporting database: user interface - mineral classification

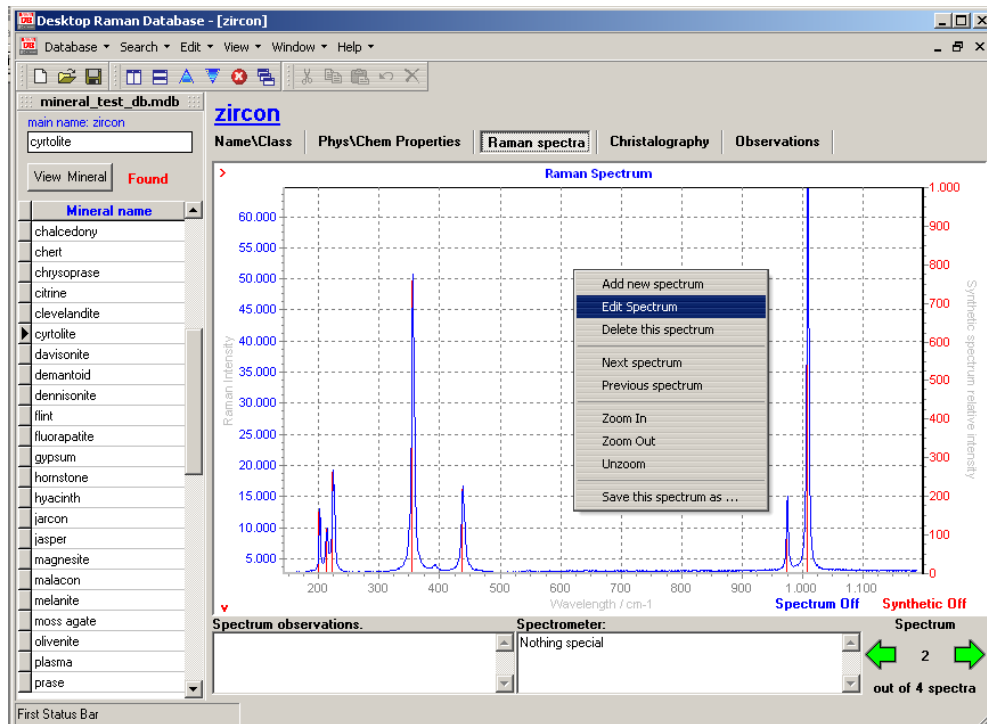


Figure C.7: MIRAS - supporting database: user interface - raman spectra

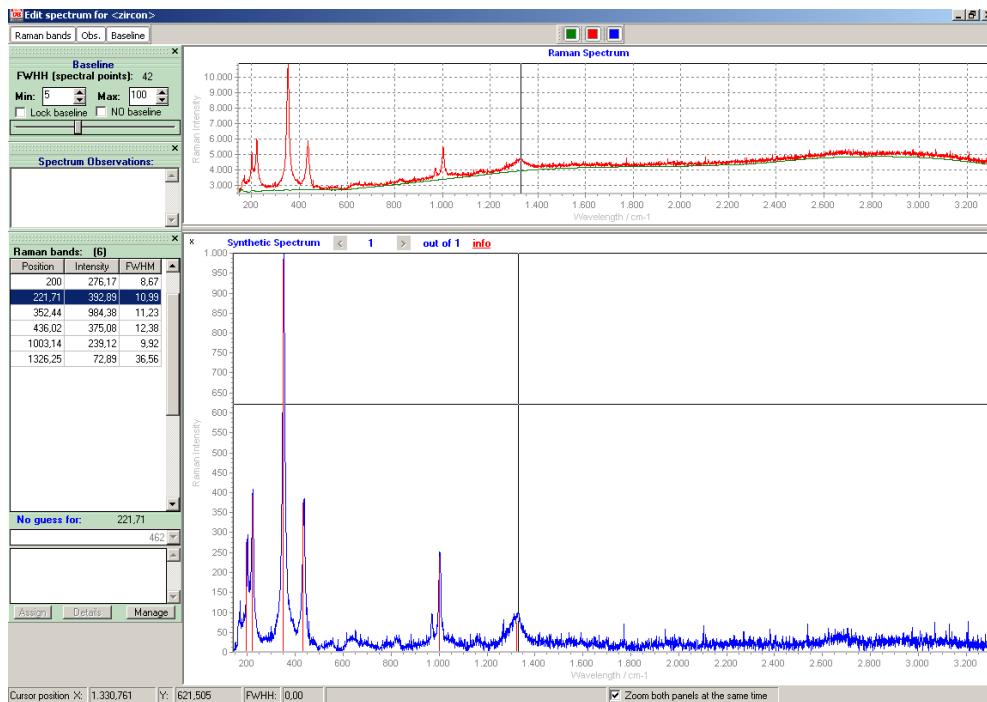


Figure C.8: MIRAS - supporting database: user interface - edit raman information

Bibliography

- [1] Ultralight Structures and Space Observatories. Technical report, NASA SBIR 1999 Program. Cited at pag. 124
- [2] M. A. G. Abushagur and N. George. Polarization and wavelength effects on the scattering from dielectric cylinders. *Appl. Opt.*, 24:4141–4145, 1985. Cited at pag. 2, 21
- [3] A. L. Aden and M. Kerker. Scattering of electromagnetic waves from two concentric spheres. *J. Appl. Phys.*, 22:1242–1246, 1951. Cited at pag. 2, 18, 20, 25
- [4] A. J. Adey. Scattering of electromagnetic waves by coaxial cylinders. *Can. J. Phys.*, 34:510–520, 1956. Cited at pag. 2, 21
- [5] Sh. Asano. Light scattering by horizontally oriented spheroidal particles. *Appl. Opt.*, 22:1390–1396, 1983. Cited at pag. 2, 21
- [6] M. Bailey. An overview of particle size analysis. *Journal of the Adhesive and Sealant Council*, pages 263–269, March 1997. Cited at pag. 10
- [7] P. W. Barber and C. Yeh. Scattering of electromagnetic waves by arbitrarily shaped dielectric bodies. *Appl. Opt.*, 14:2864–2872, 1975. Cited at pag. 21
- [8] R. H. T. Bates, J. R. James, I. N. L. Callet, and R. F. Miller. An overview of point matching. *Radio Elect. Eng.*, 43:197–210, 1973. Cited at pag. 21

- [9] B. W. Bell and W. S. Bickel. Single fiber light scattering matrix: an experimental determination. *Appl. Opt.*, 20:3874–3879, 1981. Cited at pag. 2, 21
- [10] K. Belvin. *Ultra-Lightweight Structures Technology for Space Solar Power*, 2002. Cited at pag. 124
- [11] C. Bohren and D. Huffman. *Absorption and scattering of light by small particles*. J. Wiley & Sons, New York, 1983. Cited at pag. 21, 23, 29, 136
- [12] C. F. Bohren. Light scattering by an optically active sphere. *Chem. Phys. Lett.*, 29:458–462, 1974. Cited at pag. 20
- [13] C. F. Bohren and Sh. B. Singham. Backscattering by nonspherical particles: a review of methods and suggested new applications. *J. Geophys. Res.*, 96:5269–5277, 1991. Cited at pag. 21
- [14] M. Bouchard and D.C. Smith. Catalogue of 45 reference Raman spectra of minerals concerning research in art history or archaeology, especially on corroded metals and coloured glass. *Spectrochimica Acta Part A*, 59:2247–2266, 2003. Cited at pag. 68
- [15] A. Brunsting and P. F. Mullaney. Light scattering from coated spheres: model for biological cells. *J. Appl. Opt.*, 11:675–680, 1972. Cited at pag. 25
- [16] H. Y. Chen, M. F. Iskander, and J. E. Penner. Light scattering and absorption by fractal agglomerates and coagulations of smoke aerosols. *J. Mod. Opt.*, 37:171–181, 1990. Cited at pag. 21
- [17] T. F. Cooney, E. R. D. Scott, A. N. Krot, S. K. Sharma, and A. Yamaguchi. Vibrational spectroscopic study of minerals in the Martian meteorite ALH84001. *American Mineralogist*, 84(10):1569–1576, 1999. Cited at pag. 66
- [18] B. M. Cullum, J. Mobely, Z. Chi, D. L. Stokes, G. H. Miller, and T. Vo-Dinh. Development of a compact, handheld Raman instrument with no moving parts for use in field analysis. *Review of Scientific Instruments*, 71(4):1602–1607, 2000. Cited at pag. 84
- [19] Peter Debye. Der Lichtdruck auf Kugeln von beliebigem Material. *Ann. Phys.*, 30:57–136, 1909. Cited at pag. 20, 22
- [20] D. L. Dickensheets, D. D. Wynn-Williams, H. G. M. Edwards, C. Schoen, C. Crowder, and E. M. Newton. A novel miniature confocal microscope/Raman spectrometer system for biomolecular analysis on future Mars

- missions after Antarctic trials. *Journal of Raman Spectroscopy*, 31(7):633–635, 2000. Cited at pag. 79, 110, 129
- [21] H. G. M. Edwards, D. W. Farwell, M. M. Grady, D. D. Wynn-Williams, and I. P. Wright. Comparative Raman microscopy of a Martian meteorite and Antarctic lithic analogues. *Planet. Space Sci.*, 47(3/4):353–362, 1999. Cited at pag. 66
- [22] L. B. Evans. Scattering of electromagnetic radiation by infinitely long, hollow, and coated cylinders. *J. Opt. Soc. Am.*, 54:1004–1007, 1964. Cited at pag. 2, 21
- [23] N. Everall, T. Hahn, P. Matousek, A. W. Parker, and M. Towrie. Picosecond Time-Resolved Raman Spectroscopy of Solids: Capabilities and Limitations for Fluorescence Rejection and the Influence of Diffuse Reflectance. *Applied Spectroscopy*, 55(12):1701–1708, 2001. Cited at pag. 123
- [24] G. W. Faris and R. A. Copeland. *Applied Optics*, 36(12):2684–2685, 1997. Cited at pag. 116
- [25] B. Gasharova, B. Mihailova, and L. Konstantinov. Raman spectra of various types of tourmaline. *European Journal of Mineralogy*, 9(5):935–940, 1997. Cited at pag. 66
- [26] G. Grehan, B. Maheu, and Gouesbet G. Scattering of laser beams by Mie scatter centers: numerical results using a localized approximation. *Appl. Opt.*, 25:3539–3548, 1986. Cited at pag. 20
- [27] W.P. Griffith. *Spectroscopy of Inorganic-Based Materials*. Wiley, New York, 1987. Cited at pag. 68
- [28] N. Gupta and R. Dahmani. AOTF Raman spectrometer for remote detection of explosives. *Spectrochimica Acta Part A*, 56:1453–1456, 2000. Cited at pag. 84
- [29] T. Hirschfeld. Correction of Raman Cross Section from Laboratory to Remote Spectrometer Geometries. *Applied Spectroscopy*, 27(5), 1973. Cited at pag. 116
- [30] R. Hochleitner, N. Tarcea, G. Simon, W. Kiefer, and J. Popp. Micro Raman Spectroscopy - a valuable tool for the investigation of extraterrestrial material. Accepted for publication in *Journal of Raman Spectroscopy* vol. 35, 2004. Cited at pag. 70
- [31] T. C. James and W. Klemperer. Line Intensities in the Raman Effect of 1.SIGMA. Diatomic Molecules. *J. Chem. Phys.*, 31(13):130–134, 1959. Cited at pag. 116

- [32] C. H. M. Jenkins. *Gossamer Spacecraft: Membrane and Inflatable Structures Technology for Space Applications*, volume 191 of *Progress in Astronautics and Aeronautics*. AIAA, Virginia. Cited at pag. 124
- [33] T. Kaiser and G. Schweiger. Stable algorithm for the computation of Mie-coefficients for scattered and transmitted fields of a coated sphere. *J. Comp. Phys.*, 7:682–686, 1993. Cited at pag. 49
- [34] G. W. Kattawar, Ch. R. Hu, M. E. Parkin, and P. Herb. Mueller matrix calculations for dielectric cubes: comparison with experiments. *Appl. Opt.*, 26:4174–4180, 1987. Cited at pag. 21
- [35] M. Kerker. *The scattering light and other electromagnetic radiation*. New York: Academic Press, 1969. Cited at pag. 2, 18, 20, 21, 25, 136
- [36] M. Kerker, L.H. Kaufman, and W.A. Farone. Scattering of electromagnetic waves from two concentric spheres when the outer shell has a variable refractive index. Numerical results. *J. Opt. Soc. Am.*, 56:1053–1056, 1966. Cited at pag. 2, 18, 20, 25
- [37] M. Kerker, J.P. Kratochvil, and E. Matijevic. Light scattering functions for concentric spheres. Total scattering coefficients $m_1 = 2.1050$, $m_2 = 1.4821$. *J. Opt. Soc. Am.*, 52:551–561, 1962. Cited at pag. 2, 18, 20, 23, 25
- [38] M. Kerker and E. Matijevic. Scattering of electromagnetic waves from concentric infinite cylinders. *J. Opt. Soc. Am.*, 51:506–508, 1961. Cited at pag. 2, 21
- [39] M. Kerker, D.-S. Wang, and C.L. Giles. Electromagnetic scattering by magnetic spheres. *J. Opt. Soc. Am.*, 73:765–767, 1983. Cited at pag. 2, 20
- [40] W. Kiefer. *Advances in Infrared and Raman Spectroscopy*, volume 3, chapter Recent Techniques in Raman Spectroscopy. 1977. Cited at pag. 2
- [41] B. A. Kolesov and C. A. Geiger. Raman spectra of silicate garnets. *Physics and Chemistry of Minerals*, 25(2):142–151, 1998. Cited at pag. 66
- [42] D. A. Ksienski and T. B. A. Senior. Scattering by small thin dielectric particles. *Appl. Opt.*, 38:225–231, 1985. Cited at pag. 21
- [43] A. Lakhtakia. General theory of the Purcell-Pennypacker scattering approach and its extension to bianisotropic scatterers. *Astrophys. J.*, 394:494–499, 1992. Cited at pag. 21
- [44] G. Landsberg and L. Mandelstam. A novel effect of light scattering in crystals. *Naturwissenschaften*, 16:557, 1928. Cited at pag. 2

-
- [45] P. Latimer. Light scattering by ellipsoids. *J. Colloid Sci.*, 53:102–109, 1975. Cited at pag. 21
- [46] P. Latimer. Predicted scattering by spheroids: comparison of approximate and exact methods. *Photochem. Photobiol.*, 19:3039–3041, 1980. Cited at pag. 2, 21
- [47] A. C. Lind. Electromagnetic scattering by obliquely oriented cylinders. *J. Appl. Phys.*, 37:3195–3203, 1966. Cited at pag. 2, 21
- [48] L.-G. Liu, T. P. Merenagh, and T. Irifune. Raman spectra of MgSiO₃:10% Al₂O₃-perovskite at various pressures and temperatures. *Phys. Chem. Miner.*, 22(8):511–516, 1995. Cited at pag. 66
- [49] J. A. Lock. Improved Gaussian beam-scattering algorithm. *Appl. Opt.*, 22:1684–1687, 1983. Cited at pag. 40
- [50] A. E. H. Love. The scattering of electric waves by a dielectric sphere. *Proc. London Math. Soc.*, 30:308–321, 1899. Cited at pag. 22
- [51] B. Maheu, G. Grehan, and G. Gouesbet. Generalized Lorenz-Mie theory: first exact values and comparisons with the localized approximation. *Appl. Opt.*, 26:23–25, 1987. Cited at pag. 20
- [52] Gustav Mie. Beiträge zur Optik trüber Medien, speziell kolloidaler Metallösungen. *Ann. Phys.*, 25:377–445, 1908. Cited at pag. 2, 20, 22
- [53] J. J. Mikulski and E. L. Murphy. The computation of electromagnetic scattering from concentric spherical structures. *IEEE Trans. Anten. Propag.*, AP-11:169–177, 1963. Cited at pag. 25
- [54] M. I. Mishchenko. Light scattering by size-shape distributions of randomly oriented axially symmetric particles of a size comparable to a wavelength. *Appl. Opt.*, 32:4652–4666, 1993. Cited at pag. 2, 18, 20
- [55] M. I. Mishchenko, L. D. Travis, and D. W. Mackowski. T-matrix computations of light scattering by nonspherical particles: A review. *J. Quant. Spectro. Radiative Transfer*, 55:535–575, 1996. Cited at pag. 21, 31
- [56] R. H. Morris, C. C. Hoyt, and P. J. Treado. Imaging spectrometers for fluorescence and Raman microscopy: Acousto-Optic and Liquid Crystal Tunable Filters. *Applied Spectroscopy*, 48:857–865, 1994. Cited at pag. 84, 105
- [57] B. W. Muller and R. H. Muller. Particle size analysis of latex suspensions and microemulsions by photon correlation spectroscopy. *Journal of pharmaceutical sciences*, 73:915, 1984. Cited at pag. 11
-

- [58] M. Peng, H. K. Mao, D. Li, and E. C. T. Chao. Raman spectroscopy of garnet-group minerals. *Chinese Journal of Geochemistry*, 13(2):176–183, 1994. Cited at pag. 66
- [59] S. Petit, J.-L. Robert, A. Decarreau, G. Besson, O. Grauby, and F. Martin. Contribution of spectroscopic methods to 2: 1 clay characterization. *Bulletin des Centres de Recherches Exploration-Production Elf-Aquitaine*, 19(1):119–147, 1995. Cited at pag. 66
- [60] A. J. Poggio and E. K. Miller. *Computer Techniques for Electromagnetics*, chapter Integral equation solutions of three-dimensional scattering problems, pages 159–264. Oxford, 1973. Cited at pag. 21
- [61] J. Popp, N. Tarcea, W. Kiefer, M. Hilchenbach, N. Thomas, T. Stuffer, S. Hofer, D. Stoffler, and A. Greshake. The effect of surface texture on the mineralogical analysis of chondritic meteorites using Raman spectroscopy. *Planetary and Space Science*, 50:865–870, 2002. Cited at pag. 79
- [62] J. Popp, N. Thomas, C. Cockell, H.G.M. Edwards, J. Gomez-Elvira, M. Hilchenbach, R. Hochleitner, S. Hofer, V. Hoffmann, B. Hofmann, E.K. Jessberger, W. Kiefer, J. Martinez-Frias, S. Maurice, F. Rull-Pérez, M. Schmitt, G. Simon, F. Sobron, N. Tarcea, W. Weigand, J.A. Whitby, and P. Wurz. Extended-MIRAS: an instrumental approach for the search for traces of extinct and extant life on Mars. In *Geophys. Research Abstracts*. EGS, 2004. Cited at pag. 93
- [63] V. E. Privalov and V. G. Shemanin. Proceedings of SPIE-The International Society for Optical Engineering 2002. In *Laser for Measurement and Information Transfer*, volume 4680, pages 106–111, 2002. Cited at pag. 116
- [64] T. Provder and Dwight P. Overview of particle size distribution characterization methods. *Proceedings of the Water-Borne and Higher-Solids Coatings Symposium*, 14:1–5, 1987. Cited at pag. 10
- [65] E. M. Purcell and C. R. Pennypacker. Scattering and absorption of light by non-spherical dielectric grains. *Astrophys. J.*, 186:705–714, 1973. Cited at pag. 21
- [66] C. V. Raman and K. S. Krishan. A new type of secondary radiation. *Nature*, 121:501, 1928. Cited at pag. 2
- [67] D. W. Rayleigh. On the electromagnetic theory of light. *Phil. Mag.*, 12:81–101, 1881. Cited at pag. 2, 21
- [68] D. W. Rayleigh. On the dispersion of light by a dielectric cylinder. *Phil. Mag.*, 36:365–376, 1918. Cited at pag. 2, 21

-
- [69] L. Richter, P. Costeb, V. V. Gromovc, H. Kochana, R. Nadalinid, T. C. Nge, S. Pinnaf, H. E. Richtera, and K. L. Yungg. Development and testing of subsurface sampling devices for the Beagle 2 lander. *Planetary and Space Science*, 50(9):903–913, 2002. Cited at pag. 83
- [70] R. Rieder, T. Economu, H. Waenke, A. Turkevich, J. Crisp, J. Brueckner, G. Dreibus, and H. Y. McSween. The chemical composition of Martian soil and rocks returned by the mobile alpha proton X-ray spectrometer: preliminary results from the X-ray mode. *Science*, 278:1771–1774, 1997. Cited at pag. 61, 62
- [71] R. Riesenbergr and J. Lonschinski. HADAMARD-Minispectrometer made by a Micro Device. In *Proceedings of 3rd Round Table on Micro/ Nano Technologies for Space*, pages 291–297. ESTEC, Noordwijk, The Netherlands, 2000. Cited at pag. 84
- [72] R. Riesenbergr, K. Mack, and T. Seifert. Eine neue Generation von Spektrolsensoren, 2000. VDI Berichte 1530, Sensoren und Messsysteme 2000, S. 231-235. Cited at pag. 84
- [73] R. Riesenbergr, G. Nitzsche, A. Wuttig, and B. Harnisch. *Smaller Satellites: Bigger Business*, chapter Micro Spectrometer and MEMS for Space, pages 403–406. Kluwer Academic Publisher, 2002. Cited at pag. 83, 84
- [74] A. E. Rubin. Mineralogy of meteorite groups. *Meteoritics and Planetary Science*, 32(2):231–247, 1997. Cited at pag. 72
- [75] A. E. Rubin. Mineralogy of meteorite groups. *Meteoritics and Planetary Science*, 32:733–734, 1997. Cited at pag. 72
- [76] O. Sbanski. *Simulation des elastischen und inelastischen Streulichts von sphärischen homogenen und geschichteten Mikropartikeln*. PhD thesis, Institut für Physikalische Chemie: Universität Würzburg, 2001. Cited at pag. 8, 18, 49, 128, 132
- [77] H. W. Schroetter and H. W. Kloeckner. *Raman Spectroscopy of Gases and Liquids*, chapter Raman Scattering Cross Sections in Gases and Liquids. Springer Verlag, 1979. Cited at pag. 116
- [78] D. W. Schuerman, R. T. Wang, B. A. S. Gustafson, and R. W. Scafer. Systematic studies of light scattering. 1: Particle shape. *Appl. Opt.*, 20:4039–4050, 1981. Cited at pag. 2, 21
- [79] S. K. Sharma, S. M. Angel, M. Ghosh, H. W. Hubble, and P. G. Lucey. Remote pulsed laser Raman spectroscopy system for mineral analysis on planetary surfaces to 66 meters. *Applied Spectroscopy*, 56(6):699–705, 2002. Cited at pag. 79, 110
-

- [80] S. K. Sharma, T. F. Cooney, and S. Y. Wang. Effect of high P and high T on olivines - a Raman spectral study. In *Recent Trends High Pressure Res.*, Proc. 13th AIRAPT Int. Conf. High Pressure Sci. Technol., pages 614–619, 1992. Cited at pag. 66
- [81] K. S. Shifrin. Rasseyanie sveta na dvuhslojnyh chastitsah. *Izv. AN SSSR, ser. Geofiz.*, N2:15–21, 1952. Cited at pag. 23, 25
- [82] K. S. Shifrin and I. G. Zolotov. Remark about the notation used for calculating the electromagnetic field scattered by a spherical particle. *Appl. Opt.*, 32(27):5397–5398, 1993. Cited at pag. 23
- [83] D. W. Shortt, D. Roessener, and P. J. Wyatt. Absolute measurement of diameter distributions of particles using a multiangle scattering photometer coupled with flow field-flow fractionation. *American Laboratory*, pages 21–28, 1996. Cited at pag. 14
- [84] A. Smekal. The quantum theory of dispersion. *Naturwissenschaften*, 11:873, 1923. Cited at pag. 2
- [85] M. C. Storrie-Lombardi, A. I. Tsapin, G. D. McDonald, H. Sun, and K. H. Nealson. Ultraviolet raman spectroscopy for in situ geobiological exploration of Mars. In *Book of Abstracts, 217th ACS National Meeting, Anaheim, Calif., March 21-25*, volume GEOC-069. American Chemical Society, Washington, D. C, 1999. Cited at pag. 79
- [86] S. Stroem. On the integral equations for electromagnetic scattering. *Am. J. Phys.*, 43:1060–1069, 1975. Cited at pag. 21
- [87] N. Tarcea, J. Popp, M. Schmitt, W. Kiefer, T. Stuffer, S. Hofer, E. Schmidt, G. Simon, R. Hochleitner, and M. Hilchenbach. MIRAS: present status and further possible developments. In *Geophys. Research Abstracts*, volume 5:12030. EGS, 2003. Cited at pag. 79
- [88] N. Tarcea, J. Popp, M. Schmitt, W. Kiefer, T. Stuffer, S. Hofer, G. Simon, R. Hochleitner, B. A. Hoffmann, and M. Hilchenbach. Raman imaging on minerals: global versus point sampling techniques. In *Geophys. Research Abstracts*, volume 5:11790. EGS, 2003. Cited at pag. 72
- [89] N. Thomas, S.F. Hviid, H.U. Keller, W.J. Markiewicz, T. Blümchen, A.T. Basilevsky, P.H. Smith, R. Tanner, C. Oquest, R. Reynolds, J.-L. Josset, S. Beauvivre, B. Hofmann, C.T. Rüffer, P. and Pillinger, M.R. Sims, D. Pullan, and S. Whitehead. The microscope for Beagle 2. *Planet Space Sci.*, 2003. Cited at pag. 93

-
- [90] P. J. Treado, I. W. Levin, and E. N. Lewis. High-fidelity Raman imaging spectrometry: a rapid method using an acoustooptic tunable filter. *Applied Spectroscopy*, 46:1211, 1992. Cited at pag. 105
- [91] N. K. Uzunoglu, N. G. Alexopoulos, and J. G. Fikioris. Scattering from thin and finite dielectric fibers. *J. Opt. Soc. Am.*, 68:194–197, 1978. Cited at pag. 21
- [92] Hoffmann V., Hochleitner R., Simon G., Fehr Th., Popp J., Tarcea N., and Funaki M. SNC-Meteorites: Magnetic Signature and Raman Spectroscopy. Abstract, IUGG/IAGA, Sapporo., 2003. Cited at pag. 69
- [93] J.R. Wait. Scattering of plane wave from a circular dielectric cylinder at oblique incidence. *J. Can. Phys.*, 33:189–195, 1955. Cited at pag. 2, 21
- [94] J.R. Wait. Electromagnetic scattering from a radially inhomogeneous sphere. *Appl. Sci. Res. B*, 10:441–450, 1963. Cited at pag. 2, 18, 20, 25
- [95] A. Wang and L. A. Haskin. Development of a flight Raman spectrometer for the Athena rover scientific instrument payload for Mars surveyor missions. *Institute of Physics Conference Series 2000*, 165(Microbeam Analysis 2000):103–104, 2000. Cited at pag. 79, 110, 129
- [96] A. Wang, L. A. Haskin, K. Kuebler, B. Jolliff, and M. Walsh. Raman spectroscopic detection of graphitic carbon of biogenic parentage in an ancient South African chert. LPS XXXII 2001 - abstract 1423, 2001. Cited at pag. 73
- [97] A. Wang, L. A. Haskin, A. L. Lane, T. J. Wdowiak, S. W. Squyres, R. J. Wilson, L. E. Hovland, K. S. Manatt, N. Raouf, and C. D. Smith. Development of the Mars microbeam Raman spectrometer (MMRS). *J. Geophys. Research, [Planets]*, 108(E1)(5):1–18, 2003. Cited at pag. 110
- [98] A. Wang, B. L. Jolliff, and L. A. Haskin. Raman spectroscopic characterization of a Martian SNC meteorite: Zagami. *Journal of Geophysical Research, [Planets]*, 104(E4):8509–8519, 1999. Cited at pag. 66
- [99] A. Wang, B. L. Jolliff, L. A. Haskin, K. E. Kuebler, and K. M. Viskupic. Characterization and comparison of structural and compositional features of planetary quadrilateral pyroxenes by Raman spectroscopy. *American Mineralogist*, 86(7-8):790–806, 2001. Cited at pag. 65
- [100] W. Weigand, M. Doerr, C. Robl, G. Kreisel, R. Grunert, J. Kaessbohrer, W. Brand, R. Werner, J. Popp, and N. Tarcea. Formation of ammonia from dinitrogen under primordial conditions. In *Proceedings of the Second*
-

- European Workshop on Exo/Astrobiology, Graz*, volume SP-518, pages 209–212. ESA, 2002. Cited at pag. 77
- [101] W. Weigand, G. Kreisel, C. Apfel, W. Brand, M. Dörr, H. Geilmann, R. Grunert, J. KäSSbohrer, and C. Robl. *Angew. Chem.*, 115:1579, 2003. Cited at pag. 77
- [102] B. C. Westcott. Electromagnetic wave propagation in spherically stratified isotropic media. *Electron. Lett.*, 4:572–573, 1968. Cited at pag. 2, 20
- [103] T. Wriedt. A Review of Elastic Light Scattering Theories. *Part. Part. Syst. Charact.*, 15:67–74, 1998. Cited at pag. 2, 20
- [104] Ph. J. Wyatt. Scattering of electromagnetic plane waves from inhomogeneous spherically symmetric objects. *Phys. Rev.*, 127:1837–1843, 1962. Cited at pag. 2, 20, 25
- [105] Ph. J. Wyatt. *Electromagnetic scattering*, chapter Light scattering from objects with spherical symmetry, pages 25–35. New York: Pergamon Press, 1963. Cited at pag. 2, 20, 25
- [106] Ph. J. Wyatt. Multiangle light scattering: The basic tool for macromolecular characterisation. *Instrumentation Science and Technology*, 25:1–18, 1997. Cited at pag. 11
- [107] D. D. Wynn-Williams and H. G. M. Edwards. Proximal analysis of regolith habitats and protective biomolecules in situ by laser Raman spectroscopy: Overview of terrestrial Antarctic habitats and Mars analogs. *Icarus*, 144(2):486–503, 2000. Cited at pag. 66
- [108] D. D. Wynn-Williams, H. G. M. Edwards, E. M. Newton, and J. M. Holder. Pigmentation as a survival strategy for ancient and modern photosynthetic microbes under high ultraviolet stress on planetary surfaces. *International Journal of Astrobiology*, 1(1):39–49, 2002. Cited at pag. 66
- [109] C. Yeh. Perturbation approach to the diffraction of electromagnetic waves by arbitrarily shaped dielectric obstacles. *Phys. Rev.*, 135:1193–1201, 1964. Cited at pag. 21
- [110] R. V. Yelle, J. C. McConnell, D. F. Strobel, and L. R. Doose. The far ultraviolet reflection spectrum of Uranus: results from the Voyager encounter. *Icarus*, 77(2):439–456, 1989. Cited at pag. 110

List of Figures

1.1	Core-shell microparticle	8
3.1	Elastic light scattering on a particle - general formulation	20
3.2	Core-shell microparticle: notations	25
3.3	The phase functions for homogeneous microparticles of 1, 3 and 6 μm radius	30
4.1	Basic experimental setup of the microcapsule analyzer device	35
4.2	Fitting error vs laser wavelength	36
4.3	Phase functions for the same particle for two different laser linewidths	37
4.4	Phase functions for the same particle using different laser wavelengths	38
4.5	Particular sizes which require 'composed' phase functions	39
4.6	Flowing cell with a planar window	42
4.7	Reflectance vs angle of incidence for a plane window	43
4.8	Flow cell with optics placed inside the flow chamber	44
4.9	The same phase function obtained for different theoretical sampling procedures (plane and circular detector arrays)	46
4.10	The scheme of the measurement cycle	47
4.11	Acquisition software user interface	48
4.12	Data evaluation software user interface	50
4.13	Measurement results on homogeneous standard particles.	53

4.14	Experimental scattering patterns and the closest match found in the database	54
4.15	Experimental scattering patterns and the closest match found in the database for microcapsules	56
4.16	Measurements on microcapsules	57
6.1	Raman spectra of different minerals	67
6.2	Raman spectra recorded from a Zagami slab.	70
6.3	Raman spectrum recorded from a pyroxene grain on SaU 060 Mars meteorite.	71
6.4	Surface scans on DAG735 Mars Meteorite.	72
6.5	Carbon containing material in SaU60 meteorite - Raman spectrum	73
6.6	Surface scans on NWA1086 Mars Meteorite.	74
6.7	A line scan on NWA 856 meteorite.	75
6.8	Raman spectra of anatase and pyroxene in SaU 060	76
6.9	Overlapped Raman spectra of pyrite and magnetite from NWA 1068 olivin-phyric shergottite	77
7.1	MIRAS -Unfolded setup AOTF based	85
7.2	AOTF - functioning principle	88
7.3	AOTF - calibration curve	89
7.4	APD Quantum Efficiency.	90
7.5	MIRAS -Folded setup AOTF based	91
7.6	Data structure and achievable compression.	93
7.7	Extended-MIRAS: Raman-Microscope combined instrument configuration	94
8.1	Detector quantum efficiency and the first linear approximation used for correction	97
8.2	Typical correction factor due to pile-up effects	98
8.3	Afterpulsing probability for an APD photon counting device	99
8.4	User interface for the alignment function	100
8.5	Employed relational database structure for Raman spectra of minerals	101
9.1	MIRAS BB - Raman spectra of olivine at different spectral steps	104
9.2	MIRAS BB - Raman spectra of olivine recorded with different integration times	105
9.3	Raman spectrum of Silicon measured with the BB version of MIRAS	106
9.4	Raman spectrum of a polycarbonate matrix measured with the BB version of MIRAS	106
9.5	Image taken through the AOTF of a mixture of polyvinyl particles in TiO ₂	107

10.1	Output from the RRS simulator(different harmonics of a Nd:YAG laser)	120
B.1	Flow trough cell with the laser path.	139
B.2	Complete setup with the schematic ray path depicted	140
B.3	Complete setup with the flow cell having he collecting optics inside	140
C.1	Acousto-Optic Tunable Filter	141
C.2	The External-Cavity-Diode Laser in Littrow configuration	142
C.3	The APD based SPCM-AQR-15 photon counter module	142
C.4	MIRAS Breadboard assembled at Kayser Threde GmbH - Munich	143
C.5	User interface view for the MIRAS software control	144
C.6	MIRAS - supporting database: user interface - mineral classification	144
C.7	MIRAS - supporting database: user interface - raman spectra . . .	145
C.8	MIRAS - supporting database: user interface - edit raman information	145

List of Symbols and Abbreviations

<p>a_C microparticle core radius</p> <p>AD <i>abbr.</i> Anomalous Diffraction (approximation)</p> <p>a_n Mie scattering coefficient</p> <p>AO <i>abbr.</i> Adaptive Optics</p> <p>AOTF <i>abbr.</i> Acusto-optic Tunable Filter</p> <p>APD <i>abbr.</i> Avalanche Photo Diode</p> <p>APXS <i>abbr.</i> alpha proton X-ray spectroscopy</p> <p>a_S microparticle shell radius</p> <p>BB <i>abbr.</i> Breadboard</p> <p>b_n Mie scattering coefficient</p> <p>BSS <i>abbr.</i> Back-scattering Spec- troscopy</p> <p>CCD <i>abbr.</i> Charge Coupled Device</p> <p>CDM <i>abbr.</i> Coupled Dipoles Method</p> <p>CHDF <i>abbr.</i> Capillary Hydrody- namic Fractionation</p> <p>CW <i>abbr.</i> continuous wave (laser)</p>	<p>DAG <i>abbr.</i> Dar al Gani (strewn field)</p> <p>DIAL <i>abbr.</i> differential absorption LIDAR</p> <p>DLR <i>abbr.</i> Deutschen Zentrum für Luft- und Raumfahrt</p> <p>E electric field intensity</p> <p>EBCM <i>abbr.</i> Extended Boundary Condition Method</p> <p>ECDL <i>abbr.</i> External Cavity Diode Lasers</p> <p>EPP <i>abbr.</i> Enhanced Parallel Port</p> <p>ESA <i>abbr.</i> European Space Agency</p> <p>FTIR <i>abbr.</i> Fourier Transform In- frared Spectroscopy</p> <p>GO <i>abbr.</i> Geometrical Optics (approximation)</p> <p>H magnetic field intensity</p>
---	---

LIDAR	<i>abbr.</i> Light Detection and Ranging	x	size parameter
LALLS	<i>abbr.</i> Low Angle Laser Light Scattering	$\epsilon, \epsilon_0, \epsilon_r$	dielectric constant, vacuum, relative
m	relative refractive index	λ	wavelength
MDR	<i>abbr.</i> Morphology Dependent Resonances	μ, μ_0, μ_r	magnetic permeability, vacuum, relative
MIRAS	<i>-abbr.</i> Mineral Investigation by <i>in situ</i> Raman Spectroscopy	ρ	radial distance kr (dimensionless)
MSM	<i>-abbr.</i> Mineralogische Staatssammlung München	σ	specific conductance
		Θ, θ	scattering angle
n	real part of refractive index		
N.A.	<i>abbr.</i> Numerical Aperture		
NWA	<i>abbr.</i> Northwest Africa (strewn field)		
O.D.	<i>abbr.</i> optical density		
PAP	<i>abbr.</i> Power Aperture Product		
PCS	<i>abbr.</i> Photon Correlation Spectroscopy		
PMT	<i>abbr.</i> Photomultiplier Tube		
RDG	<i>abbr.</i> Rayleigh Debye Gans (approximation)		
RPM	<i>abbr.</i> Rotations per minute		
RRS	<i>abbr.</i> Remote Raman Spectroscopy		
SaU	<i>abbr.</i> Sayh al Uhaymir (strewn field)		
SEE	<i>abbr.</i> Single Event Effect		
SEU	<i>abbr.</i> Single Event Upset		
SF3	<i>abbr.</i> Sedimentation Field Flow Fractionation		
SNC	<i>abbr.</i> Shergotty - Nahkla - Chassigny		
tbd	<i>abbr.</i> to be determined		

Danksagung

Die vorliegende Dissertation hätte nicht ohne die Unterstützung vieler entstehen können, denen ich vielmals danken möchte.

An erster Stelle gilt mein Dank Prof. Dr. Dr. h.c. Wolfgang Kiefer, der mir die Möglichkeit gab, an seinem Lehrstuhl das Promotionsstudium zu absolvieren. Ich danke ihm sowohl für seine Unterstützung bei allen auftretenden Fragestellungen als auch für die finanzielle Förderung.

Prof. Dr. Jürgen Popp möchte ich meinen Dank aussprechen, dass er mich in seine Arbeitsgruppe aufnahm und mir die Beteiligung an wichtigen wissenschaftlichen Projekten ermöglichte. Ebenso wertvoll waren mir die fachlichen Diskussionen, welche zur Entwicklung neuer Ideen beigetragen haben.

Prof. Dr. Volker Engel danke ich für die Übernahme des Korreferats.

Weiterhin bedanke ich mich bei den Kooperationspartnern Dr. Stefan Hofer, Dr. Elke Schmidt und Dr. Volker Klein von der Firma Kayser-Threde in München sowie Dr. Gilla Simon von der Mineralogischen Staatssammlung München für die stets gute Zusammenarbeit.

Ganz herzlichen Dank an alle in der Gruppe. Dr. Michael Schmitt danke ich

für die stetige Diskussionsbereitschaft. Nicht unerwähnt bleiben sollen meine ehemaligen Kollegen Dr. Oliver Sbanski, mit dem ich anfangs am Schering-Projekt zusammengearbeitet habe, Dr. Torsten Siebert, Dr. Monica Bolboaca, Dr. Lucian Baia, Dr. Nicolae Leopold, Dr. Ralph Geßner, Dr. Petra Rösch, Dr. Marion Strehle und Dr. Renate Petry, die jederzeit zu einem entspannten und freundlichen Arbeitsklima beizutragen wussten. Für die gute Arbeitsatmosphäre danke ich ebenso Adriana Szeghalmi, Joachim Koster, Raman Maksimenka, Krisztina Babocsi und Benjamin Dietzek. Besonders dankbar bin ich meinen Freunden Cristina Dem und Dr. Claudiu Dem, die mir mit Rat und Tat zur Seite standen.

Belinda Leimeister und Melanie Grom möchte ich meinen Dank für ihre freundliche Haltung ausdrücken. Ebenso herzlichen Dank Herrn Peter Popp für die Hilfe bei Computer- und Netzwerkproblemem. Ein aufrichtiges Dankeschön möchte ich der ganzen Mechanik- und Elektronikwerkstatt aussprechen, vor allem Rainer Eck, Jürgen Zimmermann, Wolfgang Liebler, Ralph Kohrman und Thomas Schreckling für die schnelle und einwandfreie Erledigung der Aufträge. Gleichzeitig danke ich Frau Müller für die Hilfsbereitschaft, die anfallenden Verwaltungsformalitäten immer freundlich zu übernehmen.

Für das Korrekturlesen dieser Arbeit bedanke ich mich bei Prof. Dr. Jürgen Popp, Dr. Claudiu Dem, Joachim Koster, Dr. Torsten Siebert und meiner Beatrice, der ich für ihre Geduld und Zuneigung sehr dankbar bin.

Von Herzen danke ich meinen Eltern, die mich aus der Ferne stets unterstützt und motiviert haben.

Lebenslauf

PERSÖNLICHE ANGABEN

Name: Nicolae Tarcea
Geburtsdatum: 13.Juli 1976
Geburtsort: Orlat/Rumänien
Staatsangehörigkeit: rumänisch
Familienstand: ledig

AUSBILDUNG

Promotion

seit 09/2000

Promotionsstudium am Institut für Physikalische Chemie II der Universität Würzburg bei Prof. Dr. Dr. h.c. W. Kiefer

Studium

10/1999-7/2000

Physikstudium (Master of Science), Studiengang Physik der oxydischen Materialien, an der Fakultät für Physik der Universität Babes-Bolyai, Cluj-Napoca(Klausenburg), Rumänien

Titel der Arbeit: "Vibrational Studies on $xB_2O_3(1-x)CaO$ and $xCuO(1-x)[2B_2O_3CaO]$ Glass Systems"

Abschluß: Magisterdiplom - Master of Science

10/1994-7/1999

Physikstudium, Studiengang Technologische Physik, an der Fakultät für Physik der Universität Babes-Bolyai, Cluj-Napoca, Rumänien

Titel der Diplomarbeit: "Ellipsometric Measurements on Thin Films of Octaclorfenotiazinil and SiO_2/Si "

Abschluß: Diplom, Ingenieurtitel

Schulbildung

9/1990-7/1994

Kollegium "Gheorghe Lazar" in Sibiu (Hermannstadt), Rumänien

BERUFSTÄTIGKEIT

seit 2001

Wissenschaftlicher Mitarbeiter am Institut für Physikalische Chemie II der Universität Würzburg

9/2000-12/2001

Wissenschaftliche Hilfskraft am Institut für Physikalische Chemie II der Universität Würzburg

9/1999-1/2000

Wissenschaftliche Hilfskraft am Lehrstuhl für Optik der Fakultät für Physik der Universität Babes-Bolyai, Cluj-Napoca